

**MEASUREMENT OF MULTIJET CROSS-SECTION RATIOS  
IN PROTON-PROTON COLLISIONS WITH THE  
CMS DETECTOR AT THE LHC**

A THESIS

Submitted to the  
FACULTY OF SCIENCE  
PANJAB UNIVERSITY, CHANDIGARH  
for the degree of

**DOCTOR OF PHILOSOPHY**

**2018**

**Anterpreet Kaur**

DEPARTMENT OF PHYSICS  
CENTRE OF ADVANCED STUDY IN PHYSICS  
PANJAB UNIVERSITY, CHANDIGARH  
INDIA



*Dedicated to  
my Parents*



## **Acknowledgement**

*I would like to take this opportunity to thank the many people who helped make this dissertation possible.*

*In the first and foremost place, I gratefully express my sincere gratitude to my supervisor Prof.(Mrs.) Manjit Kaur for her invaluable assistance, support, guidance and blessings. She inspired me greatly to work in this project. Her willingness to motivate me contributed tremendously to this project.*

*I am highly obliged to Prof. C.S. Aulakh Chairperson of the Department of Physics, Panjab University, Chandigarh, for his helping hand in providing a good environment and adequate facilities to complete this project successfully.*

*I feel deeply indebted to my parents for their unconditional love, understanding, support, strength, blessings and for everything.*

*I am greatly thankful to my wellwishers, my friends Anu, Sohail, Junaid, Mandeep and my classmates for all that they meant to me during the crucial times of the completion of my project.*

*I owe my very special thanks to Mr. Inderpal Singh, Mrs. Prabhdeep Kaur, Mrs. Manuk Z. Mehta, Ms. Ritu Aggarwal, Ms. Ruchi Gupta, Ms. Monika Mittal and Ms. Genius, the members of high energy physics Laboratory, Dept. of Physics, P.U. for helping me out from all kinds of problems with their constant support, suggestions and encouragement.*

*Finally and the most importantly, I would like to pay my greatest regards to the Almighty God for His blessings and kindness, a boundless and an endless source of inspiration for me always.*



# Abstract

The collisions of hadrons at very high centre-of-mass energies provide a direct probe to the nature of the underlying parton-parton scattering physics. The scattering of the elementary quark and gluon constituents of the incoming hadron beams produces a high momentum partons which then fragment to spray of particles clustered in the form of jets. These jets are the final structures observed in the detector and they preserve the energy and direction of the initial partons. Hence jets can serve as a direct test of theory of strong interactions called Quantum Chromodynamics. The inclusive multijet production cross-section is an important observable which provides the details of parton distribution functions (PDF) of the colliding hadrons and the precise measurement of the strong coupling constant  $\alpha_s$ . Instead of individual cross-sections, the cross-section ratio is a better tool to determine the value of  $\alpha_s$  as many theoretical and experimental uncertainties cancel in the ratio.

A measurement of inclusive multijet event cross-sections and the cross-section ratio is presented using data from proton-proton collisions collected with the CMS detector at a centre-of-mass energy of 8 TeV corresponding to an integrated luminosity of  $19.7 \text{ fb}^{-1}$ . Jets are reconstructed with the anti- $k_t$  clustering algorithm for a jet size parameter  $R = 0.7$ . The inclusive 2-jet and 3-jet event cross-sections as well as the ratio of the 3-jet over 2-jet event cross-section  $R_{32}$  are measured as a function of the average transverse momenta  $p_T$  of the two leading jets in a phase space region ranging up to jet  $p_T$  of 2.0 TeV and an absolute rapidity of  $|y| = 2.5$ . The measurements after correcting for detector effects are well described by predictions at next-to-leading order in perturbative quantum chromodynamics and additionally are compared to several Monte Carlo event generators. The strong coupling constant at the scale of the  $Z$  boson mass is extracted from a fit of the measured  $R_{32}$  which gives  $\alpha_s(M_Z) = 0.1150 \pm 0.0010 \text{ (exp)} \pm 0.0013 \text{ (PDF)} \pm 0.0015 \text{ (NP)} {}^{+0.0050}_{-0.0000} \text{ (scale)}$  using MSTW2008 PDF set. The current measurement agrees well with the world average value of  $\alpha_s(M_Z) = 0.1181 \pm 0.0011$  as well as previous measurements.



# Contents

<b>1</b>	<b>Introduction</b>	<b>1</b>
<b>2</b>	<b>Theoretical Background</b>	<b>5</b>
2.1	Standard Model . . . . .	5
2.2	Quantum Chromodynamics . . . . .	8
2.2.1	Perturbative Quantum Chromodynamics . . . . .	12
2.2.2	Renormalization and Running of the Strong Coupling . . . . .	13
2.2.3	Factorization and Parton Distribution Functions . . . . .	17
2.3	Hadron Collisions . . . . .	17
2.3.1	Parton Shower . . . . .	17
2.3.2	Hadronization . . . . .	17
2.3.3	Underlying Event and Multi-Parton Interactions . . . . .	17
2.4	Jets . . . . .	17
2.4.1	Jet Algorithms . . . . .	17
2.4.2	Jet Properties . . . . .	17
2.5	Leading order and next-to-leading order calculations . . . . .	19
2.6	Parton Distribution Functions . . . . .	20
<b>3</b>	<b>Experimental Setup</b>	<b>21</b>
3.1	The Large Hadron Collider . . . . .	22

---

3.2 Luminosity Measurement . . . . .	24
3.3 The Compact Muon Solenoid . . . . .	26
3.3.1 Coordinate System . . . . .	28
3.3.2 Inner Tracker System . . . . .	31
3.3.3 Electromagnetic Calorimeter . . . . .	33
3.3.4 Hadronic Calorimeter . . . . .	34
3.3.5 Superconducting Magnet . . . . .	37
3.3.6 Muon System . . . . .	38
3.3.7 Trigger and Data Acquisition System . . . . .	40
3.3.7.1 Jet Triggers . . . . .	42
3.3.7.2 Data Acquisition System . . . . .	42
3.3.8 Data Management . . . . .	43
<b>4 Event Generation, Simulation and Reconstruction</b> . . . . .	<b>45</b>
4.1 Event Generation and Simulation Software . . . . .	45
4.1.1 PYTHIA . . . . .	47
4.1.2 MADGRAPH5 . . . . .	47
4.1.3 HERWIG . . . . .	48
4.1.4 POWHEG . . . . .	48
4.1.5 NLOJET++ and FASTNLO . . . . .	48
4.2 Detector Simulation . . . . .	49
4.3 Event Reconstruction . . . . .	51
4.3.1 Particle Flow Algorithm . . . . .	53
4.3.2 Jet Energy Corrections . . . . .	54
4.4 Software Tools . . . . .	57
4.4.1 CMSSW Framework . . . . .	57

4.4.2	ROOT . . . . .	58
<b>5</b>	<b>Measurement of the Differential Inclusive Multijet Cross-sections and their Ratio</b>	<b>59</b>
5.1	Data Samples . . . . .	60
5.1.1	Monte Carlo Samples . . . . .	61
5.2	Event Selection . . . . .	62
5.2.1	Trigger Selection . . . . .	62
5.2.2	Primary Vertex Selection . . . . .	64
5.2.3	Missing Transverse Energy . . . . .	66
5.2.4	Jet Identification . . . . .	66
5.2.4.1	Jet ID Efficiency . . . . .	67
5.2.5	Jet Selection . . . . .	71
5.3	Comparison with Simulation . . . . .	71
5.3.1	Pileup Reweighting . . . . .	71
5.3.2	Comparison of Cross-sections and their Ratio . . . . .	72
5.4	Jet Energy Resolution (JER) . . . . .	75
5.5	Unfolding . . . . .	80
5.5.1	Response Matrices . . . . .	82
5.5.1.1	Inclusive Cross-sections . . . . .	82
5.5.1.2	Cross-section Ratio, $R_{32}$ . . . . .	85
5.5.2	Closure Test . . . . .	86
5.5.3	Unfolding of the Measurement . . . . .	87
5.6	Experimental Uncertainties . . . . .	89
5.6.1	Statistical Uncertainty . . . . .	90
5.6.2	Jet Energy Corrections Uncertainty . . . . .	91

5.6.3	Unfolding Uncertainty . . . . .	94
5.6.4	Luminosity Measurement Uncertainty . . . . .	95
5.6.5	Residual Uncertainty . . . . .	96
5.6.6	Total Experimental Uncertainty . . . . .	96
<b>6</b>	<b>Theoretical Calculations</b>	<b>99</b>
6.1	Fixed Order NLO Calculations . . . . .	99
6.1.1	NLO Correction Factors . . . . .	101
6.1.2	Non-Perturbative Corrections . . . . .	102
6.1.3	Electroweak Corrections . . . . .	104
6.2	Theoretical Uncertainties . . . . .	106
6.2.1	Scale Uncertainty . . . . .	106
6.2.2	PDF Uncertainty . . . . .	107
6.2.3	Non-perturbative Uncertainty . . . . .	108
6.2.4	Total Theoretical Uncertainty . . . . .	108
6.3	Comparison of Theory to Data . . . . .	110
<b>7</b>	<b>Determination of the Strong Coupling Constant</b>	<b>115</b>
7.1	Sensitivity of Measurements to $\alpha_s(M_Z)$ . . . . .	116
7.2	Determination of $\alpha_s(M_Z)$ . . . . .	117
7.2.1	Fitting Procedure . . . . .	117
7.2.2	Fit Results . . . . .	123
7.3	Running of the Strong Coupling Constant . . . . .	126
<b>8</b>	<b>Summary</b>	<b>130</b>
<b>Appendix A</b>		<b>134</b>

A.1	Cross-section Ratio, $R_{32}$	135
A.2	Individual Sources of Jet Energy Correction Uncertainties	136
A.3	Experimental Uncertainties	139
A.4	Theoretical Uncertainties	142
	<b>Bibliography</b>	<b>145</b>



# Chapter 1

## Introduction

Particle physics deals with the study of the basic constituents of matter and the forces governing the interactions among them. The Standard Model (SM) is the most accepted theory which describes the nature and properties of the fundamental particles and their interactions. The elementary particles leptons and quarks, known as fermions, interact through the exchange of gauge bosons and acquire mass through a scalar boson called the Higgs. The four fundamental forces of interaction existing in nature are : the electromagnetic force, the strong force, the weak force and the gravitational force. Quantum Chromodynamics (QCD) is the theory of the strong interactions between the quarks mediated by the massless gluons. The partons (quarks and gluons) have a peculiar property of “color” charge. The quarks strongly binds into colorless particles called hadrons such as protons and neutrons together known as nucleons, pions etc. The structure and the properties of sub-atomic particles can be explored by first accelerating them using particle accelerators and then colliding at very high energies. The end products of these collisions get detected in the particle detectors constituting the real data. The data sets analyzed in details to reveal the structure and characteristic properties of the fundamental particles.

To investigate the very rare particles or to search for physics beyond SM, the

particle accelerators have become ever bigger and more complex. The Large Hadron Collider (LHC) is one of the today's biggest and most powerful collider where the protons are accelerated and collided at extremely high center-of-mass energies to probe their internal structure described by parton distribution functions (PDFs). The PDF sets give the probability for finding a parton at an energy scale  $Q$  with a fractional momentum  $x$  of the proton. Since the proton is not elementary and is made up of partons, the proton-proton (pp) collisions are viewed as interactions between their constituent partons. The final products of the scattering are observed by Compact Muon Solenoid (CMS), one of the detectors located around the interaction points. The scattering cross-section can be defined as a sum of terms with increasing powers of the strong coupling constant  $\alpha_S$  convoluted with PDFs. The lowest-order  $\alpha_S^2$  term represents the production of two partons in final states whereas terms of higher-order  $\alpha_S^3$ ,  $\alpha_S^4$  etc. signify the existence of multi partons in final states. The final state partons give a parton shower (PS) due to decrease in energy through emission of other quarks and gluons. The colored products of parton shower hadronize to a spray of colorless hadrons known as jets. The jets are the final structures observed in the detector. So they carry the significant information about the energy and direction of the initial partons and hence are important to study. The final partons have the probability to radiate more gluons resulting in multijets in the final state. Such events are produced in large number and are an important source for testing the predictions given by QCD. They also serve as an important background in the searches for new particles and physics beyond SM.

The inclusive multijet event cross-section  $\sigma_{i-jet}$  given by  $pp \rightarrow i \text{ jets} + X$ , where every jet counts, is proportional to  $\alpha_s^i$ . The inclusive jet cross-section studied in terms of jet  $p_T$  and rapidity  $y$  is one of the important observables as it provides the essential information about the PDFs and the precise measurement of  $\alpha_S$ . Also the ratio of cross-sections given by Eq. 1.1 is proportional to the QCD coupling  $\alpha_S$

and hence can be used to determine the value of  $\alpha_S$ .

$$R_{mn} = \frac{\sigma_{m-jet}}{\sigma_{n-jet}} \propto \alpha_S^{m-n} \quad (1.1)$$

Instead of studying inclusive cross-sections, the cross-section ratio is more useful because of the partial or complete cancellation of many theoretical and experimental uncertainties between numerator and denominator. The CMS Collaboration has previously measured the ratio of the inclusive 3-jet cross-section to the inclusive 2-jet cross-section as a function of the average transverse momentum,  $\langle p_{T1,2} \rangle$ , of the two leading jets in the event at 7 TeV [1] and lead to an extraction of  $\alpha_s(M_Z) = 0.1148 \pm 0.0055$ , where the dominant uncertainty stems from the estimation of higher-order corrections to the NLO prediction. In this analysis, a measurement of inclusive 2-jet and 3-jet event cross-sections as well as ratio of 3-jet event cross-section over 2-jet  $R_{32}$ , is presented using an event sample collected by the CMS experiment during 2012 at the LHC and corresponding to an integrated luminosity of  $19.7 \text{ fb}^{-1}$  of pp collisions at a centre-of-mass energy of 8 TeV. The event scale is chosen as before to be the average transverse momentum of the two leading jets, but will be referred to as  $H_{T,2}/2$  in this thesis. The measurements are used to determine the value of the strong coupling constant at the scale of the  $Z$  boson mass  $\alpha_s(M_Z)$  and the running of  $\alpha_S$  with energy scale  $Q$  is studied.

This thesis is organized as :

**Chapter 2** gives a brief overview of the Standard Model of particle physics and the theory of strong interactions QCD with main emphasis on the jets and jet algorithms.

**Chapter 3** deals with experimental apparatus which covers the details of the CMS detector and its various sub-detectors.

**Chapter 4** describes the methods of event generation using different Monte-Carlo event generators, detector geometry simulation and reconstruction of the par-

---

ticles in the detector. This chapter also gives an overview of the different approaches of jet reconstruction at CMS and application of jet-energy corrections along with the description of the software framework used in the analysis presented in the current thesis.

**Chapter 5** presents the measurement of inclusive differential multijet cross-sections and the cross-section ratio. The measurements are corrected for detector effects by unfolding procedure which is discussed in details in this chapter. The sources of the experimental uncertainties are studied in details.

**Chapter 6** contains a detailed description of the NLO pQCD theory predictions compared to data and the extraction of  $\alpha_s$ . The NLO calculations are corrected with the non-perturbative and electroweak corrections. The theoretical uncertainties are calculated from various sources. The unfolded measurements are compared to the predictions at NLO in pQCD and additionally as well as to predictions from several Monte Carlo event generators.

**Chapter 7** describes the method to extract  $\alpha_s(M_Z)$  from the current measurement and the running of  $\alpha_s$  with energy scale  $Q$  is presented along with the previous measurements from different experiments.

**Chapter 8** summarizes the results and conclusions of the work done in this thesis.

The common unit convention based on International System of Units (SI), followed in particle physics, will be used throughout the thesis. It is supplemented with the units electron volt (eV) for energy and barn (b) for the interaction cross section. The speed of light ( $c$ ) and the reduced Planck constant ( $\hbar$ ) are set to unity, i.e.  $\hbar = c = 1$ .

# Chapter 2

## Theoretical Background

Since 1930s, many theories and discoveries in particle physics have revealed the fundamental structure of matter. The matter is made up of fundamental particles and their interactions are mediated by four fundamental forces [2]. The theoretical models describe all the phenomena of particle physics as well as predict the nature and properties of particles. These models must be either confirmed experimentally or totally excluded giving hints of new physics. This interplay between experimental discoveries and the corresponding theoretical predictions leads to describe the fundamental particles and their interactions through a theoretical model, known as the Standard Model. The world's most powerful particle accelerators and detectors are used by physicists to test the predictions and limits of the Standard Model where it has successfully explained almost all experimental results. This chapter describes the Standard Model with the main focus on Quantum Chromodynamics and its properties which serve as the theoretical foundations of this thesis.

### 2.1 Standard Model

The Standard Model (SM) of particle physics [3–5] was developed in 1970s. It is a mathematical framework which describes the properties of fundamental particles and

the forces of interactions between them, as summarized in Fig. 2.1. According to the SM, there are 12 elementary particles i.e. without any internal structure, known as fermions. The fermions having half integral spin obeying Fermi-Dirac statistics and follows the Pauli exclusion principle. Each fermion has a corresponding antiparticle with same properties but opposite-sign quantum numbers. Depending on how the

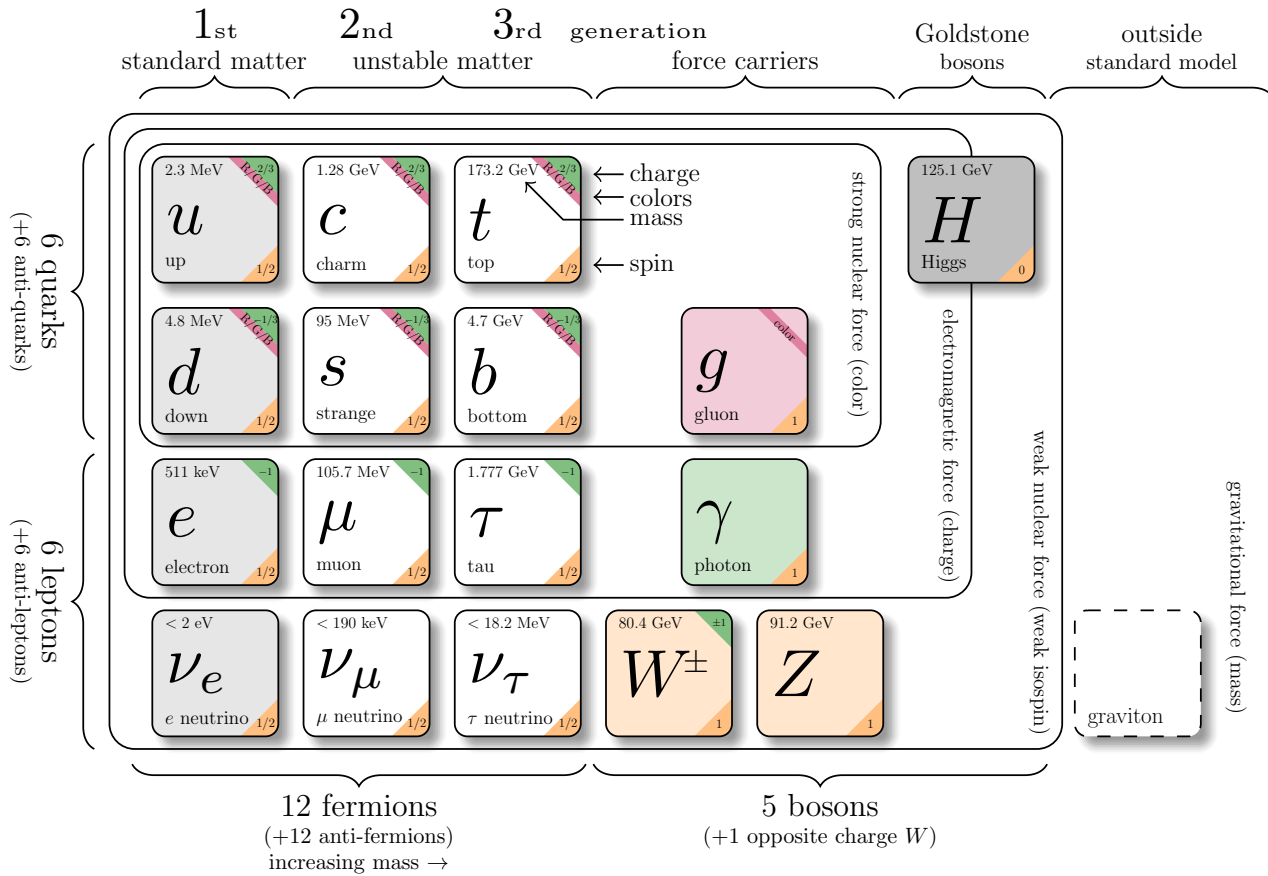


Figure 2.1: The Standard Model<sup>1</sup> summarizing the properties of elementary particles known as fermions (leptons and quarks), grouped into three generations, gauge bosons as mediators for the interactions, the scalar Higgs boson and not incorporated graviton for the gravitational force.

fermions interact, they are classified into two categories - leptons ( $\ell$ ) and quarks ( $q$ ). There are six types of leptons : electron ( $e$ ), muon ( $\mu$ ) and tau ( $\tau$ ) with

<sup>1</sup>Source : <http://www.texample.net/tikz/examples/model-physics>

electric charge  $Q = -1$  (all charges are in the units of elementary charge  $e$ ) and the corresponding neutrinos  $\nu_e$ ,  $\nu_\mu$  and  $\nu_\tau$  having electric charge  $Q = 0$ . There are six “flavors” of quarks : up ( $u$ ), down ( $d$ ), strange ( $s$ ), charm ( $c$ ), bottom ( $b$ ) and top ( $t$ ).  $u$ ,  $c$  and  $t$  carry charge  $Q = \pm \frac{2}{3}$  whereas  $d$ ,  $s$  and  $b$  carry charge  $Q = \pm \frac{1}{3}$ . The quarks and leptons are categorized into three generations. The lightest and the most stable particles belong to first generation and the second and third generations have the heavier and less stable particles.

There are four fundamental forces existing in nature : electromagnetic, strong, weak and gravitational force. Every interaction involves the exchange of a gauge boson : the photon ( $\gamma$ ) for the electromagnetic force, gluons ( $g$ ) for the strong force, two  $W$ ’s and a  $Z$  for the weak force and the graviton (not yet found) for the gravitational force. However, the gravitational force has not been incorporated into SM yet. Along with this, the existence of dark matter or energy and the matter-antimatter asymmetry are still missing pieces in the SM. Each force acts between particles because of some property of that particle - charge for electromagnetism, color for the strong force and flavor for the weak force.

In the SM, first three forces are unified into one quantum field theory [6], known as Grand Unified Theory (GUT) [7–9]. The SM framework is based on quantum field theories and is described by  $SU(3)_C \otimes SU(2)_L \otimes U(1)_Y$  gauge symmetry. Here,  $SU(2)_L \otimes U(1)_Y$  term describes the weak and electromagnetic forces, respectively. The electromagnetic interaction of particles is explained by a well established modern theory of Quantum Electrodynamics (QED). In SM, the weak and electromagnetic interactions are combined by electroweak theory. The electroweak symmetry is spontaneously broken by the coupling to the scalar Higgs field. The gauge bosons of the unified electroweak theory are a mixture of the gauge bosons of the unbroken symmetry resulting in the massive  $W^\pm$  and  $Z$  bosons, and the massless photon ( $\gamma$ ). The Higgs boson, named after Peter Higgs, is the field quantum of the Higgs field responsible for electroweak symmetry breaking. It was discovered by

the CMS [10] and ATLAS [11] collaborations in 2012, with the properties consistent with the SM. The  $SU(3)_C$  term defines the strong interaction between quarks and gluons mediated by gluons, with the three degrees of freedom of the color charge (C). In contrast to the electroweak symmetry, the  $SU(3)_C$  of the strong interaction is an exact symmetry and hence the gluons are massless. The strong interaction between quarks and gluons is described by theory called Quantum Chromodynamics (QCD), explained in details in the next section of this thesis.

## 2.2 Quantum Chromodynamics

Quantum Chromodynamics [12, 13] is the non-abelian gauge theory of strong interactions between the quarks and gluons. The gauge group of QCD is the special unitary group  $SU(3)_C$  with color charges C as the generators of the gauge group. Color charge is the peculiar property of QCD and has a same role as the electric charge in electromagnetic interactions. However, the mediator of electromagnetic interactions i.e. photon, itself does not carry any electric charge whereas the gluon carry color charge. This allows the self coupling of gluons and hence make the theory non-Abelian. Both the quarks and gluons carry three colors : red ( $r$ ), green ( $g$ ) and blue ( $b$ ), and three anti-colors : anti-red ( $\bar{r}$ ), anti-green ( $\bar{g}$ ) and anti-blue ( $\bar{b}$ ). The quarks carry a single color charge whereas gluons carry a combination of color charges. There are nine eigen states of gluons but one of them  $\frac{1}{\sqrt{3}}(r\bar{r} + g\bar{g} + b\bar{b})$  is totally symmetric color singlet which has no net color charge and does not take part in interaction. The remaining eight eigen states of the gluons are :

$$r\bar{b}, \ r\bar{g}, \ b\bar{g}, \ b\bar{r}, \ g\bar{r}, \ g\bar{b}, \ \frac{1}{\sqrt{2}}(r\bar{r} - b\bar{b}), \ \frac{1}{\sqrt{6}}(r\bar{r} + b\bar{b} - 2g\bar{g}) \quad (2.1)$$

The dynamics of the quarks and gluons are controlled by the gauge invariant

QCD Lagrangian  $\mathcal{L}_{QCD}$  which is composed of four terms as :

$$\mathcal{L}_{QCD} = \underbrace{-\frac{1}{4}F_{\mu\nu}^A F_A^{\mu\nu}}_{\mathcal{L}_{gluons}} + \underbrace{\sum_{flavors} \bar{q}_a (i\gamma^\mu (D_\mu)_{ab} - m_q) q_b}_{\mathcal{L}_{quarks}} + \mathcal{L}_{gauge} + \mathcal{L}_{ghost} \quad (2.2)$$

where  $\mathcal{L}_{gluons}$  represents the kinetic term of the gluon fields  $\mathcal{A}_\mu^A$ ,  $\mathcal{L}_{quarks}$  describes the interaction of spin- $\frac{1}{2}$  quark fields  $q_a$  of mass  $m_q$  with spin-1 gluon fields  $\mathcal{A}_\mu^A$  summing over all presently known six flavors u, d, s, c, b, and t;  $\mathcal{L}_{gauge}$  defines the chosen gauge and  $\mathcal{L}_{ghost}$  is the so-called ghost term which is a remedy necessary to treat the degeneracy of equivalent gauge field configurations in non-Abelian gauge theories. Here the Greek letters  $\mu, \nu, \dots \in \{0,1,2,3\}$  represents space-time indices whereas  $a,b,c \in \{1,2,3\}$  and  $A,B,C \in \{1,\dots,8\}$  are the indices of the triplet and octet representations, respectively, of the  $SU(3)_C$  gauge symmetry group.  $F_{\mu\nu}^A$  is the field tensor defined as

$$F_{\mu\nu}^A = \partial_\mu \mathcal{A}_\nu^A - \partial_\nu \mathcal{A}_\mu^A - g_s f_{ABC} \mathcal{A}_\mu^B \mathcal{A}_\nu^C \quad (2.3)$$

where  $g_s$  is the coupling constant determining the strength of the interaction between colored partons and  $f_{ABC}$  are the structure constants of the  $SU(3)_C$  group. The third term in Eq. 2.3 is a non-Abelian term which distinguishes QCD from QED and gives rise to a three-gluon and a four-gluon vertex.  $(D_\mu)_{ab}$  is the covariant derivative given by Eq. 2.4 and  $\gamma_\mu$  are the Dirac  $\gamma$ -matrices.

$$(D_\mu)_{ab} = \partial_\mu \delta_{ab} + i g_s T_{ab}^A \mathcal{A}_\mu^A \quad (2.4)$$

There are eight gluon fields  $\mathcal{A}_\mu^A$  with factors  $T_{ab}^A$  corresponding to the generators of the  $SU(3)_C$  gauge group. A representation of the generators is given via  $T^A = \lambda^A / 2$  by the Hermitian and traceless Gell-Mann matrices  $\lambda^A$  [14]. The generator matrices

$T^A$  satisfy the commutation relations

$$\left[ T^A, T^B \right] = i f_{ABC} T^C \quad (2.5)$$

In  $\mathcal{L}_{QCD}$ , the classical contribution comes from  $\mathcal{L}_{gluons}$  and  $\mathcal{L}_{quarks}$  terms which correspond to the free quark- and gluon-field terms, and the quark-gluon interaction term presented in Fig. 2.2. Along with this, the non-Abelian group structure of QCD leads to the cubic and quartic gluon self-interaction vertices, which are proportional to  $g_s$  and  $g_s^2$ , respectively.

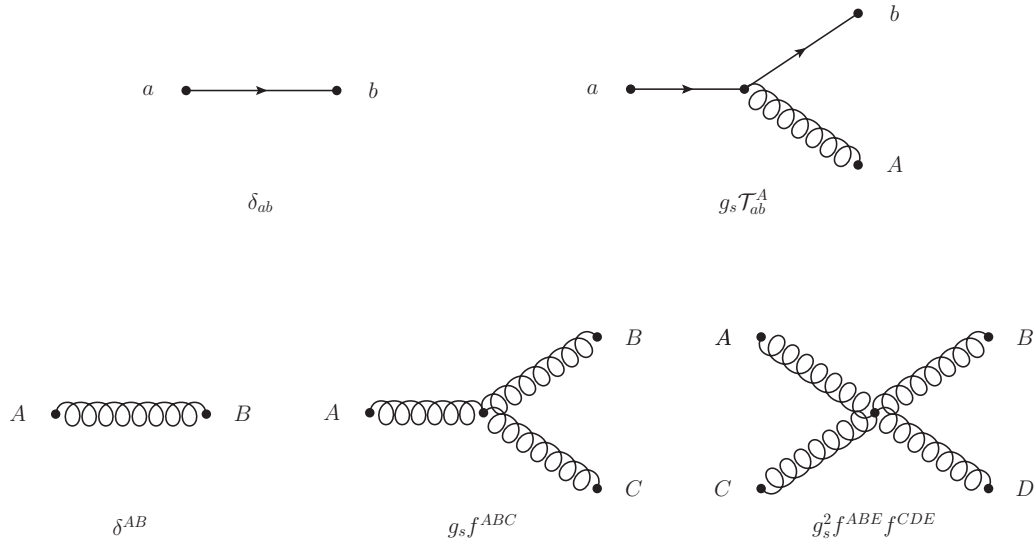


Figure 2.2: The fundamental Feynman rules of a free quark-field term (top left), quark-gluon interaction term (top right), free gluon-field term (bottom left), cubic gluon self-interaction term (bottom middle) and quartic gluon self-interaction term (bottom right). Taken from [15].

It is impossible to use perturbation theory on a gauge invariant Lagrangian without choosing a specific gauge in which to calculate. The usual gauge-fixing term is given by

$$\mathcal{L}_{gauge} = -\frac{1}{2\xi} (\partial^\mu A_\mu^A)^2 \quad (2.6)$$

where  $\xi$  may be any finite constant. This choice fixes the class of covariant gauges with  $\xi$  as the gauge parameter. As QCD is non-Abelian, the gauge fixing term must be supplemented by a ghost Lagrangian as

$$\mathcal{L}_{ghost} = \partial_\alpha \eta^{A\dagger} (D_{AB}^\mu \eta^B) \quad (2.7)$$

where  $\eta^A$  is a complex scalar field which obeys Fermi statistics. The ghost fields cancel unphysical degrees of freedom which arise due to using covariant gauges. This completes the QCD Lagrangian shown in equation 2.2.

The strength of an interaction is given by a fundamental parameter called the coupling constant  $\alpha$ . In QED, the coupling constant  $\alpha_e = e^2/4\pi = 1/137$  is constant. In contrast to this, in QCD, the coupling constant  $\alpha_S(Q) = g_s^2/4\pi$  is not constant and depends on the separation between the interacting particles. It increases with the increase in the distance or decrease in the energy scale  $Q$ . At large distances or low energies, the quarks can never be found as free particles but as color neutral bound states called hadrons. Hadrons are two types : mesons ( $q\bar{q}$ ) made up of quark-antiquark pair and baryons ( $qqq$ ) made from three (anti-)quarks. When the colored quarks and gluons within a hadron are pulled farther and farther apart, there is an increase in the strength of force between them. This results in creation of new quark-antiquark pair making difficult to liberate a free quark or gluon. This property of QCD is known as confinement. As it would take an infinite amount of energy to separate two quarks, they are forever bound into hadrons such as protons ( $uud$ ), neutrons ( $udd$ ). Although the gluons are massless, the confinement leads to the finite range of the strong interactions. On the other hand, at small distances, the quarks and gluons interact very weakly and are treated as free particles. This property is known as asymptotic freedom. This indicates that perturbation theory is only applicable at high energies or small distances.

### 2.2.1 Perturbative Quantum Chromodynamics

At high energies, the property of asymptotic freedom allows a perturbative treatment in QCD calculations. In perturbative Quantum Chromodynamics (pQCD), any observable  $X$  such as cross-section of a scattering process, can be written as a perturbative series in terms of coupling constant  $\alpha_S$  as :

$$X = \sum_{i=0}^N \alpha_s^n c_i = c_0 + \alpha_s^1 c_1 + \alpha_s^2 c_2 + \dots \quad (2.8)$$

where  $c_i$  are the perturbative coefficients. In a process, the pQCD calculation of  $X$  is determined by over the amplitudes of all Feynman diagrams. For a given Feynman diagram, the power of  $\alpha_S$  is determined by the number of vertices associated with quark-gluon or gluon-gluon interactions. A leading order (LO) prediction sums over only the lowest-order contribution whereas next-to-leading order (NLO) includes terms with an additional powers of  $\alpha_S$ . The next-next-to-leading order (NNLO) includes emission of another gluon or a virtual gluon loop. The different order of the QCD processes are shown in Fig. 2.3. The calculations become complex with the loop diagrams where the momenta of the virtual particles in a loop are not fully constrained by four-momentum conservation and the associated integrals are divergent. Such ultraviolet (UV) divergencies enter the calculations beyond LO due to loop or vertex corrections. These are overcome by a procedure known as renormalization, described in next Section. Apart from these, QCD also suffers from infrared and collinear divergences (IRC) due to the presence of massless gluons and neglected quark masses. These need to be handled in pQCD calculations. The observable to be studied must be IRC safe.

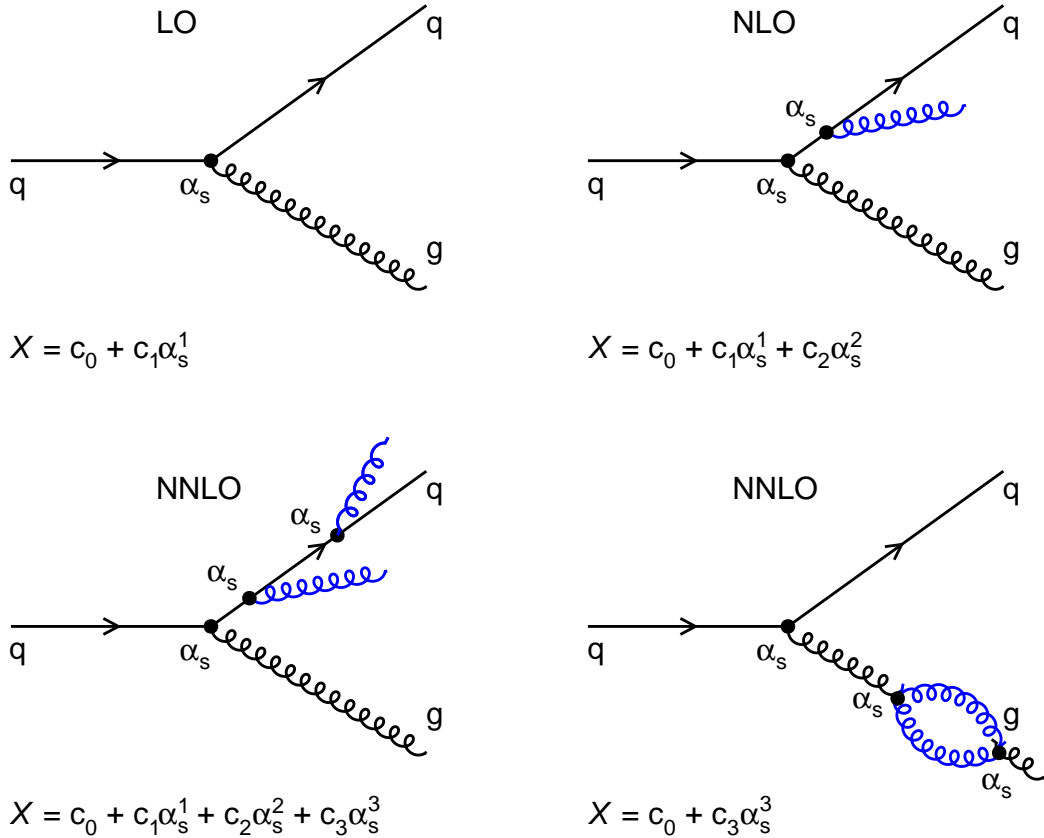


Figure 2.3: Feynman diagrams<sup>2</sup> showing leading-order (LO), next-to-leading order (NLO) and next-next-to-leading order (NNLO) processes in QCD along with the perturbative expansion of any observable  $X$  in powers of the strong coupling constant  $\alpha_S$ . At each successive step in perturbation series, the emission of an additional gluon take place.

## 2.2.2 Renormalization and Running of the Strong Coupling

The renormalization is a mathematical procedure which allows the finite calculation of momenta integrals of loop by removing UV divergences. It introduces a regulator for the infinities, the renormalization scale  $\mu_r$ . At first, the divergences are regularized temporarily by introducing a cut-off to the loop momenta at  $\mu_r$  scale. Then the free parameters of the Lagrangian, i.e. the coupling constant are redefined (renormalized) to absorb the UV divergences. Hence, both  $\alpha_S(Q)$  and observable  $X$  become a function of  $\mu_r$ . The exact dependence of  $\alpha_S(\mu_r^2)$  on  $\mu_r$  is described by the

---

<sup>2</sup>Drawn using ROOT

renormalization group equation (RGE), which determines the running of  $\alpha_s(\mu_r^2)$ . RGE states that the dependence of  $X$  on  $\mu_r$  must cancel, which is expressed mathematically as :

$$\mu_r^2 \frac{d}{d\mu_r^2} X \left( \frac{Q^2}{\mu_r^2}, \alpha_s(\mu_r^2) \right) = \left( \mu_r^2 \frac{\partial}{\partial \mu_r^2} + \mu_r^2 \frac{\partial \alpha_s(\mu_r^2)}{\partial \mu_r^2} \frac{\partial}{\partial \alpha_s(\mu_r^2)} \right) X = 0 \quad (2.9)$$

Using  $\beta(\alpha_s) = \mu_r^2 \frac{\partial \alpha_s(\mu_r^2)}{\partial \mu_r^2}$ , Eq. 2.9 can be re-written as

$$\left( \mu_r^2 \frac{\partial}{\partial \mu_r^2} + \beta(\alpha_s) \frac{\partial}{\partial \alpha_s(\mu_r^2)} \right) X = 0 \quad (2.10)$$

By setting the renormalization scale to the physical scale i.e.  $Q^2 = \mu^2$ ,  $X(1, \alpha_s(Q))$  is a solution to above equation.  $Q$ -dependence of the  $X$  is only from the renormalization of the theory and would not be present in the classical theory. Hence measuring the  $Q$ -dependence of  $X$  will directly probe the quantum structure of the theory. The  $\beta$  function in QCD has a perturbative expansion as :

$$\beta(\alpha_s) = -\alpha_s^2 \left( b_0 + b_1 \alpha_s + b_2 \alpha_s^2 + \mathcal{O}(\alpha_s^3) \right) \quad (2.11)$$

where  $b_0$ ,  $b_1$  and  $b_2$  are the 1-loop, 2-loop and 3-loop  $\beta$ -function coefficients encoding the dependence of the coupling on the energy scale and given in the modified minimal subtraction ( $\overline{\text{MS}}$ ) scheme [16, 17] as :

$$b_0 = \frac{33 - 2n_f}{12\pi}, \quad b_1 = \frac{153 - 19n_f}{24\pi^2}, \quad b_2 = \frac{77139 - 15099n_f + 325n_f^2}{3456\pi^3} \quad (2.12)$$

where  $n_f$  is the number of quark flavours with masses  $m_q$  smaller than the scale  $\mu_r$ . On integration of above equation, the energy dependence of  $\alpha_S$  is yielded. Neglecting

the higher orders, the first order solution of RGE is :

$$\alpha_s(\mu_r^2) = \frac{1}{b_0 \ln(\mu_r^2/\Lambda^2)} \quad (2.13)$$

with  $\Lambda$  as the constant of integration. It corresponds to the scale at which the perturbative coupling would become large and the perturbative series diverge. With  $b_0 > 0$ , the coupling becomes weaker at higher scales  $Q$ , i.e. the effective color charge gets smaller when the distance decreases. This leads to the asymptotic freedom. It is convenient to express  $\alpha_s$  at some fixed scale. As some of the best measurements come from  $Z^0$  decays, it is common practise to give the strong coupling at the scale of the  $Z$  boson mass as  $\alpha_s(M_Z)$ . So, Eq. 2.13 can be expressed as :

$$\alpha_s(\mu_r, \alpha_s(M_Z)) = \frac{\alpha_s(M_Z)}{1 + \alpha_s(M_Z) b_0 \ln(\mu_r^2/M_z^2)} \quad (2.14)$$

The parameter  $\alpha_s$  is a free parameter of the theory. It is deduced from experimental measurements and evolved to the scale of the  $Z$  boson. The current world average value of the strong coupling according to the PDG [18] reads as and is determined from hadronic lepton decays, lattice QCD calculations, deep inelastic scattering data, electron-positron annihilation processes and electroweak precision fits. Fig. 2.2 shows various determinations of the strong coupling from measurements at scales  $Q$ , which describe the running of the strong coupling up to the 1 TeV scale.

In the perturbative region, the first order solution of equation 2.11 is given by

$$\alpha_s(Q) = \frac{\alpha_s(\mu)}{1 + \alpha_s(\mu)bt}, \quad (2.15)$$

Note that as  $t$  becomes large,  $\alpha_s$  approaches 0. In other words, as  $Q^2$  increases  $\alpha_s(Q)$  decreases, allowing the quarks to behave as free particles within the hadron,

a property known as asymptotic freedom.

The renormalization scale is not a truly arbitrary parameter, it should be chosen to be on the order of the hard scale  $Q \sim E_T$  because perturbation theory is only valid for a small range of values for  $\mu$ . Figure ?? shows how a typical cross section changes with the choice of renormalization parameter. If the renormalization parameter becomes too small,  $\mu$  less than  $\sim E_T/2$ , LO and NLO calculations differ greatly. This implies that higher order terms are not small so perturbation theory is not valid. For values of  $\mu \sim E_T$ , perturbation theory works well because the series can be expanded about a small value. LO and NLO calculations differ slightly, so a perturbative expansion is valid since adding an additional higher order term introduces only a small change. For  $\mu$  greater than  $\sim 2E_T$ , LO and NLO again begin to diverge causing perturbation theory to be no longer valid.

By using perturbative QCD, the change of the coupling constant with scale can be calculated, but it cannot give an absolute value for  $\alpha_s$ . Therefore, a fundamental parameter can be chosen as some convenient reference scale which is large enough to be in the perturbative region. By convention this parameter is defined as  $\Lambda$  and is a constant of integration defined as

$$\ln \frac{Q^2}{\Lambda^2} = - \int_{\alpha_s(Q)}^{\infty} \frac{dx}{\beta x} \quad (2.16)$$

$\Lambda$  represents the scale at which  $\alpha_s(Q)$  becomes strong. Using  $\Lambda$ ,  $\alpha_s(Q)$  can be written as

$$\alpha_s(Q) = \frac{1}{b \ln(Q^2/\Lambda^2)} \quad (2.17)$$

### 2.2.3 Factorization and Parton Distribution Functions

## 2.3 Hadron Collisions

### 2.3.1 Parton Shower

### 2.3.2 Hadronization

### 2.3.3 Underlying Event and Multi-Parton Interactions

## 2.4 Jets

### 2.4.1 Jet Algorithms

### 2.4.2 Jet Properties



## 2.5 Leading order and next-to-leading order calculations

A perturbative expansion in  $\alpha_s$  is generally performed to calculate measurable quantities in QCD. Physical quantities are calculated by separating processes at different orders in  $\alpha_s$ . At leading order only two jets can exist. Calculations at LO allow for only  $gg \rightarrow gg$ ,  $qq \rightarrow qq$ ,  $qg \rightarrow qg$ ,  $q\bar{q} \rightarrow q\bar{q}$ ,  $q\bar{q} \rightarrow gg$ , and  $gg \rightarrow q\bar{q}$ . Figure shows some of the diagrams which contribute to leading order parton-parton scattering. Each vertex in these diagrams is proportional to  $\alpha_s$ . Since each diagram at LO has two vertices, calculations can only be performed at order  $O(\alpha_s^2)$ . Typically leading order calculations depend heavily upon the choice of renormalization scale, leading to uncertainties in most LO calculations of about 30%. In order to reduce the theoretical uncertainties, higher order diagrams can be introduced. As more terms are included in the perturbative expansion, the dependence on  $\mu$  decreases, reducing the theoretical uncertainties.

At next-to-leading order, calculations may include three jet events, because diagrams such as  $gg \rightarrow ggg$  are now possible. NLO must also include a larger number of two jet diagrams arising from loops. Figure ?? shows some of the diagrams contributing to NLO parton-parton scattering. At NLO, each diagram has either three or four vertices, allowing calculations of order  $O(\alpha_s^3)$  to be performed. Terms which are of order  $O(\alpha_s^4)$  are ignored. NLO is much less sensitive to the renormalization scale. Calculations at this order typically have errors of  $\sim 10\%$ .

Calculating quantities to all orders in  $\alpha_s$  is the ultimate goal. However, it becomes increasingly difficult to calculate higher order processes. At NLO, calculations require over 100 separate diagrams. The number of diagrams necessary to calculate higher order corrections is large and the mathematics and computing time is foreboding. Currently only exact NLO calculations are available.

## 2.6 Parton Distribution Functions

In addition to needing a renormalization scale to calculate physical quantities in QCD, parton distribution functions are also required. Parton distribution functions parameterize the quark and gluon momentum distribution within the proton as a function of  $Q^2$ , where  $Q$  is the momentum transferred. They are measured by deep inelastic scattering experiments, in which a high energy lepton is scattered on a hadron target. By measuring the cross section of  $lp \rightarrow lX$  and  $\nu p \rightarrow lX$ , the parton distribution functions can be found. Since parton distribution functions are an experimentally measured quantity, different parameterizations exist. For this study we use the most recent parameterizations.

# Chapter 3

## Experimental Setup

The hadron colliders aim at search for elementary particles and their interactions as predicted in the Standard Model or theories beyond the Standard Model. For the same beam energy, higher center-of-mass energy can be achieved by the hadron colliders as compared to fixed target experiments. Due to the availability of very high center-of-mass energy for the collisions, it becomes possible for the researchers to understand the fundamental structure of the universe deeply and to look back in its history. The precise measurement of mass of the Z and W boson discovered by the UA1 and UA2 experiments was done at the Large Electron-Positron (LEP) collider. The discovery of top quark and an acute measurement of its mass was performed by the proton-antiproton collider Tevatron at FNAL. The search for the long awaited Higgs boson was carried out by the currently running most powerful accelerator, the Large Hadron Collider (LHC). Still many questions related to the the nature of dark matter, the existence of supersymmetry (SUSY) or the extra dimensions are yet to be answered.

The European Organization for Nuclear Research (CERN) is a world-class fundamental physics research organization founded in 1954. In the beginning, it concentrated on pure physics research to understand the inside of the atom, justifying the word “nuclear” in name. At present, the main area of research at CERN

is particle physics - the study of the fundamental constituents of matter and the forces of interactions acting between them. To complete this task, several particle accelerators have been built by CERN to explore the physics at the TeV energy scale.

### 3.1 The Large Hadron Collider

The Large Hadron Collider (LHC) [19] is the world's biggest and the most powerful particle accelerator and collider built by CERN. It occupies the 27 km circumference circular tunnel (between the border of France and Switzerland), previously used by LEP collider [20], at a depth ranging from 50 to 175 metres (164 to 574 ft) underground. Two beams of particles of the same kind, either protons or lead or xenon ions, are accelerated in direction opposite to each other. 1,232 dipole magnets maintain the beams in their circular path and 392 quadrupole magnets keep the beams focused to increase the probabilities of interaction between the particles. Since this thesis is based on the proton-proton (pp) collisions data, the main focus is on protons.

The protons pass through a series of accelerators which increase their energy successively before their injection into the main ring of LHC. Figure 3.1 gives an overview of the various accelerators and detectors comprising the complex structure of the LHC. The protons are obtained by stripping of electrons from hydrogen gas atoms using an electric field. The protons are accelerated up to 100 keV through a radiofrequency quadrupole which provides the first focusing and a further acceleration to 750 keV energy. The linear particle accelerator (LINAC2) increases the energy of protons to 50 MeV. Then these protons are injected into the Proton Synchrotron Booster (PSB) in the form of bunches where they get accelerated to 1.4 GeV energy. The energy of protons is further enhanced to 25 GeV by Proton Synchrotron (PS) and then to 450 GeV by the Super Proton Synchrotron (SPS). Finally

the protons are injected into two beam pipelines of the main LHC ring where their energy increases to the collision energy. In head on collisions for colliding beams of the same mass particles, the center of mass system and the laboratory system coincide and the total center of mass energy is twice the energy of the beams.

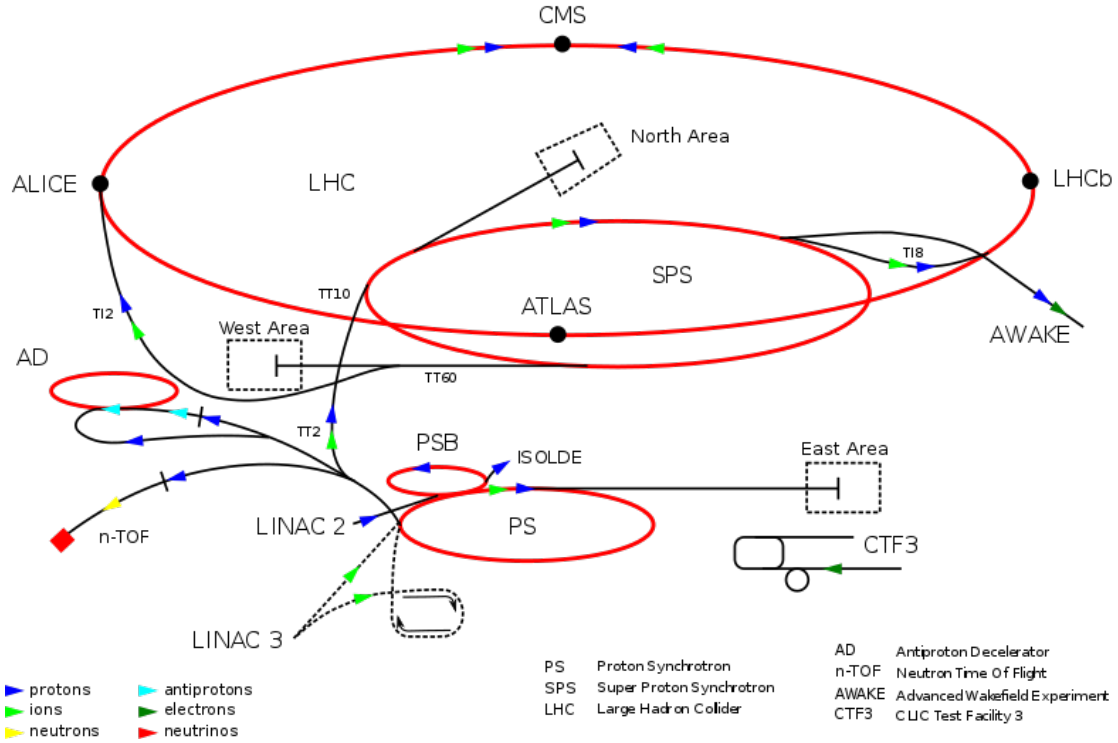


Figure 3.1: Overview of the different experiments of the Large Hadron Collider (LHC), a complex particle accelerator and collider located at CERN<sup>3</sup>.

The accelerated beams are made to collide at four interaction points around which six detectors : ALICE (A Large Ion Collider Experiment) [21], ATLAS (A Toroidal LHC Apparatus) [22], CMS (Compact Muon Solenoid) [23–25], LHCb (Large Hadron Collider for Beauty) [26], LHCf (Large Hadron Collider forward) [27] and TOTEM (Total, elastic and diffractive cross-section measurement) [28], are located. The CMS and ATLAS are the two general purpose detectors dedicated to the search of the Higgs boson, existence of super-symmetry (SUSY) and also looking

<sup>3</sup>Source : [https://en.wikipedia.org/wiki/Large\\_Hadron\\_Collider](https://en.wikipedia.org/wiki/Large_Hadron_Collider)

for extra dimensions. The ALICE is a heavy-ion detector which collides lead ions to study quark-gluon plasma, a state of matter believed to be present just after the Big Bang. The LHCb experiment will explore the differences between matter and anti-matter and new physics through b-quark (beauty) studies. TOTEM experiment is dedicated to cross-section measurements whereas LHCf focuses on forward physics.

The LHC successfully injected the first protons on September 10, 2008 but after few days magnetic quench occurred in about 100 bending magnets leading to a loss of  $\sim 6$  tonnes of liquid helium. The low-energy beams circulated in the tunnel for the first time on November 20, 2009 and after three days, the first particle collisions took place in all four detectors at  $\sqrt{s} = 450$  GeV. The LHC achieved 1.18 TeV energy per beam on November 30, 2009 and become the world's highest energy particle accelerator leaving behind the Tevatron with record of 0.98 TeV per beam for eight years. The pp collisions at  $\sqrt{s} = 2.36$  TeV were recorded around December 15, 2009. On March 19, 2010, the beam energy was ramped up to 3.5 TeV, resulting in the first pp collisions at  $\sqrt{s} = 7$  TeV on March 30, 2010. The beam energy was kept at 3.5 TeV throughout 2011, and increased to 4 TeV in 2012. After a long shutdown for two years, the LHC restarted in 2015 and collided the proton beams at a much higher centre-of-mass energy of 13 TeV and is running successfully till now. In the coming years, protons will be made to collide at a designed  $\sqrt{s} = 14$  TeV with luminosity up to  $10^{34}$  cm $^{-2}$ s $^{-1}$ . In this thesis, work has been carried out using the pp collisions data collected by the CMS detector at  $\sqrt{s} = 8$  TeV in the year of 2012.

## 3.2 Luminosity Measurement

Luminosity ( $\mathcal{L}$ ) is one of the most important parameters of an accelerator which characterizes its performance. It gives the rate at which collisions occur and given by the number of collisions produced in a detector per cm $^2$  and per second. Cross-

section ( $\sigma$ ) is a measurement of the probability that an event will occur. It is related to total number of events  $N$  of a process over a time period  $T$  and  $\mathcal{L}$  as :

$$N = \int_0^T \mathcal{L} \sigma dt = \mathcal{L}_{int} \sigma \quad (3.1)$$

where  $\int_0^T \mathcal{L} dt = \mathcal{L}_{int}$  is the total integrated luminosity. It is expressed in units of area, usually in barn $^{-1}$  and gives a direct indication of the number of produced events for a process. For example, an integrated luminosity of 10 fb $^{-1}$  means that 10 events are produced in a process with cross-section equal to 1 fb.

The luminosity depends on the particle beam parameters and is given by :

$$\mathcal{L} = \frac{N_p^2 N_b f_{rev} \gamma F}{4\pi \epsilon_n \beta^*} \quad (3.2)$$

where  $N_p$  is the number of particles per bunch,  $N_b$  is the number of bunches per beam,  $f_{rev}$  is the revolution frequency of the beam,  $\gamma$  is the relativistic gamma factor and  $F$  gives the geometric luminosity reduction factor. The effective collision area of the two beams is related to the normalized transverse beam emittance  $\epsilon_n$  and the value of the betatron function  $\beta^*$  at the interaction point.

The CMS experiment constantly monitors the instantaneous luminosity delivered by LHC which is shown versus time in Fig. 3.2 for proton-proton collisions at nominal center-of-mass energy for the years 2010-2017. The relative instantaneous luminosity is calculated by using two methods [29] : Hadron Forward (HF) method by measuring the particle flux in the hadron forward calorimeter and by counting the number of reconstructed vertices in the pixel tracker. The absolute luminosity measurement relies on van-der-Meer scans done in special runs of the LHC [30]. The uncertainty on the luminosity measured for 2012 data set is 2.5% (syst.) and 0.5% (stat.).

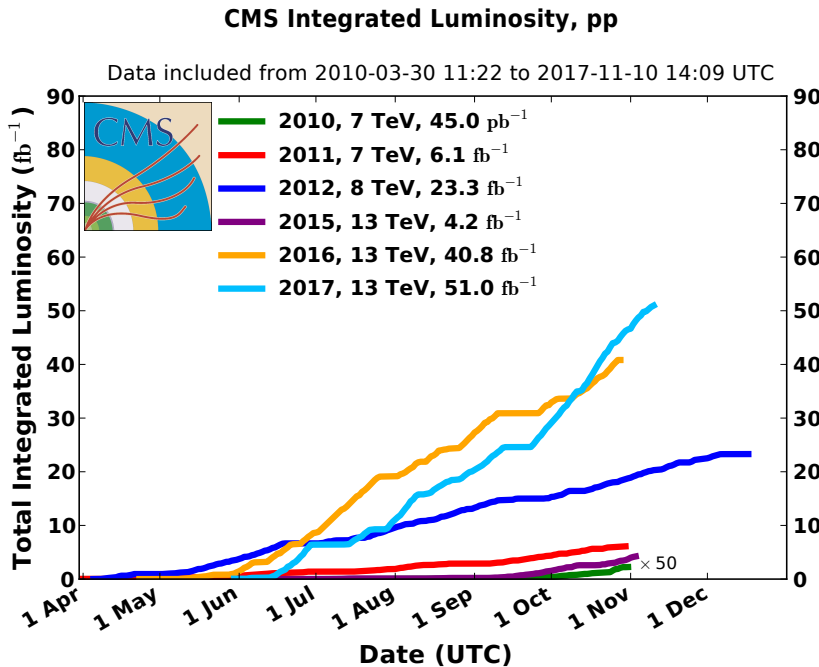


Figure 3.2: The integrated luminosity, delivered to CMS during stable beams for proton-proton collisions at nominal center-of-mass energy, is shown versus time for data-taking in 2010 (green), 2011 (red), 2012 (blue), 2015 (purple), 2016 (orange) and 2017 (light blue) run periods of the LHC<sup>4</sup>.

### 3.3 The Compact Muon Solenoid

The Compact Muon Solenoid (CMS) detector is a general purpose detector located at the interaction point 5 (P5) of the main LHC ring, near the village of Cessy in France. The name of CMS comes from its compact size with main emphasis on the detection of muons and enclosed within high solenoidal magnetic field. The CMS detector aims at identifying the different types of particles produced in proton-proton and heavy ion collisions and measuring their energies and momenta. This is achieved by concentric layers of different sub-detectors arranged in a cylindrical complex structure with 21.6 m length and 15 m diameter. The silicon-based tracker surrounds the the interaction point and forms the innermost layer. It is surrounded

<sup>4</sup>Source : <https://twiki.cern.ch/twiki/bin/view/CMSPublic/LumiPublicResults>

by a scintillating crystal electromagnetic calorimeter (ECAL) and a sampling hadron calorimeter (HCAL) which are enclosed inside the superconducting solenoid. Outside the magnet lies the large muon detectors embedded inside an iron yoke. The three dimensional view of the CMS detector along with its components is presented in Fig. 3.3. The CMS was constructed in parts at ground and assembled later on

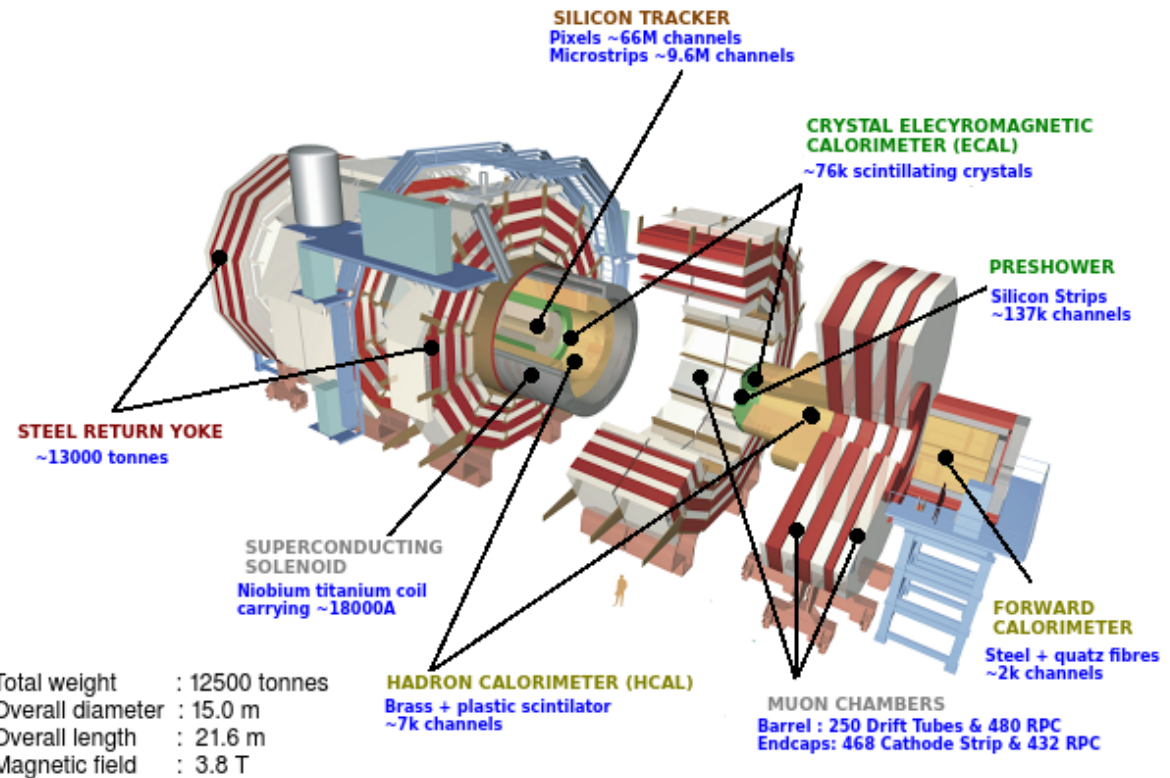


Figure 3.3: The three dimensional view of the CMS detector along with its sub-detector components<sup>5</sup>.

in the cavern. The components are easily accessible for upgrades or repairs as the detector can be opened up into movable slices. Figure 3.4 shows the front view of the CMS detector differentiating individual components which contribute to event reconstruction. The path of reconstructed particles is represented by dashed (invisible track) and solid (visible track) lines for different particle classes : photons ( $\gamma$ ),

<sup>5</sup>Source : <https://orbiterchspacenews.blogspot.in/2013/04/cern-cms-prepares-for-future.html>

muons ( $\mu^\pm$ ), electrons ( $e^-$ ), neutrons (n) and charged hadrons (pions  $\pi^\pm$ ).

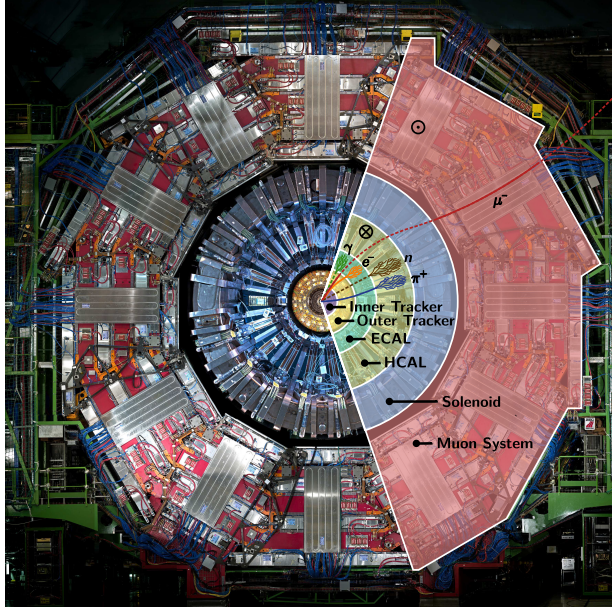


Figure 3.4: Front view of the CMS detector along with its components : inner tracker, outer tracker, electromagnetic calorimeter, hadronic calorimeter, solenoid and muon system. The path of different particles detected by dedicated sub-detectors are shown by dashed (invisible track) and solid (visible track) lines.  $\otimes$  and  $\odot$  gives the direction of magnetic field inside the solenoid and in the return yoke, respectively. Taken from [25].

A brief overview of the CMS detector has been presented and the details of the its design as well as physics performance are available in Ref. [24, 25]. Before going into the details of each sub-detector, first the CMS coordinate system is described in the next section.

### 3.3.1 Coordinate System

CMS uses right-handed coordinate system, illustrated in Fig. 3.5, having origin at the nominal interaction point (IP) of the collision inside the detector. The  $x$ -axis points horizontally from the IP, towards the center of the LHC ring, the  $y$ -axis vertically upwards and the  $z$ -axis along the beam direction towards the Jura mountains. The radial coordinate in  $x$ - $y$  plane is denoted by  $r$ . Following customary polar coordinate conventions : the azimuthal angle  $\phi$  is measured from the  $x$ -axis in

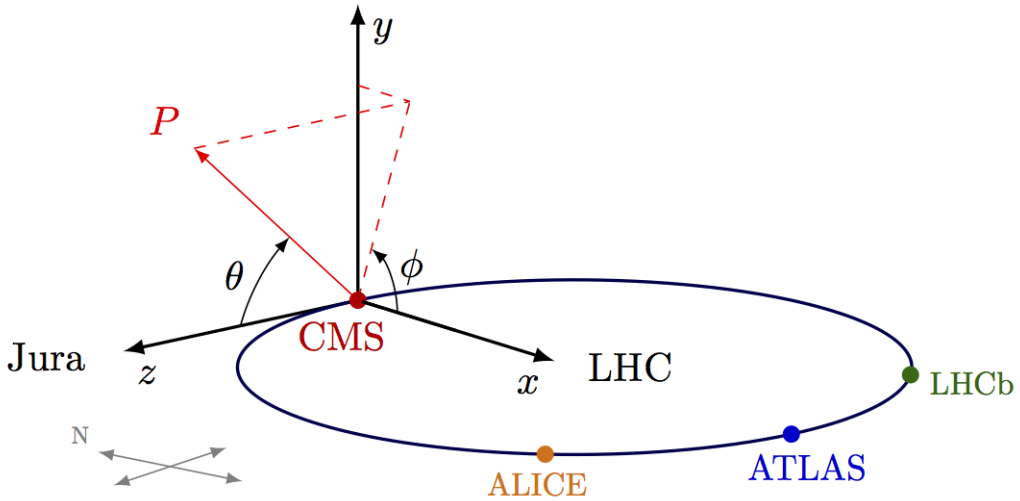


Figure 3.5: The right-handed coordinate system used by the CMS detector<sup>6</sup> with origin at the interaction point (IP),  $x$ -axis points horizontally from the IP towards the center of the LHC ring, the  $y$ -axis vertically upwards and the  $z$ -axis along the beam direction towards the Jura mountains,  $\phi$  as the azimuthal angle measured from the  $x$ -axis in the  $x$ - $y$  plane and  $\theta$  as the polar angle calculated from the  $z$ -axis in the  $z$ - $y$  plane.

the  $x$ - $y$  plane as  $\phi = \tan^{-1}(\frac{y}{x})$  where  $\phi = 0$  points to the  $+x$  axis and  $\phi = \pi/2$  points to the  $+y$  axis. The polar angle  $\theta$ , is calculated from the  $z$ -axis in the  $z$ - $y$  plane as  $\theta = \tan^{-1}(\frac{x^2 + y^2}{2})$  with  $\theta = 0$  corresponding to the  $+z$  direction and  $\theta = \pi$  to the  $-z$  direction. The quantities pseudorapidity  $\eta$  and the rapidity  $y$  are preferred over the angles  $\theta$  and  $\phi$ . The pseudorapidity and rapidity are given by Eq. 3.3. Both the quantities are equal for massless particles.

$$\begin{aligned}\eta &= -\ln\left(\tan\left(\frac{\theta}{2}\right)\right) \\ y &= \frac{1}{2} \ln\left(\frac{E + p_z}{E - p_z}\right)\end{aligned}\tag{3.3}$$

The difference between rapidities  $\Delta y$  is invariant under longitudinal Lorentz boost whereas it does not hold for  $\eta$ . Hence  $y$  is considered in this thesis. The angular

<sup>6</sup>Source : [https://wiki.physik.uzh.ch/cms/latex:example\\_spherical\\_coordinates](https://wiki.physik.uzh.ch/cms/latex:example_spherical_coordinates)

distance between the two particles is defined by  $\Delta R = \sqrt{(\Delta\eta)^2 + (\Delta\phi)^2}$ . The momentum component transverse to the direction of beam  $p_T$ , is computed from the  $x$ - and  $y$ -components as  $p_T = \sqrt{p_x^2 + p_y^2}$  and the transverse energy is given by  $E_T = E \sin\theta$ . After introducing the CMS coordinate system, further the detector subsystems are described briefly in the following sections. A longitudinal section of the CMS detector in the  $y$ - $z$  plane, shown in Fig. 3.6, locates the different subsystems along with the superconducting solenoid.

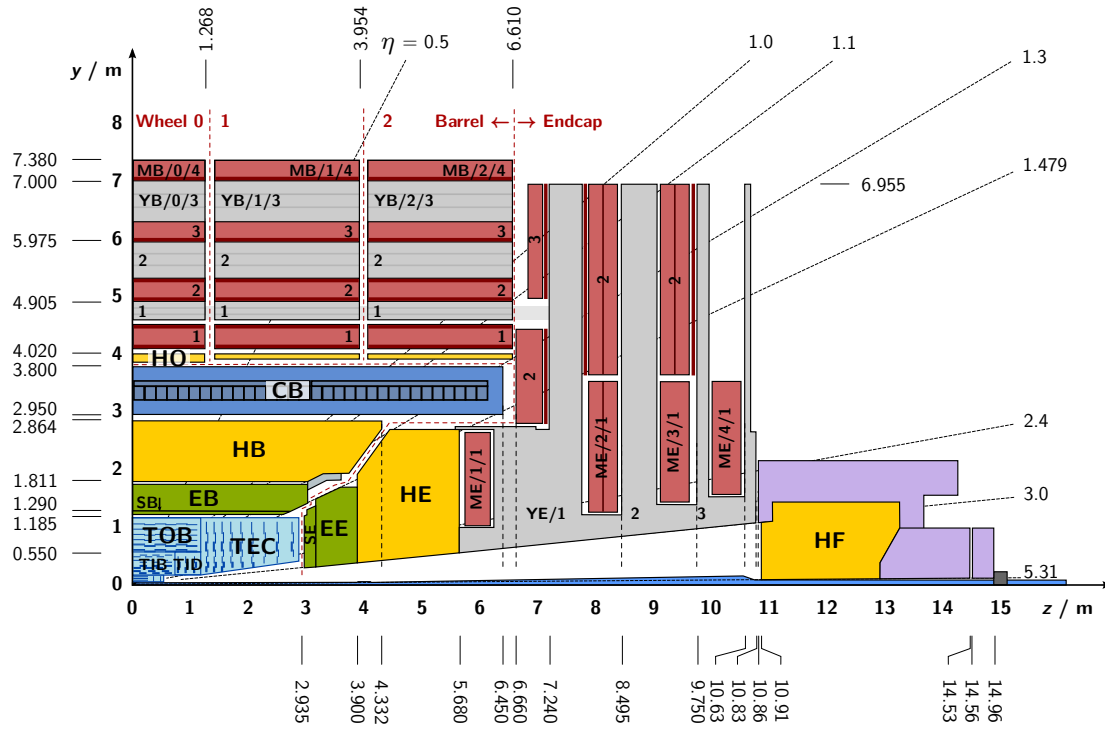


Figure 3.6: Longitudinal section of the CMS detector in the  $y$ - $z$  plane<sup>7</sup>. It shows the tracking detector (TIB, TID, TOB, TEC) close to the nominal interaction point at  $(0,0)$ , the electromagnetic (EB, EE) and hadronic (HB, HE, HO, HF) calorimeters. The coil of the solenoid magnet (CB) surrounds the inner barrel region. The iron return yoke (YB, YE) is interleaved with the muon chambers (MB, ME).

<sup>7</sup>Source : <http://cds.cern.ch/record/1747055>

### 3.3.2 Inner Tracker System

The charged particles produced from the LHC collisions leave their trajectories as they move outward from the interaction point. The particle flux within the detector decreases as  $1/r^2$ . So the tracks of the particles need to be measured as close to the collision point as possible and in a precise manner. The innermost tracking system of the CMS consisting of silicon detectors measures the hits of charged particles. It surrounds the interaction point and has a cylindrical volume of length of 5.8 m and a diameter of 2.5 m and covers a pseudorapidity range up to  $|\eta| < 2.5$ . When charged particles pass through the silicon detector material, small ionization currents are produced which are detected as a hit. Such multiple hits when combined, reconstruct the track which gives the information about the direction and transverse momentum  $p_T$  of the charged particle. Silicon detectors have a much higher resolution in tracking charged particles as compared to the older ones such as cloud chambers or wire chambers. CMS inner tracking system shown in Fig. 3.7 consists of two sub-systems :

**Pixel Detector** - A pixel detector lying close to the beam pipe have three concentric barrel layers at radii of 4.4, 7.3 and 10.2 cm from the beam pipe. It has two disks of pixel modules on each side of barrel. At the LHC design luminosity of  $10^{34} \text{ cm}^{-2}\text{s}^{-1}$ , about 1000 particles from more than 20 overlapping proton-proton interactions traverse through the tracker for each bunch crossing, i.e. every 25 ns. The size of each pixel is  $100 \mu\text{m} \times 150 \mu\text{m}$  which gives an average occupancy of  $10^{-4}$  per bunch crossing. By taking an advantage of the large Lorentz effect, the pixel tracker has a resolution of  $10 \mu\text{m} \times 20 \mu\text{m}$  needed for a precise determination of the primary and secondary vertices and the required momentum resolution.

**Strip Detector** - After coming out of the pixel detector the charged particles pass through ten layers of silicon strip detectors, reaching out to a radius of 130 cm. The silicon strip detector consists of four inner barrel (TIB) layers assembled

in shells with two inner endcaps (TID), each composed of three small discs. The outer barrel (TOB) consists of six concentric layers. Finally two endcaps (TEC) close off the tracker. Each part has silicon modules designed differently for its place within the detector. The strip detector measures the particle tracks with a reduced resolution of  $23\text{ }\mu\text{m}$  reflecting the smaller particle flux at larger distances from the interaction point. The active silicon area of CMS tracker is about  $200\text{m}^2$  which

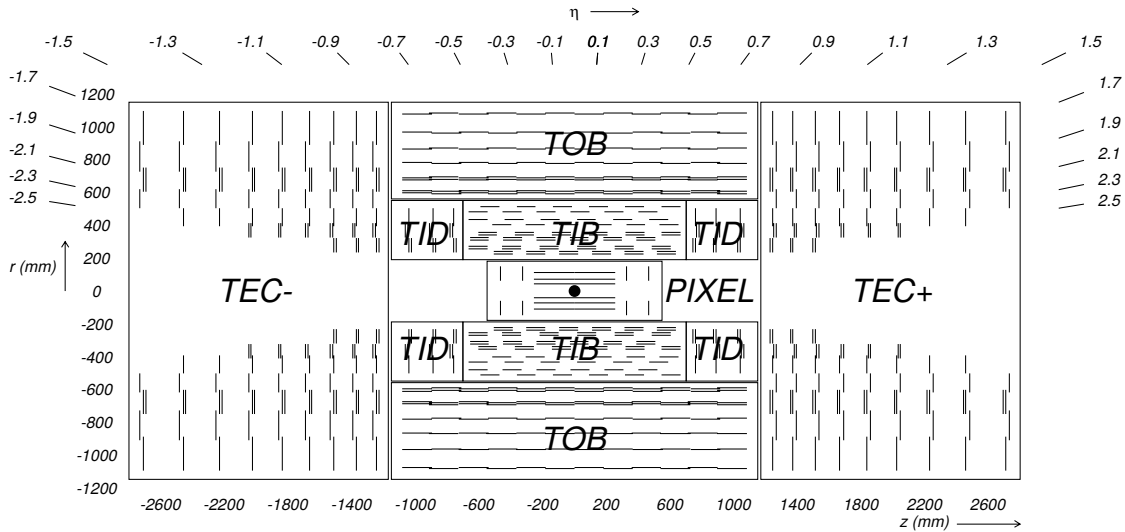


Figure 3.7: The longitudinal section of the inner tracking system consisting of the silicon pixel detector and the silicon strip detector is shown in  $r$ - $z$  plane. The silicon strip detector has four components : The Tracker Inner Barrel (TIB) complemented by the Tracker Inner Disks (TID) which are further surrounded by the Tracker Outer Barrel (TOB) in barrel region. Tracker End Cap (TEC) covers high  $\eta$  ranges up to  $\eta = 2.5$ . Taken from [23].

makes it the largest silicon tracker. Along with the measurement of tracks, the energy also needs to be measured for which the calorimeters are present outside the tracker. The tracker should interfere with the particles to a minimum extent so that their momentum can be measured precisely but to measure their energy, they are required to interact with the calorimeters fully.

### 3.3.3 Electromagnetic Calorimeter

The electromagnetic calorimeter (ECAL) is a homogeneous and hermetic calorimeter used to slow down the produced photons and electrons/positrons and measure their energy by absorb them into the detector material. ECAL consists of 61200 lead tungstate ( $\text{PbWO}_4$ ) crystals in the barrel part and 7324 crystals in each of the two endcaps.  $\text{PbWO}_4$  is a very dense material with a short radiation length of  $X_0 = 0.89$  cm and covers the pseudorapidity up to  $|\eta| < 3.0$ . The particles interact with matter and produce electromagnetic shower through the subsequent processes of bremsstrahlung and electron-positron pair production. The energy of the particles deposited by Compton scattering and the photoelectric effect causes excitation of the material atomic state and the emission of photons. These photons are detected by silicon avalanche photo diodes (APDs) in the barrel region and vacuum phototriodes (VPT) in the end-cap region. The number of created photons gives the direct measure of energy of the incident particle. The incorporation of oxygen makes it highly transparent and enables to emit scintillation light. The small Molière radius of 2.19 cm gives a fine granularity. These properties leads to compact size of ECAL and can be placed easily within the solenoid magnet.

Figure 3.8 presents a geometric view of ECAL in the  $y$ - $z$  plane showing the arrangement of different parts of ECAL : the ECAL barrel (EB) extending up to  $|\eta| < 1.479$  using more than 60000 crystals and ECAL endcaps (EE) covering the region  $1.479 < |\eta| < 3.0$  with an additional 15000 crystals. The preshower detectors (ES) made of lead absorbers and silicon detectors are put in front of the endcaps to distinguish high energetic single photons from low energetic photon pairs originating from neutral pions decays.

The relative energy resolution of the ECAL has been measured to be [31] :

$$\left( \frac{\sigma(E)}{E} \right)^2 = \left( \frac{2.8\%}{\sqrt{E}} \right)^2 + \left( \frac{12\%}{E} \right)^2 + \left( 0.30\% \right)^2 \quad (3.4)$$

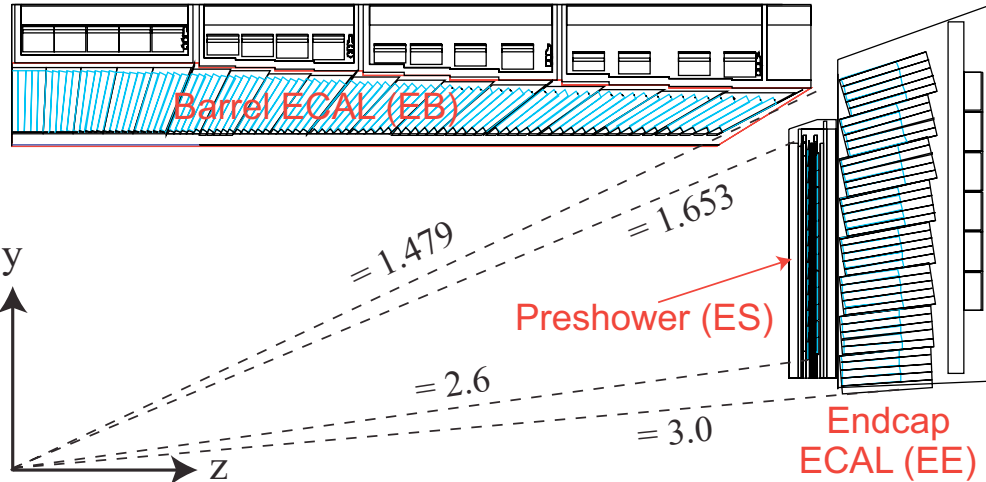


Figure 3.8: A geometric view of one quarter of the electromagnetic calorimeter (ECAL) in  $y$ - $z$  plane showing the arrangement of sub-modules covering the barrel region (EB) and the endcaps (EE). ECAL is complemented with preshower detector (ES) mounted in front of the endcaps. Taken from [24].

where  $E$  is the energy in GeV. The first term is the stochastic component caused by fluctuations in lateral shower containment and in the energy deposited in the preshower absorber. The second term is the contribution by noise and the last is the constant term comes from the non-uniformity of the longitudinal light collection, inter-calibration errors, and leakage of energy from the back of the crystal.

### 3.3.4 Hadronic Calorimeter

At CMS, the major fraction of the produced particles in proton-proton collisions is hadrons. The combined CMS calorimeter system measures directions and energies of quarks, gluons and neutrinos by measuring the energy and direction of particle jets. The neutral hadrons do not leave track and hence their energy is measured by taking into account the missing transverse energy ( $E_T^{\text{miss}}$ ). The determination of  $E_T^{\text{miss}}$  is a crucial tool in searching the new particles and phenomena. The hadron calorimeter (HCAL) are particularly important in the identification of hadron jets, neutrinos as well as electrons, photons and muons in conjunction with the ECAL

and the muon system. Hence HCAL is an essential sub-system of the CMS detector and contributes to most of CMS's physics studies.

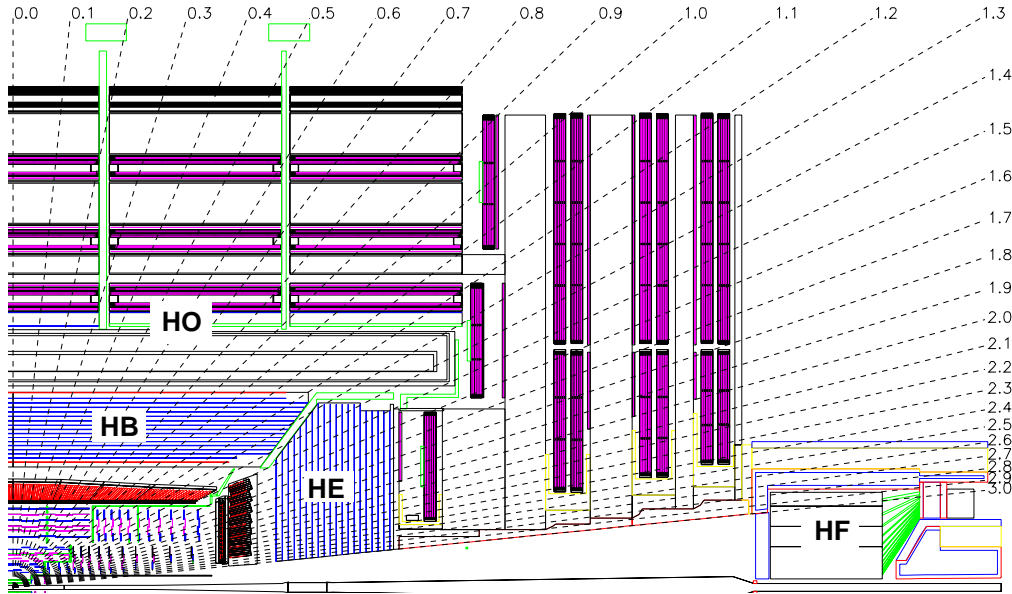


Figure 3.9: Longitudinal view of one quarter of the hadronic calorimeter (HCAL) detector in  $r$ - $\eta$  plane showing its different parts : hadron barrel (HB), hadron outer (HO), hadron endcap (HE) and hadron forward (HF). Taken from [23].

HCAL is a sampling calorimeter installed inside the solenoid coil. It is made up of non-magnetic brass absorber having a short interaction length of  $\lambda_I = 16$  cm interleaved with plastic scintillators having wavelength-shifting (WLS) fibres as readout. The hadrons produced with high energy showers a large number of pions and nucleons by inelastic interactions. The hadronic shower spreads more than the electromagnetic showers because of large transverse momentum of the secondary particles. As the energy of the particles is lower than a certain threshold, the ionization and low-energy hadronic processes come into play. The active scintillation material gets excited and emits blue-violet light. All scintillators are connected to photodiodes using wavelength shifters which read out the signals and pass them to the data acquisition system. The longitudinal view of one quarter of the HCAL presented in Fig. 3.9 shows the different parts :

**Hadron Barrel -** The hadron barrel (HB) is divided into two identical half barrel sections on either side of the interaction point. Each half barrel is made of 18 azimuthal wedges which are further divided into four azimuthal sectors each giving a granularity of  $\Delta\phi = 0.087$ . In  $z$  direction, the plastic scintillators are divided into 16 intervals of granularity  $\Delta\eta = 0.087$ . HB covers the region up to  $|\eta| < 1.305$  and overlaps with endcaps for  $1.305 \leq |\eta| \leq 1.392$ . Since HB has the highest resolution ( $\Delta\eta \times \Delta\phi = 0.087 \times 0.087$ ), it constitutes the optimal region for a data-driven calibration of the jet energy scale. The thickness of the HCAL amounts to 7-11 interaction lengths and which should be sufficient enough to stop nearly all hadrons in the calorimeter.

**Hadron Outer -** The total amount of material in barrel region to absorb the hadronic shower is not sufficient. This requirement is fulfilled by placing an outer hadron (HO) calorimeter as a tail catcher on top of the coil of the magnet. The HO utilizes the solenoid coil as an additional absorber equal to  $1.4/\sin\theta$  interaction lengths and measures the tails of hadron showers penetrating the HB and the coil. Since the HO is physically located inside the muon system, it is strongly constrained by its geometry. The muon system is subdivided into 5 rings along the  $z$ -axis. Each of these rings is 2.536 m wide in  $z$ -direction and the HO is placed as first sensitive layer in these rings, with a scintillator thickness of 10 mm. The central ring ( $\eta = 0$ ) has two scintillator layers placed on each side of 19.5 cm thick iron layer.

**Hadron Endcap -** The hadron endcaps (HE) extends the pseudorapidity range up to  $|\eta| < 3.0$ , a region containing about 34% of the particles produced in the final state. The granularity in  $\Delta\eta \times \Delta\phi$  is  $0.087 \times 0.087$  up to  $|\eta| < 1.6$  and  $0.17 \times 0.17$  for  $|\eta| > 1.6$ . The usage of non-magnetic material in order to not disturb the magnetic field and the close distance to the beam line were the main challenges faced during the construction of the HE. The continuous radiation damages decrease the

detector response which need to be corrected and monitored at regular intervals.

**Hadron Forward -** The hadron forward (HF) calorimeter lies  $2.8 < |\eta| < 5.2$  region and is placed more closer to the beam pipe at distance of  $z = \pm 11.2$  m from the interaction point. It is essentially a cylindrical steel structure with an outer radius of 130.0 cm which is azimuthally subdivided into 36  $20^\circ$  modular wedges. The HF is made of 5 mm thick grooved steel plates which have quartz fibers inserted into the grooves. The fibres run parallel to the beam line which are bundled to form  $0.175 \times 0.175$  ( $\Delta\eta \times \Delta\phi$ ) towers. HF detects the jets with very high  $\eta$  and the hadronization products of the beam remnants. It is built using iron absorbers and quartz fibers as active material, which measures the emitted Cerenkov light and produces the signal in the photomultipliers (PMT).

The relative hadronic energy resolution of the barrel HCAL and ECAL combination can be parametrized as :

$$\left(\frac{\sigma(E)}{E}\right)^2 = \left(\frac{a}{\sqrt{E}}\right)^2 + b^2 \quad (3.5)$$

with a stochastic term  $a$  and a constant term  $b$ . These values have been measured [32] as  $a = (0.847 \pm 0.016) \sqrt{\text{GeV}}$  and  $b = 0.074 \pm 0.008$  whereas for HF the measured values are  $a = 1.98 \sqrt{\text{GeV}}$  and  $b = 0.09$ .

### 3.3.5 Superconducting Magnet

The superconducting magnet is the key feature of the CMS detector which is 13m long and 6m in diameter. Its refrigerated superconducting high-purity aluminium-stabilized niobium-titanium coils cooled at 4 Kelvin produces a magnetic field of 4 Teslas (T). The magnet will run at 3.8 T in order to maximize its lifetime. This intense solenoidal field makes the compactness and cylindrical symmetry of the detector possible. The magnet is placed between the calorimeters and the muon

system. The solenoidal magnetic field parallel to the beam bends the tracks of the high momentum charged particles in the transverse plane. The curvature of the trajectory increases with the strength of the magnetic field which make possible to determine the transverse momentum more precisely. The magnet is complemented by a  $\sim 10000$  tonnes iron yoke which returns the magnetic field at 2 T.

### 3.3.6 Muon System

As the name suggests, the detection of muons is of central importance to CMS. Only the muons and neutrinos, out of all the known stable particles, pass through the calorimeter without depositing most or all of their energy. They interact very little with matter and can travel long distances through the dense matter. The charged muons can be detected by having an additional tracking system outside the calorimeters whereas the neutrinos are practically undetectable as they escape completely without being tracked in any of the layers. Their presence can be detected from the missing energy carried by them. The CMS muon system is installed outside calorimeters in the iron return yoke of the magnet. The muon system perform the muon identification, momentum measurement and triggering. Good muon momentum resolution and trigger capability are enabled by the high-field solenoidal magnet and its flux-return yoke. The latter also serves as a hadron absorber for the identification of muons. The CMS muon system is designed to have the capability of reconstructing the momentum and charge of muons over the entire kinematic range of the LHC. The muon system shown in Fig. 3.10 consists of three types of gaseous particle detectors :

**Drift Tube** - The muon barrel (MB) detector has four concentric layers of drift tube (DT) chambers inside the iron yoke which covers the region up to  $|\eta| < 1.2$ . DT stations are distributed into 5 wheels along the z direction. Each wheel is divided into 12 sectors, each covering a  $30^\circ$  azimuthal angle. The DTs are aluminium tubes

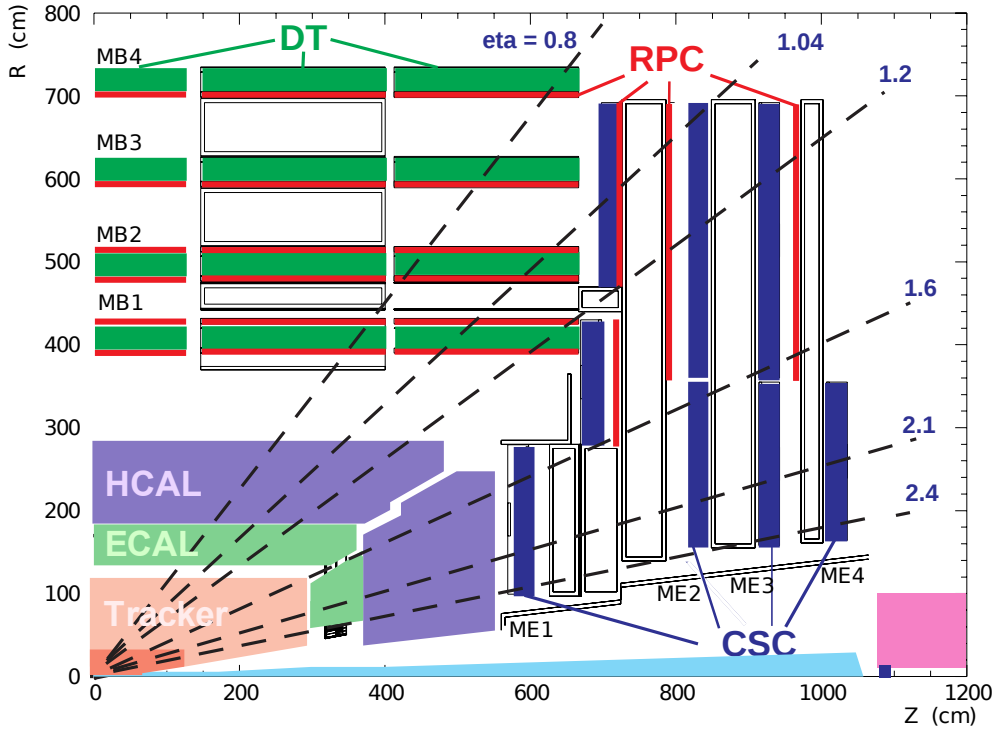


Figure 3.10: A longitudinal view presenting the location of the three muon subsystems : four Drift Tube (DT) stations in the barrel (MB1-MB4, green), four stations of Cathode Strip Chambers (CSC) in the endcap (ME1-ME4, blue), and the Resistive Plate Chambers (RPC) stations (red)<sup>8</sup>.

of 2.5 m of length and  $4.2 \times 1.3 \text{ cm}^2$  of area, filled with gas mixture ( 58% Ar + 15 % CO<sub>2</sub>).

**Cathode Strip Chambers** - In the forward region, the muon and background flux is higher. So cathode strip chambers (CSC) are preferred because of their fast response time, radiation tolerance and fine segmentation. The four stations of CSCs are installed in each end cap covering in total the region of  $0.9 < |\eta| < 2.4$ . Each CSC is trapezoidal in shape and consists of 6 gas gaps, each gap having a plane of radial cathode strips and a plane of anode wires running almost perpendicularly to the strips.

<sup>8</sup>Source : <https://arxiv.org/abs/1209.2646>

**Resistive Plate Chambers** - Both DT and CSC are accompanied by resistive plate chambers (RPC) which are double-gap chambers, operated in avalanche mode to ensure good operation at high rates. They help to resolve ambiguities in attempting to make tracks from multiple hits in a chamber and provide additional points for determination of a muon trajectory. They provide fast response to the trigger system which is described in the following section.

### 3.3.7 Trigger and Data Acquisition System

The proton-proton collisions (events) take place at high interaction rates at LHC. In the 2012 run period, at beam crossing frequencies of 25 ns there are 40 million bunch crossings per second with an average of around 20 collisions per bunch crossing. Both the collision and the overall data rates are much higher than the rate at which the information can be stored. So a dramatic rate reduction has to be achieved which is possible with an efficient trigger system by retaining interesting signal events and rejecting background events. The decision of accepting or rejecting an event has to be performed very quickly and it is based on signals of certain physics objects inside the detector. CMS has a two-level complex trigger system :

**Level-1 Trigger** - The Level-1 (L1) trigger system is based on custom electronics which stores the events at maximum rate of 100 kHz and then forward them to the next level triggers. The L1 system uses only coarsely segmented data from calorimeter and muon detectors, while holding all the high-resolution data in pipeline memories in the front-end electronics. Figure 3.11 shows the work flow of the L1 trigger system. L1 trigger consists of local, regional and global components. The local triggers known as Trigger Primitive Generators (TPG), are based on energy deposits in calorimeter trigger towers and tracks in muon chambers. Regional Triggers combine their information and use pattern logic to determine ranked and sorted trigger objects such as electron or muon candidates in limited spatial regions. The rank is determined as a function of energy or momentum and quality, which re-

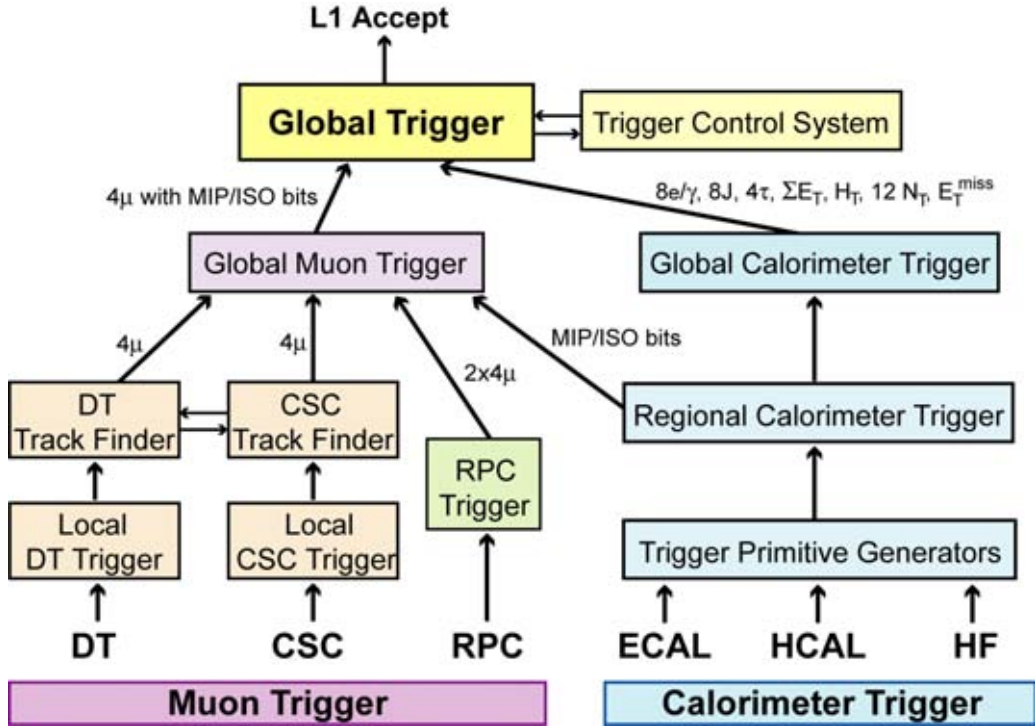


Figure 3.11: Work flow of the L1 trigger system. Taken from [23].

flects the level of confidence attributed to the L1 parameter measurements, based on detailed knowledge of the detectors and trigger electronics and on the amount of information available. The Global Calorimeter and Global Muon Triggers determine the highest-rank calorimeter and muon objects across the entire experiment and transfer them to the Global Trigger, the top entity of the Level-1 hierarchy. The latter takes the decision to reject an event or to accept it for further evaluation by the HLT.

**High Level Trigger -** At the second step, a software-based High-Level Trigger (HLT) is designed to reduce the maximum L1 accept rate of 100 kHz to a final output rate of 100 Hz. The HLT system filter events by performing physics selections using faster versions of the offline reconstruction software. The HLT is provided by a subset of the on-line processor farm which, in turn, passes a fraction of the accepted

events to the Data Acquisition (DAQ) system for more complete processing.

### 3.3.7.1 Jet Triggers

Triggers based on jet and missing transverse energy ( $E_T^{\text{miss}}$ ) triggers are important for search for new physics whereas the single-jet triggers are mainly designed to study quantum chromodynamics (QCD). In this thesis, the single-jet triggers are used to select the events for analysis. At L1, they use mainly information from the calorimeter by looking for an energy cluster and a high energy deposit. The sums of transverse energy from ECAL and HCAL are computed in  $4 \times 4$  trigger towers, except in the HF region where this quantity is measured in the whole trigger tower itself. If this deposit is greater than a certain threshold, the event is selected at L1 and it is passed to the HLT. Jets are reconstructed in the HLT using the anti- $k_t$  jet clustering algorithm. The inputs for the jet algorithm are either calorimeter towers giving “CaloJet” objects, or the reconstructed particle flow objects giving “PFJet” objects. The processing time of reconstruction algorithm is high and hence the jet trigger paths are divided into multiple selection steps. At first, jets are reconstructed from calorimeter towers. Only for events in which at least one calorimeter jet passes a certain  $p_T$  threshold, the particle flow algorithm is run and the jets are clustered again from the particle flow candidates. In 2012, most of the jet trigger paths use PFJets as their inputs. The rate of jet events is quite high, so PFJet trigger paths have a pre-selection based on CaloJets. The matching between CaloJets and PFJets is required in single PFJet paths. Due to the flexibility of the HLT, it is possible to apply the jet energy corrections during the HLT selection.

### 3.3.7.2 Data Acquisition System

As the L1 trigger accepts events at a rate of 100 kHz, the Data Acquisition (DAQ) system has to process the events at the same speed. It reads out the data of all detector sub-components and assembles the complete events, see Fig. 3.12. The data

is subsequently passed to the HLT which further reduces the rates to a few hundred events per second. Finally, the events are merged and saved to a local storage system, from which they are continuously transferred to the Tier-0 computing center at CERN.

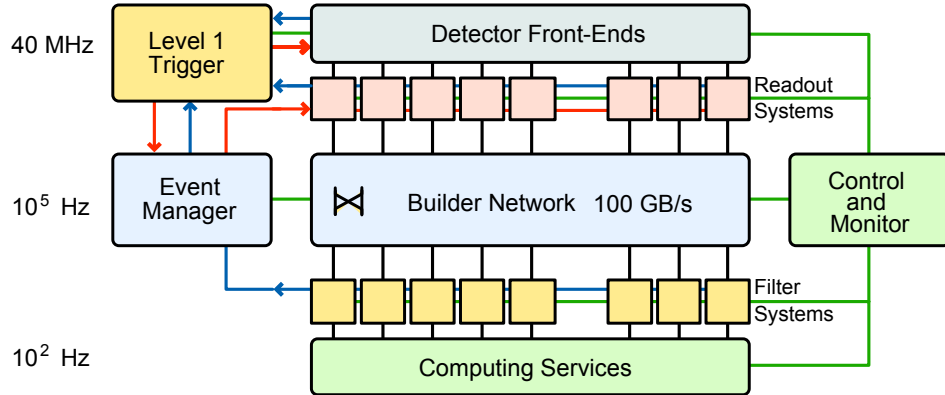


Figure 3.12: Architecture of the CMS DAQ system. Taken from [23].

### 3.3.8 Data Management

Although the trigger system reduces the collision rate enough to be stored in tape, still there is a huge amount of data need to be analyzed. An efficient computing infrastructure and the software is required for storing and distributing the data. To meet this need, the LHC has a data storage infrastructure called the Worldwide LHC Computing Grid (WLCG) [33]. WLCG provides a hierarchical structure, as shown in Fig. 3.13, in a series of four levels or Tiers. Each Tier is made up of several computer centres. All the raw collision data collected by CMS is converted into a format suitable for offline analysis and sorted in the form of datasets at the Tier-0 site at CERN. This processed data is then transferred to Tier-1 centers all over the world where reconstruction algorithms are run. Further reconstructed and simulated data is distributed to Tier-2 sites, where it is available for physics analysis mainly performed on Tier-3 sites.

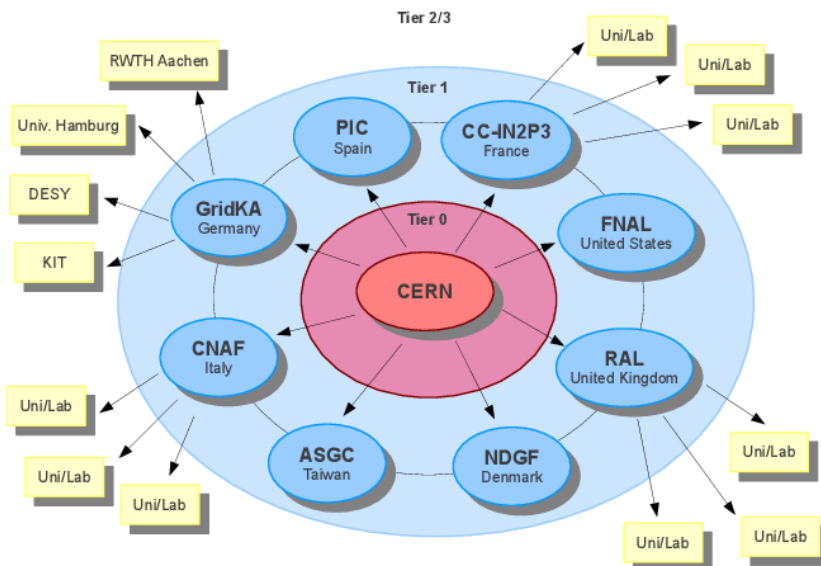


Figure 3.13: Schematic overview of the CMS computing grid. All data collected by CMS is stored at the Tier-0 site at CERN which is then transferred to Tier-1 centers all over the world. Further reconstructed and simulated data is distributed to Tier-2 sites, where it is available for physics analysis mainly performed on Tier-3 sites. Taken from [33].

# Chapter 4

## Event Generation, Simulation and Reconstruction

Event simulation plays a significant role in the operation of any experiment. Before the real data taking, reconstruction algorithms, efficiency of trigger paths, analysis strategies and other operational details of the experiment need to be studied and optimized well. This is achieved by simulation of the apparatus and the expected processes using the Monte Carlo (MC) method [34]. In high energy physics, the simulation of experimental data is done in two steps : event generation and detector simulation. Event generators simulate a collision starting from the proton-proton interaction up to the production of the final decay products, to be observed with the CMS detector. The output of an event generator is used as input for a detector simulation program which models the interactions of the generated final-state particles with the detector. This procedure requires a sophisticated and complex simulation of the detector material and of the behaviour of the particles in it.

### 4.1 Event Generation and Simulation Software

In real world, the machine or collider produces interactions which are observed by detectors. The interesting events are stored and reconstructed afterwards for a

physics analysis. In the Monte Carlo world, the role of machines is played by the event generators. The event generators generate simulated events as detailed as observed by a detector. The output of an event generator is in the form of “events” with the same behaviour and fluctuations as real data which serves as an input to the detector simulation, allowing a precise prediction and verification for the entire system of experimental setup. The comparison of real and Monte Carlo world is presented in Fig. 4.1.

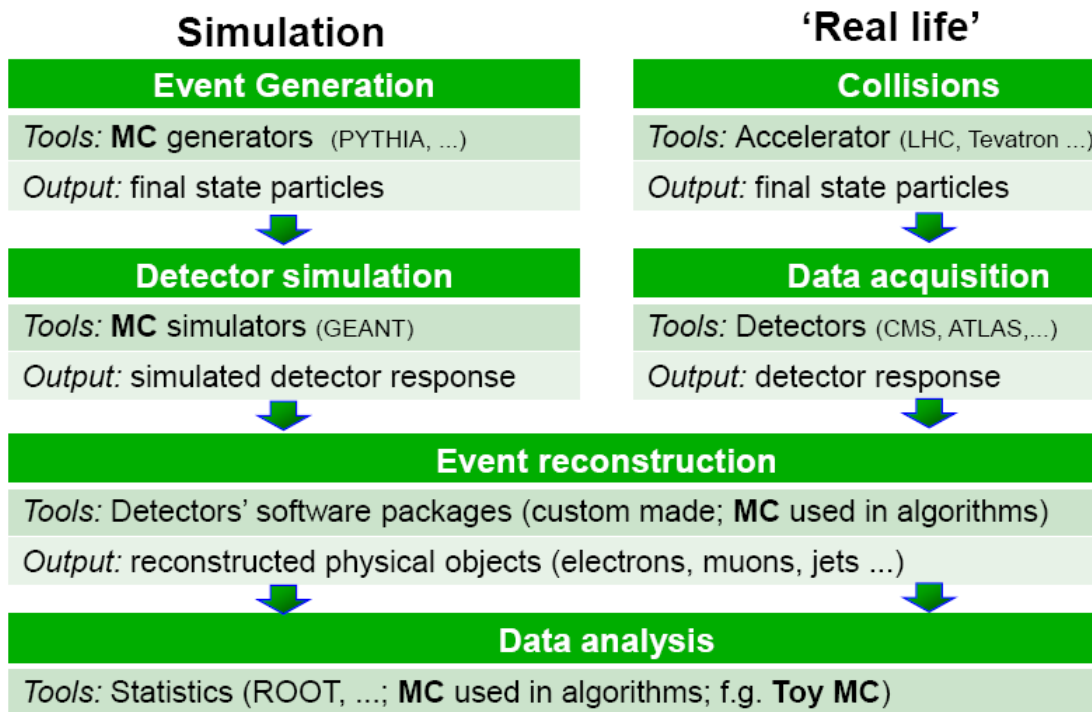


Figure 4.1: Comparison of Monte Carlo simulations with the real world data.

There are a variety of Monte Carlo event generators which are commonly used in high energy physics. The MC event generators used in this thesis include leading order (LO) generators : PYTHIA, MADGRAPH5 and HERWIG as well as the next-to-leading order generator POWHEG. These generators are described one by one in the following sections.

### 4.1.1 PYTHIA

PYTHIA is the most widely used program to generate the collisions at high energies for p-p, e-e and e-p colliders. It contains theory and models for a number of physics aspects, including hard and soft processes, parton distributions, initial-state and final-state parton showers, multiple interactions, fragmentation and decay. It also has a set of utilities and interfaces to external programs. It uses the Lund string hadronization model [35] to describe the hadronization process. PYTHIA was originally coded in FORTRAN language under the version 6 i.e. PYTHIA6 [36]. In 2004, it was rewritten in C++ and was released as PYTHIA8 [37] in 2007. The two versions differ in the description of multi-parton interactions. Both the versions use leading order (LO) calculations to derive the colored partons from the hard interaction. From these partons, colorless objects like hadrons, leptons and photons are produced. For the studies in this thesis, PYTHIA6 with tune Z2<sup>\*</sup> [38] and PYTHIA8 with tunes CUETS1 and CUETM1 [39] have been used.

### 4.1.2 MADGRAPH5

MADGRAPH5 [40] generates matrix elements for high energy physics processes, such as decays and  $2 \rightarrow n$  scatterings. The event information of the hard process such as particle ID, momenta, spin etc. is stored in the Les Houches format [41] and can be interfaced to other generators. In this thesis, MADGRAPH5 has been interfaced to PYTHIA6 with tune Z2<sup>\*</sup> to handle the rest of the generation steps which involves parton showering and hadronization. Matching algorithms make sure that there is no double-counting between the tree-level and the PS-model-generated partons. MADGRAPH5+PYTHIA6 (MG5+P6) samples are used mainly for general comparisons to data and calculating the detector resolution.

### 4.1.3 HERWIG

HERWIG (Hadron Emission Reactions With Interfering Gluons) [42] is a multi-purpose event generator. It includes the simulation of hard lepton-lepton, lepton-hadron and hadron-hadron scattering and soft hadron-hadron collisions. It uses angular ordering for parton showers and cluster model for hadronization. The HERWIG generator includes a number of hard scattering processes and has the possibility to interface external matrix element generators. It uses angular ordering for parton showers and cluster model for hadronization. HERWIG was FORTRAN based and has a version in C++, named HERWIG++ [43]. The samples generated using HERWIG++ generator with the default tune of version 2.3 [44] have been used to study non-perturbative effects.

### 4.1.4 POWHEG

POWHEG generator performs the fixed next-to-leading order (NLO) calculations merged with parton showers [45–47]. A computer framework known as POWHEG BOX [48], implements NLO calculations in shower Monte Carlo programs according to the POWHEG method. It can be interfaced with all modern shower Monte Carlo programs that support the Les Houches Interface for User Generated Processes. It contains the hard matrix elements for NLO dijet production. For the parton shower and hadronization, POWHEG is interfaced to PYTHIA8 with tunes CUETS1 and CUETM1.

### 4.1.5 NLOJET++ and FASTNLO

The LO as well as NLO cross-sections for jet production are evaluated using a C++ program called NLOJET++ [49, 50]. It uses the dipole subtraction method for the separation of the divergences. NLOJET++ can calculate up to three-jet observables at NLO precision. The perturbative QCD cross-section calculations in

NLOJET++ are determined in Monte Carlo integration and are very time consuming. So it is not feasible to repeatedly calculate the cross-sections which is required for PDF fits or uncertainty estimations. The NLOJET++ is interfaced to the FASTNLO project [51, 52] which performs fast re-evaluations of cross-sections. It stores the perturbative coefficients obtained with NLOJET++ in a way that the strong coupling constant and the PDFs can be changed afterwards without a recalculation of the perturbative coefficients.

All the event generators and cross-section calculation tools takes the PDFs as an input. They are either hard coded in the generators or accessed via a standardized interface with the LHAPDF library [53, 54]. LHAPDF provides a unified and easy way to use the PDF sets by storing them in data files. It provides interpolation routines to read the PDFs and interpolate the PDFs at all scales. It also allows access to single PDF members without needing to load whole sets. LHAPDF is supported by many MC event generators and other physics programs.

## 4.2 Detector Simulation

The particles generated by Monte Carlo event generators are passed through the detector simulation. It is a computer program which defines the detector system. The detector definition includes the representation of its geometrical elements, their materials and electronics properties. The geometrical representation of detector elements focuses on the definition of solid models and their spatial position. The detector simulation describes the interactions of the passing particles with the material of the detector. While propagating through the detector material, these particles are allowed to decay according to their known branching fractions and decay kinematics. The interactions of the particles with the detector material take place through several physical processes, including electron bremsstrahlung, energy loss by ionization, multiple scattering, hadron showering etc., which are simulated or parametrized in the corresponding parts of the detector.

In CMS, the detector response is simulated by two approaches [24] : Full Simulation and Fast Simulation. Full Simulation is based on a C++ simulation toolkit GEANT4 (GEometry ANd Tracking) [55]. It is a successor of a FORTRAN based GEANT3 and handles the interactions of particles with matter over a wide range of energy. In GEANT4, the magnetic fields, electric fields and electromagnetic uniform and non-uniform fields can be specified. The equation of motion of the particle in the field gives the track of the particle. A physical interaction of a track in the sensitive region of a detector is called a hit. The secondary particles produced are stored in a stack with the information of their kinematic properties as well as the vertex position where the interaction has occurred. A large number of Monte Carlo events may have to be produced for a feasible physics analysis. The complete detector simulation of CMS using GEANT4 is rather time consuming. For the fast simulation of the detector response, a Fast Simulation framework [56] has been developed in the general software framework of the CMS. In Fast Simulation, detector effects are parametrized instead of simulating these from first principles as done in Full Simulation. Fast Simulation package produces events at rates of the order of 100 times faster than the corresponding Full Simulation ones, while maintaining almost the same level of accuracy for physics studies. The format of the Fast Simulation data output is fully compatible with the standard Full Simulation one.

After simulating the detector response, it is then transformed into a digital signal with the help of electronics and this step is called digitization. The simulated output of the detector response needs to be as close as possible to the real data coming from the CMS detector. After this, event reconstruction algorithms are applied to both simulated and real events.

## 4.3 Event Reconstruction

The aim of the event reconstruction is to identify the particles passing through the detector by interpreting the electrical signals produced in digitization. These particles are produced either directly from the interaction point of pp collisions or from the hadronization process. In event reconstruction, analysis-level objects are created by combining recorded signals from the tracker, calorimeters and muon detectors. At initial level, the reconstructed hits are collected which are combined to form tracks and calorimetric towers. Then higher level objects such as electrons, photons, muons and jets are reconstructed by combining the tracks and energy deposits. This thesis presents the study of jets. The hadrons and other particles produced by the hadronization of a quark or gluon are clustered into a narrow cone called “jets”. The detailed description of jets is given in Sec. 2.4. The jet algorithms, discussed in Sec. 2.4.1, are used for clustering by taking partons, stable particles or reconstructed particle candidates as inputs. The different levels at which the jets are formed are parton level, particle level and detector or reconstructed level, as illustrated in Fig. 4.2. In the CMS detector, jets are the localized deposits of energy in the calorimeter cells along with the large number of tracks in the direction of the deposited energy. Depending on the type of input to the jet algorithm, jets can be categorized into different types :

**Generator Jets** - The stable particles generated by the Monte Carlo event generators are clustered into generator jets (GenJets). At this particle level, the passage through the detector simulation has not been carried out. The objects at this level are charged hadrons, photons and neutral hadrons. Since the energy of GenJets is independent of the detector response, these are considered as reference objects for jet energy corrections.

**Calorimetric Jets** - The jets reconstructed using the energy clusters deposited in the ECAL and HCAL calorimeter towers are called Calorimetric jets (CaloJets).

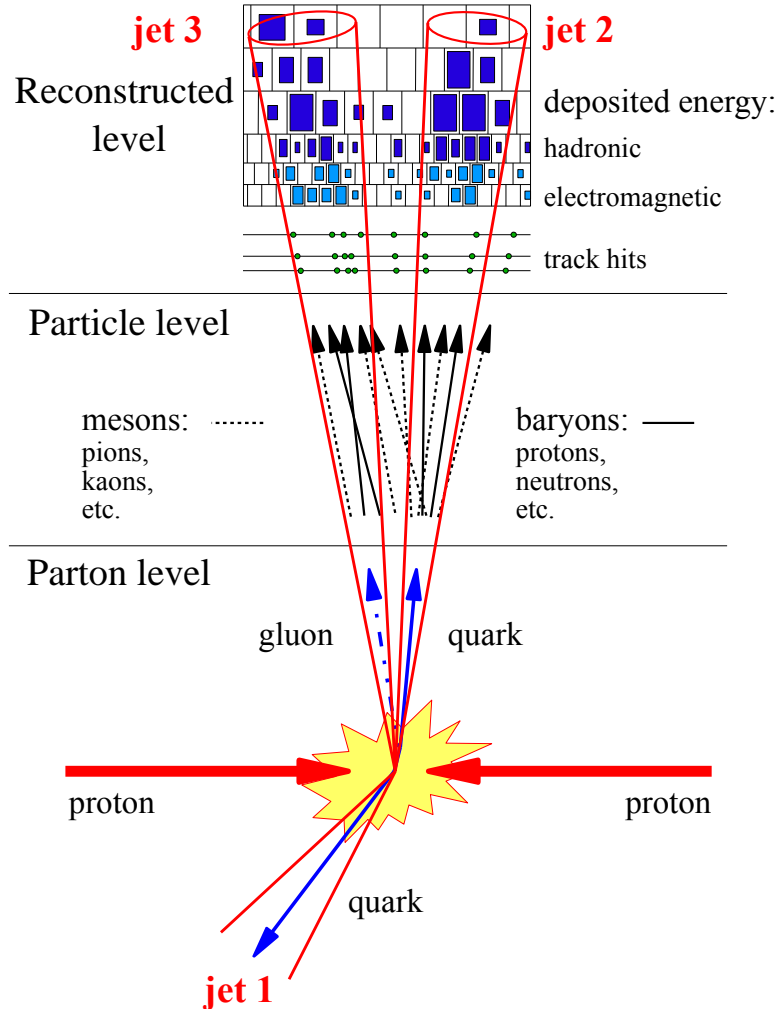


Figure 4.2: In a proton-proton collision, the hard scattered quarks and gluons fragment and hadronize to produce the showers of partons, hadrons, or detector measurements which are clustered into parton jets, particle jets and reconstructed jets, respectively. Taken from [57].

One calorimetric tower consists of one HCAL cell surrounded by an array of  $5 \times 5$  ECAL cells. The tower's four-momenta are computed taking the direction from the interaction point to the tower center and assuming zero mass. All towers with a transverse-energy measurement above 300 MeV are considered in the clustering process. CaloJets are relatively simple objects because only calorimeter information is deployed, but they are strongly affected by the non-linearity of the calorimeter response. Since the readout of calorimeter measurements is fast, CaloJets are com-

monly used by the trigger system.

**Particle Flow Jets** - The clustering of particle flow candidates give detector level jets called Particle Flow jets (PFJets). The four-momenta of the particles is taken as the input. The use of the tracking detectors and high granularity of the ECAL improves the energy resolution through the independent measurements of charged hadrons and photons inside a jet. Hence PFJets perform better than CaloJets and are the standard jets used at CMS.

The study presented in this thesis uses the jets clustered using the anti- $k_t$  algorithm with a jet size parameter of  $R = 0.7$  and particle flow candidates. In CMS, all the particles are reconstructed and identified using a Particle Flow (PF) algorithm, discussed in details in next section.

### 4.3.1 Particle Flow Algorithm

To identify and reconstruct the particles, the CMS employs the event reconstruction technique called Particle Flow (PF) algorithm [58,59]. Basically, the detector signals are concerted back to physical objects by using PF event reconstruction algorithm, as shown in Fig. 4.3. It combines the information from the individual sub-detectors. The additional identification of the tracks, using the Combinatorial Track Finder (CTF) algorithm [60], enhances the reconstruction performance. Based on these tracks, the primary vertices in an event are identified. The transverse momenta of final state stable particles or energies of the calorimeter towers are the inputs to PF algorithm. The PF algorithm first collects reconstructed hits in each sub-detector independently and creates a list of reconstructed elements (referred as blocks) : charged tracks in tracker, energy clusters in calorimeters and muon tracks in muon system. Then a link algorithm connects topologically compatible blocks producing PF objects. The PF objects consists of all stable particles : electrons, muons, photons, charged and neutral hadrons. The combination of the track momentum at

the main interaction vertex, the corresponding ECAL energy deposit and the energy sum of all bremsstrahlung photons associated with the track is used to determine the energy of electrons. The curvature of the tracks in tracker and muon chamber is used to estimate the energy of muons. The energy of photons is obtained directly from the ECAL measurement, corrected for zero-suppression effects<sup>9</sup>. The energy of charged hadrons is calculated by combining the track momentum and corresponding energy clusters in ECAL and HCAL, corrected for zero-suppression effects as well as calibrated for the nonlinear response of the calorimeters. The energy of neutral hadrons is obtained from the corresponding calibrated ECAL and HCAL energies only. Along with the reconstruction of these objects, missing transverse energy ( $E_T^{\text{miss}}$ ) is also determined using PF algorithm.  $E_T^{\text{miss}}$  is defined as the negative vector sum of transverse momenta  $p_T$  of all the isolated stable particles reconstructed in an event i.e.  $E_T^{\text{miss}} = -\sum_i \overrightarrow{p_{T,i}}$ . To avoid any kind of double-counting of energy, blocks of all PF reconstructed particle objects are removed and the energy of the calorimeter clusters is recalculated. Finally, the collection of PF objects is used to reconstruct the jets by using jet clustering algorithms.

### 4.3.2 Jet Energy Corrections

The measured energy of jets cannot be directly translated to the true particle or parton level. This is because of the nonlinear and nonuniform response of the calorimeters, effects of pileup and small residual effects in the data after corrections based on MC simulation. Hence to relate the measured jet energy to the corresponding true particle jet energy, jet energy corrections (JEC) [61, 62] are used to correct the measured jet energy. CMS follows a factorized approach, as presented in Fig. 4.4, where JEC are applied in a sequential manner with fixed order, i.e. the output of one step serves as the input for the next one. Each level of correction takes care

---

<sup>9</sup>To suppress noise in the calorimeters, only cells with energies above a given threshold are considered and this procedure is known as zero-suppression.

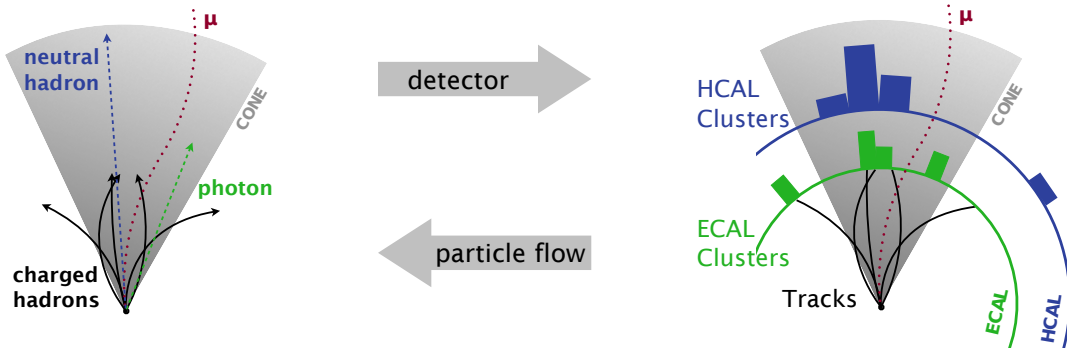


Figure 4.3: Schematic association of sub-detector measurements to physical particle objects using the Particle Flow (PF) event reconstruction technique used by CMS. [15]

of a different effect and is independent of each other. At each step, the jet four momentum is scaled with a correction factor which depends on jet  $p_T$ ,  $\eta$ , flavor etc.

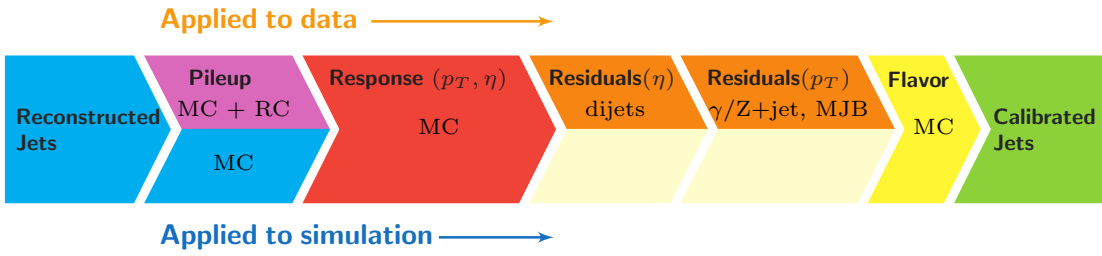


Figure 4.4: A schematic diagram of the factorized jet energy corrections (JEC) for data (upper half) and simulation (lower half) [62]. The reconstructed jets are corrected for pileup effects, non-uniform  $p_T$  and  $\eta$  response and residual differences between data and Monte Carlo simulations along with optional flavor corrections. All corrections marked with MC are derived from simulation studies, RC stands for random cone, and MJB refers to the analysis of multijet events.

The corrected jet transverse momentum  $p_T^{\text{corr}}$  is obtained by applying all correction factors subsequently on raw or uncorrected jet transverse momentum  $p_T^{\text{raw}}$  as below :

$$p_T^{\text{corr}} = c_{\text{res}}(\eta, p_T'') \cdot c_{\text{mc}}(\eta, p_T') \cdot c_{\text{pileup}}(\eta, \rho, A_j, p_T^{\text{raw}}) \cdot p_T^{\text{raw}} \quad (4.1)$$

where  $p'_T$  is the transverse momentum after applying the pileup correction factor  $c_{\text{pileup}}$  on  $p_T^{\text{raw}}$ ,  $p''_T$  is the transverse momentum after applying the additional correction factor  $c_{\text{mc}}$  because of relative and absolute effects derived from MC. At last a correction factor  $c_{\text{res}}$  for residual effects derived from data is applied. The corrections applied at each step are discussed as :

**Pileup Corrections -** The additional proton-proton collisions occurring within the same bunch-crossing produce particles which got clustered into the jets coming from the hard interaction. This extra energy must be subtracted from the reconstructed jet energy. This is done by applying the pileup corrections to raw jet  $p_T^{\text{raw}}$ . The pileup corrections are determined from the simulation of a sample of QCD dijet events processed with and without pileup effects. The pileup correction factor,  $c_{\text{pileup}}$  is calculated using jet area method from the pileup density  $\rho$  in the event and the jet area  $A_j$  and is parametrized as a function of  $\rho$ ,  $A_j$ , jet  $p_T$  and  $\eta$ . The corrections for residual differences between data and detector simulation as a function of eta are determined using the random cone (RC) method in zero-bias events. Hence the different pileup corrections are applied to data and MC.

**MC Corrections -** The next correction applied to the pile up corrected jets is based on simulated QCD events. There are some differences between the reconstructed and generated jet  $p_T$  because of inefficiencies introduced by the detector simulation. The correction factor,  $c_{\text{mc}}$  is derived by comparing the measured jet  $p_T$  to the particle level jet  $p_T$ . The corrections are determined as a function of jet  $p_T$  and  $\eta$  which make the detector response uniform over these two variables.

**Residual Data Corrections -** The jets corrected with above mentioned corrections are further corrected for remaining small differences between data and Monte Carlo simulations. This correction is only applied to data. The correction factor  $c_{\text{res}}$  is derived using data-driven methods. The relative residual corrections are based on well-balanced dijet events in which a forward probe jet is calibrated using a tag

jet in the well understood barrel region. The last correction step is the absolute residual correction in which reconstructed  $Z$  bosons balanced to a jet are used to calibrate the jet energy using the very precisely reconstructed  $Z$  boson.

**Flavor Corrections** - These corrections correct the jets for flavor dependence ( $b$ ,  $\tau$  etc.) and are optional. These are extracted using  $Z+jet$  and photon+jets simulated events. The flavor corrections have not been applied for 8 TeV data.

The process of correction of jets by using JEC introduces uncertainties in the final corrected jet energy which are discussed in Sec. 5.6.2.

## 4.4 Software Tools

Every year, the CMS is recording a huge amount of data, from collisions as well as simulations. This data is analyzed iteratively to improve the understanding of the detector and the measured physics. So a dedicated data structure and software tools are required for data analysis. These are included in the software framework referred to as CMSSW. This section describes the CMSSW framework and software tools used in the current study.

### 4.4.1 CMSSW Framework

The CMS software framework (CMSSW) [63] provides all necessary tools for a physics analysis. The CMSSW framework is built on top of an event data model (EDM). It is a container for arbitrary C++ objects, e.g. recorded raw data and reconstructed physical objects (e.g particles, missing transverse energy) or derived quantities of an event. The reconstruction and distribution algorithms in CMSSW are divided into modules, which can be dynamically loaded and run. The CMSSW event processing model consists of one executable, called cmsRun, and many plug-in modules which are managed by the framework. SCRAM (Source Configuration, Re-

lease, And Management) is a configuration and management tool in the framework. It builds a runtime environment and make available all the necessary shared libraries. The shared libraries reduces memory consumption by only loading required modules during runtime. The CMSSW framework performs calibration, event generation, detector simulation, event reconstruction as well as data analysis by implementing the codes either in C++ or Python languages. To reduce the event content, a process called skimming is performed where only necessary data is preserved.

#### **4.4.2 ROOT**

ROOT [64] is an object-oriented data analysis framework, developed by CERN. ROOT consists of a huge C++ library provided with all the functionalities to store and analyze large amounts of data. It provides histogramming methods in 1, 2 and 3 dimensions, curve fitting, function evaluation, minimization, graphics and visualization classes. The command language of ROOT is command line interpreter (CINT), with several extensions to C++ which makes ROOT a versatile package. ROOT is an open-source system which can be dynamically extended by linking external libraries. The events generated or analyzed in CMSSW framework are stored in a tree structure in files using ROOT libraries. In this thesis, ROOT has been used extensively for storing information of events or objects, for fitting as well as plotting purposes.

# Chapter 5

## Measurement of the Differential Inclusive Multijet Cross-sections and their Ratio

The inclusive differential jet event cross-sections are studied as a function of the average transverse momentum,  $H_{T,2}/2 = \frac{1}{2}(p_{T,1} + p_{T,2})$ , where  $p_{T,1}$  and  $p_{T,2}$  denote the transverse momenta of the two leading jets, and are defined by :

$$\frac{d\sigma}{d(H_{T,2}/2)} = \frac{1}{\epsilon \mathcal{L}_{\text{int,eff}}} \frac{N_{\text{event}}}{\Delta(H_{T,2}/2)} \quad (5.1)$$

where  $N_{\text{event}}$  is the number of inclusive n-jet events counted in an  $H_{T,2}/2$  bin,  $\epsilon$  is the product of the trigger and jet selection efficiencies, which are greater than 99%,  $\mathcal{L}_{\text{int,eff}}$  is the effective integrated luminosity, and  $\Delta(H_{T,2}/2)$  are the bin widths. The measurements are reported in units of (pb/GeV). The inclusive n-jet event samples include the events with number of jets  $\geq n$ , where  $n = 2$  and  $3$  in the current study.

The cross-section ratio  $R_{32}$ , defined in Eq. 5.2 is obtained by dividing the differential cross-sections of inclusive 3-jet events to that of inclusive 2-jet one, for

each bin in  $H_{\mathrm{T},2}/2$ .

$$R_{32} = \frac{\frac{d\sigma_{3-jet}}{d(H_{\mathrm{T},2}/2)}}{\frac{d\sigma_{2-jet}}{d(H_{\mathrm{T},2}/2)}} \quad (5.2)$$

For inclusive 2-jet events ( $n_j \geq 2$ ) sufficient data are available up to  $H_{\mathrm{T},2}/2 = 2000$  GeV, while for inclusive 3-jet events ( $n_j \geq 3$ ) and the ratio  $R_{32}$ , the accessible range in  $H_{\mathrm{T},2}/2$  is limited to  $H_{\mathrm{T},2}/2 = 1680$  GeV.

## 5.1 Data Samples

This measurement uses the data which was collected at the centre-of-mass energy of 8 TeV by CMS experiment in the 2012 run period of the LHC. The 2012 data is taken in four periods A, B, C, D and the data sets are divided into samples according to the run period. Further each sample is grouped into subsets based on the trigger decision. For run B-D, the `JetMon` stream datasets contain prescaled low trigger threshold paths (HLTPFJet40, 80, 140, 200 and 260) while the `JetHT` stream datasets contain unprescaled high threshold trigger paths (HLT PFJet320 and 400). For run A, the `Jet` stream contains all the above mentioned trigger paths. The data to be used in physics analysis must satisfy a certain criteria according to which it should fulfill the validation requirements of data quality monitoring procedure. CMS uses JSON (Java Script Object Notation) format files to store the range of good lumi sections within a run. In the current analysis, the applied certification file<sup>10</sup> is based on the final event reconstruction of the 2012 CMS data sets. The datasets used in the current study are mentioned in the Table 5.1 along with the luminosity of each dataset which increases with period. Full 2012 data sample corresponds to an integrated luminosity of  $19.71 \text{ fb}^{-1}$ .

---

<sup>10</sup>Cert\_190456-208686\_8TeV\_22Jan2013ReReco\_Collisions12\_JSON

Table 5.1: Run range and luminosity of the proton-proton collisions data collected at the centre-of-mass energy of 8 TeV by CMS experiment in the year of 2012 in four different run periods A, B, C and D.

Run	Run range	Data set	Luminosity $\text{fb}^{-1}$
A	190456-193621	/Jet/Run2012A-22Jan2013-v1/AOD	0.88
B	193834-196531	/Jet[Mon,HT]/Run2012B-22Jan2013-v1/AOD	4.41
C	198022-203742	/Jet[Mon,HT]/Run2012C-22Jan2013-v1/AOD	7.06
D	203777-208686	/Jet[Mon,HT]/Run2012D-22Jan2013-v1/AOD	7.37

### 5.1.1 Monte Carlo Samples

To have a comparison of data results with the simulated events, the **MADGRAPH5** Monte-Carlo (MC) event generator has been used. It has been interfaced to **PYTHIA6** by the LHE event record, to generate the rest of the higher-order effects using the Parton Showering (PS) model, with tune Z2\* to model the underlying event. The MC samples are processed through the complete CMS detector simulation to allow studies of the detector response and compare to measured data on detector level.

The cross-section measured as a function of the transverse momentum  $p_T$  or the scalar sum of the transverse momentum of all jets  $H_T$  falls steeply with the increasing  $p_T$ . So in the reasonable time, it is not possible to generate a large number of high  $p_T$  events. Hence, the events are generated in the different phase-space region binned in  $H_T$  or the leading jet  $p_T$ . Later on, the different phase-space regions are added together in the data analyses by taking into account the cross-section of the different phase-space regions. The official CMS **MADGRAPH5+PYTHIA6** (MG5+P6) MC samples used in this analysis are generated as slices in the  $H_T$  phase-space are tabulated in Table 5.2 along with their cross-sections and number of events generated.

Table 5.2: The official Monte Carlo samples are produced in phase space slices in  $H_T$  with the generator MADGRAPH5 and interfaced to PYTHIA6 for the parton shower and motorization of the events. The cross-section and number of events generated are mentioned for each sample.

Generator	Sample	Events	Cross-section pb
MADGRAPH5 + PYTHIA6	/QCD_HT-100To250_TuneZ2star_8TeV-madgraph-pythia6/ Summer12_DR53X-PU_S10_START53_V7A-v1/AODSIM	50129518	$1.036 \times 10^7$
	/QCD_HT-250To500_TuneZ2star_8TeV-madgraph-pythia6/ Summer12_DR53X-PU_S10_START53_V7A-v1/AODSIM	27062078	$2.760 \times 10^5$
	/QCD_HT-500To1000_TuneZ2star_8TeV-madgraph-pythia6/ Summer12_DR53X-PU_S10_START53_V7A-v1/AODSIM	30599292	$8.426 \times 10^3$
/QCD_HT-1000ToInf_TuneZ2star_8TeV-madgraph-pythia6/ Summer12_DR53X-PU_S10_START53_V7A-v1/AODSIM		13843863	$2.040 \times 10^2$

## 5.2 Event Selection

The events are selected according to several quality criteria which ensures the high purity and high selection efficiency of the sample to be studied. This event selection also reduces beam induced background, detector-level noise and jets arising from fake calorimeter energy deposits.

### 5.2.1 Trigger Selection

CMS implements a two-level trigger system to reduce the amount of recorded events to a sustainable rate. In this analysis the jets are the final objects to study. So single jet trigger paths with varying thresholds are used to select events in data. It consists of one L1 trigger seed and multiple HLT filters. The L1 jet trigger uses transverse energy sums computed using both HCAL and ECAL in the central region ( $|\eta| < 3.0$ ) or HF in the forward region ( $|\eta| > 3.0$ ). The single jet triggers (HLT\_PFJetX), same as the ones used for other CMS 8 TeV measurements [65, 66], are used in the current study and are tabulated in Table 5.3. A single jet trigger selects an event in which at least one jet has the transverse momentum above the threshold. HLT\_PFJetX implies that there is at-least one jet in the event, whose  $p_T > X$  (GeV). The L1 trigger has a lower threshold to ensure full efficiency versus  $p_T$  of the HLT trigger. The  $p_T$  spectrum is steeply falling and hence the rates for low- $p_T$  jets are very high.

So it is not feasible to use a single unprescaled trigger for the selection of all required events. To collect sufficient data in the lower part of the  $p_T$  spectrum, different five prescaled low- $p_T$  trigger paths, each with different prescale value, are used. Also, one unprescaled trigger i.e. HLT\_Jet320 is used in the high  $p_T$  region, in which the rate is sufficiently small to collect and store all events. During the reconstruction of the spectrum, the prescales have been taken into the account.

Table 5.3: The single jet trigger paths used in the analysis are listed here. The column  $H_{T,2}/2, 99\%$  indicates the value of  $H_{T,2}/2$  at which each trigger exhibits an efficiency larger than 99%. The last column gives the effective luminosity seen by each trigger which divided by the total integrated luminosity of  $19.71 \text{ fb}^{-1}$ , gives the effective prescale applied on a trigger over the whole run period.

Trigger Path	L1 threshold GeV	HLT threshold GeV	$H_{T,2}/2, 99\%$ GeV	Eff. Lumi $\text{fb}^{-1}$
HLT_PFJet80	36	80	120.0	0.0021
HLT_PFJet140	68	140	187.5	0.056
HLT_PFJet200	92	200	262.5	0.26
HLT_PFJet260	128	260	345.0	1.06
HLT_PFJet320	128	320	405.0	19.71

The efficiency of each trigger path as a function of  $H_{T,2}/2$  is described by the turn-on curves with a rising part where the trigger is partly inefficient, until a plateau region where the trigger is fully efficient. Hence it is important to determine the threshold above which a trigger becomes fully efficient. The threshold is the value at which the trigger efficiency exceeds 99%. The trigger efficiency for HLT\_PFJetY is given by Eq. 5.3 where HLT\_PFJetX is the reference trigger and is assumed to be fully efficient in the considered phase space region. The value of X is chosen previous to that of Y in  $p_T$  ordering from the trigger list so that the higher trigger condition can be emulated from the lower trigger path.

$$\epsilon_{\text{HLT\_PFJetY}} = \frac{H_{T,2}/2 \left( \text{HLT\_PFJetX} + (\text{L1Object\_p}_T > \text{Z}) + (\text{HLTOBJECT\_p}_T > \text{Y}) \right)}{H_{T,2}/2(\text{HLT\_PFJetX})} \quad (5.3)$$

where Y is the  $p_T$  threshold of HLT\_PFJetY and Z is the L1 seed value corresponding to the trigger path HLT\_PFJetY. The denominator represents the number of events for which the reference trigger path HLT\_PFJetX has been fired. The numerator is the number of events for which HLT\_PFJetX has been fired along the  $p_T$  of  $\text{L1Object} \geq Z$  and the  $p_T$  of  $\text{HLTObject} \geq Y$ . For example, to obtain turn-on curve for HLT\_PFJet260, HLT\_PFJet200 is the reference HLT path. The  $p_T$  cut on L1Object is 128 GeV and  $p_T$  cut on HLTObject is 260 GeV. The threshold point at which the trigger efficiency is larger than 99% is determined by fitting the turn-on distribution with a sigmoid function described in Eq. 5.4. The trigger turn-on curves as a function of  $H_{T,2}/2$  can be seen in Fig. 5.1 which are described by a sigmoid function (blue line). The error bars give the uncertainty on the efficiency which is calculated using Clopper-Pearson confidence intervals [67].

$$f_{fit}(x) = \frac{1}{2} \left( 1 + \operatorname{erf} \left( \frac{x - \mu}{\sqrt{2}\sigma} \right) \right) \quad (5.4)$$

### 5.2.2 Primary Vertex Selection

The reconstructed tracks, number of strip and pixel hits and the normalized track  $\chi^2$ , identify the primary vertex (PV). The tracks are clustered according to the z-coordinate of their point of closest approach to the beam axis. A selection criteria for primary vertex should be followed which helps to identify and reject the beam background events. At-least one good primary vertex reconstructed from at least four tracks within a distance of  $|z(PV)| < 24$  cm to the nominal interaction point in a collision, is required in each event. The radial distance in x-y plane,  $\rho(PV)$  should be not be greater than 2 cm. The number of degrees of freedom in fitting for the position of each vertex using its associated tracks should be at-least four in number.

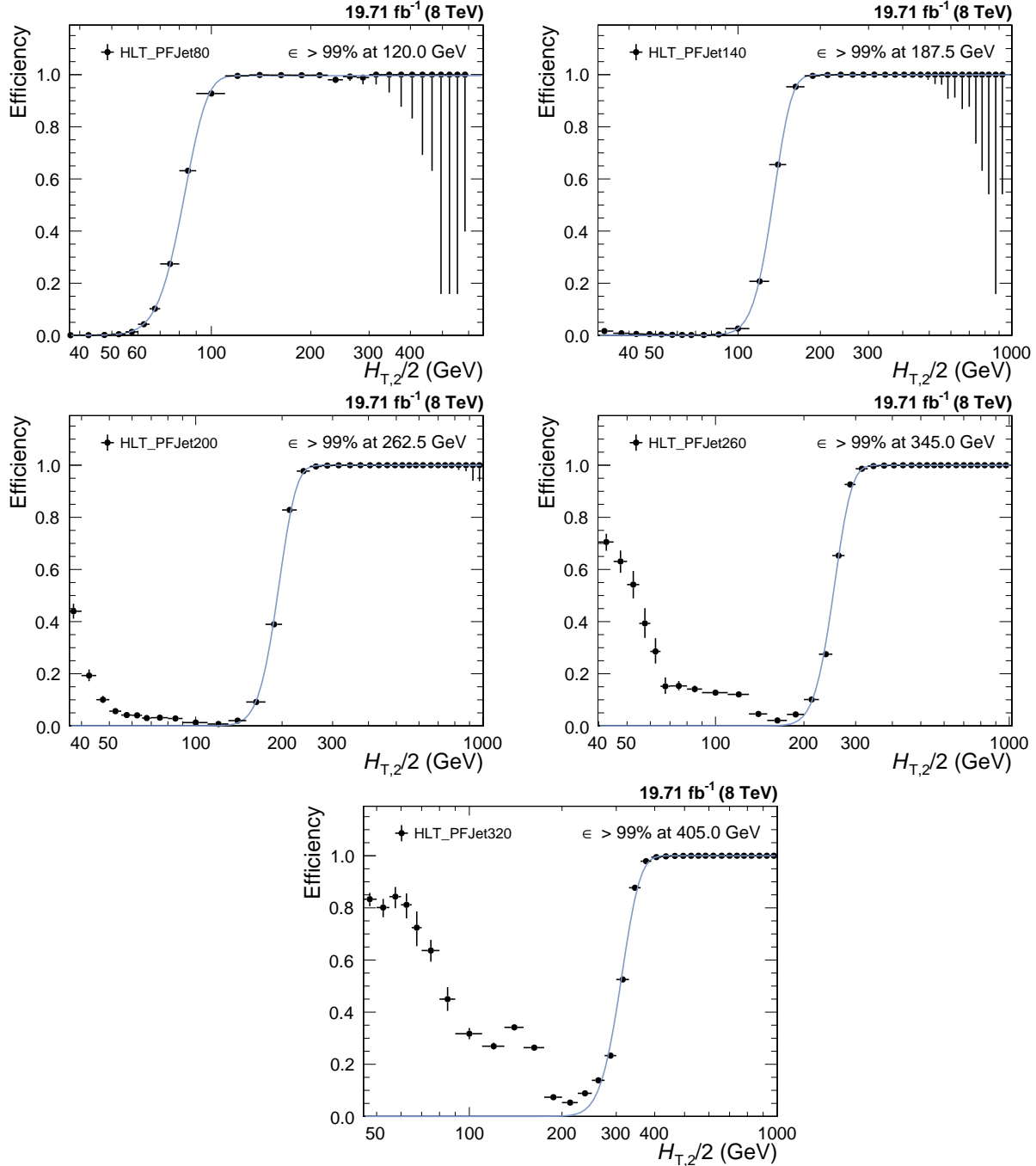


Figure 5.1: Trigger efficiencies turn-on curves for the single jet trigger paths are fitted with a sigmoid function (blue line) to obtain the 99% efficiency threshold. The error bars give the uncertainty on the efficiency which is calculated using Clopper-Pearson confidence intervals [67].

### 5.2.3 Missing Transverse Energy

In an ideal detector where all particles could be identified and perfectly measured, the transverse momentum of all particles would sum up to zero. But the neutral weakly interacting particles, such as neutrinos, escape from typical collider detectors and do not produce any direct response in the detector elements. The imbalance of total momentum of all visible particles can give the hints of the presence of such particles. The vector momentum imbalance in the plane perpendicular to the beam direction is known as missing transverse momentum or energy ( $E_T^{\text{miss}}$ ). It is one of the most important observables for discriminating leptonic decays of W bosons and top quarks from background events which do not contain neutrinos, such as multijet and Drell–Yan events or searches for physics beyond the Standard Model.

The ratio of missing transverse energy to the total transverse energy  $E_T^{\text{miss}}/\sum E_T$ , shown in Fig. 5.2 for  $n_j \geq 2$  (left) and  $n_j \geq 3$  events (right), shows a discrepancy between data (black solid circles) and simulated MC (blue histogram), at the tail part of the distribution. This is because of a finite contribution from  $Z(\rightarrow \nu\bar{\nu}) + \text{jet}$  events which gives rise to non-zero  $E_T$  in the events in data. Such events are absent in QCD simulated events in MC. Hence  $E_T^{\text{miss}}/\sum E_T$  is required to be less than 0.3 to reject events with high  $E_T^{\text{miss}}$ .

### 5.2.4 Jet Identification

In order to suppress fake jets, arising from detector noise or misreconstructed particles, jet identification criteria (ID) has been applied. Instead of applying it event-wise, it is applied it on each jet. The algorithm works on reconstructed jets using information of the clustered particle candidates. The official tight jet ID [68], recommended by JETMET group [69] is used. Due to pileup and electronic noise the jet constituent fractions may vary from event to event. In order to reject the noisy jets, some jet selection criteria are optimized to select only good quality jets. The selec-

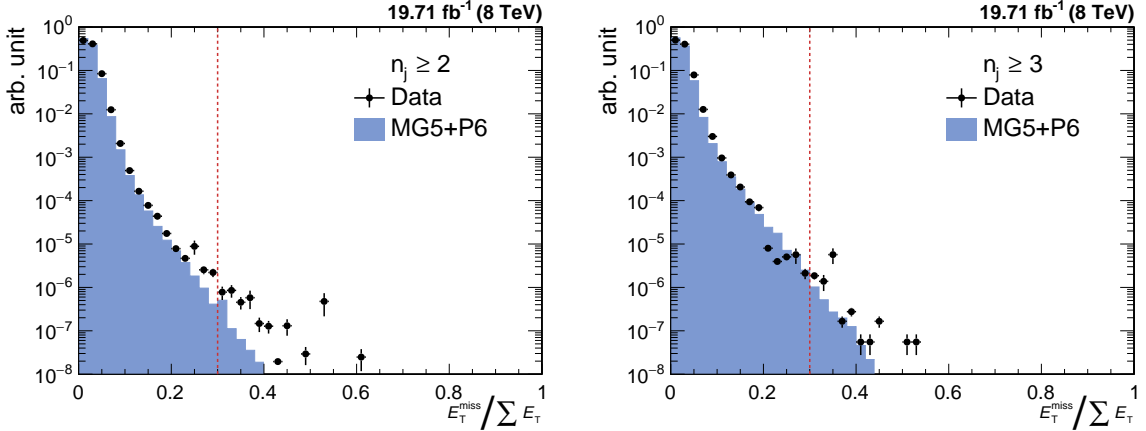


Figure 5.2: Missing transverse energy fraction of the total transverse energy per event in data (black solid circles) and simulated Monte Carlo events (blue histogram) in inclusive 2-jet (left) and 3-jet events (right). To remove background and noise, events with a fraction exceeding a certain threshold, here indicated with the red dashed line, are rejected.

tion criteria are implemented as selection cut on jet fractions. Table 5.4 summarizes the properties of the reconstructed jets and their respective cuts. Each jet should contain at least two particles, one of which should be a charged hadron. The cut on the fraction of neutral hadrons and photons removes HCAL noise and ECAL noise, respectively. Muons that are falsely identified and clustered as jets are removed by the muon fraction criterion. Based on information of the tracker, additional selection cuts are enforced in the region  $|\eta| < 2.4$ . The charged electromagnetic fraction cut removes the jets clustered from misidentified electrons. Furthermore, the fraction of charged hadrons in the jet must be larger than zero and jets without any charged hadrons are very likely to be pileup jets. The Figs. 5.3 and 5.4 show the distributions of the jet constituents observed in data (black solid circles) and simulated MC events (blue histogram) for  $n_j \geq 2$  and  $n_j \geq 3$ , respectively.

#### 5.2.4.1 Jet ID Efficiency

The efficiency of the jet ID as a function of  $H_{T,2}/2$  is studied using a tag-and-probe technique with dijet events. The two leading jets are required to be back-to-back in the azimuthal plane such that  $|\Delta\phi - \pi| < 0.3$ . One of the dijets is selected randomly

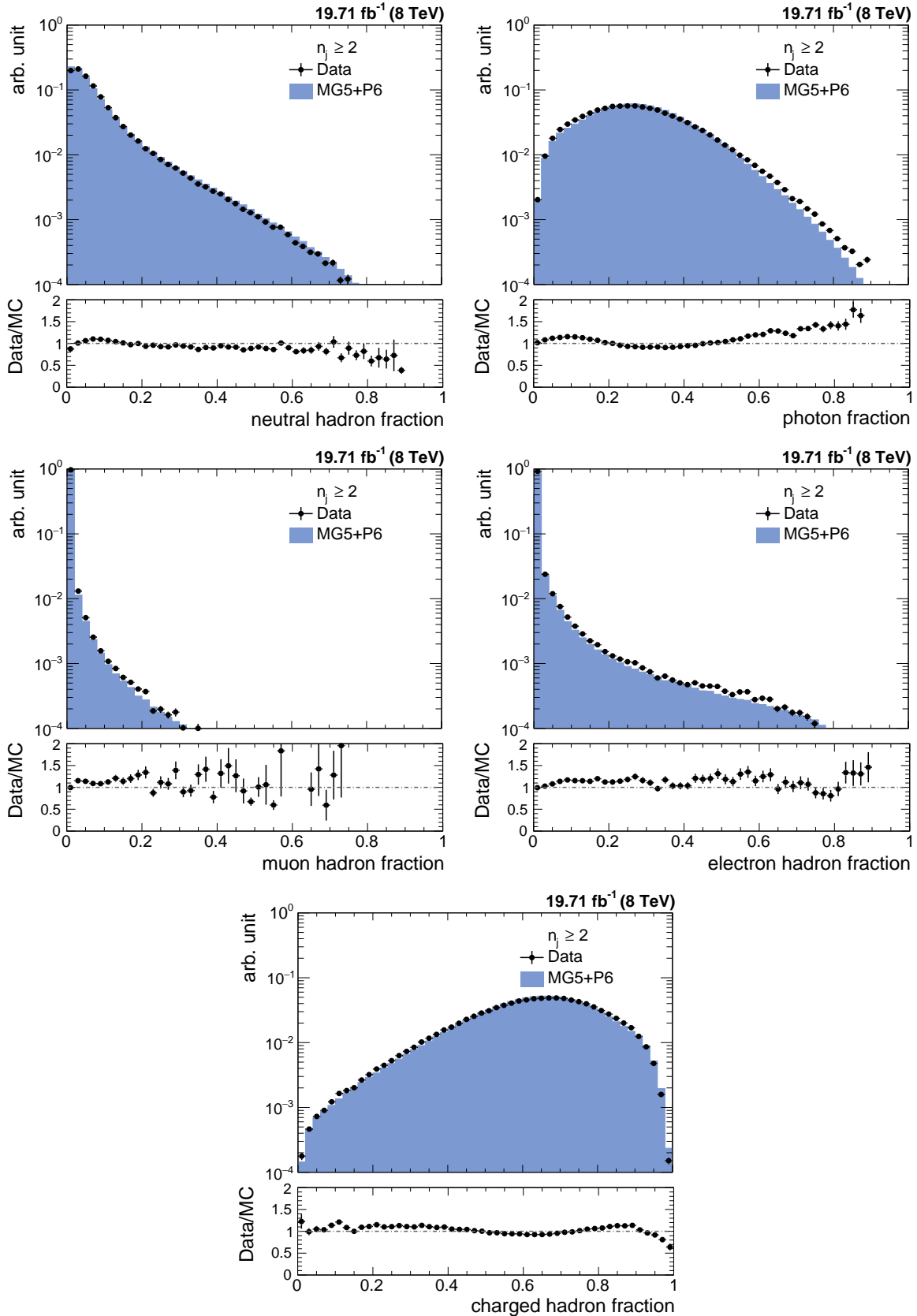


Figure 5.3: The fractions of jet constituents as observed in data (black solid circles) and simulated Monte Carlo events (blue histogram) for different types of PF candidates for inclusive 2-jet events. Data and simulations are normalized to the same number of events. The distributions are shown after the application of the jet ID.

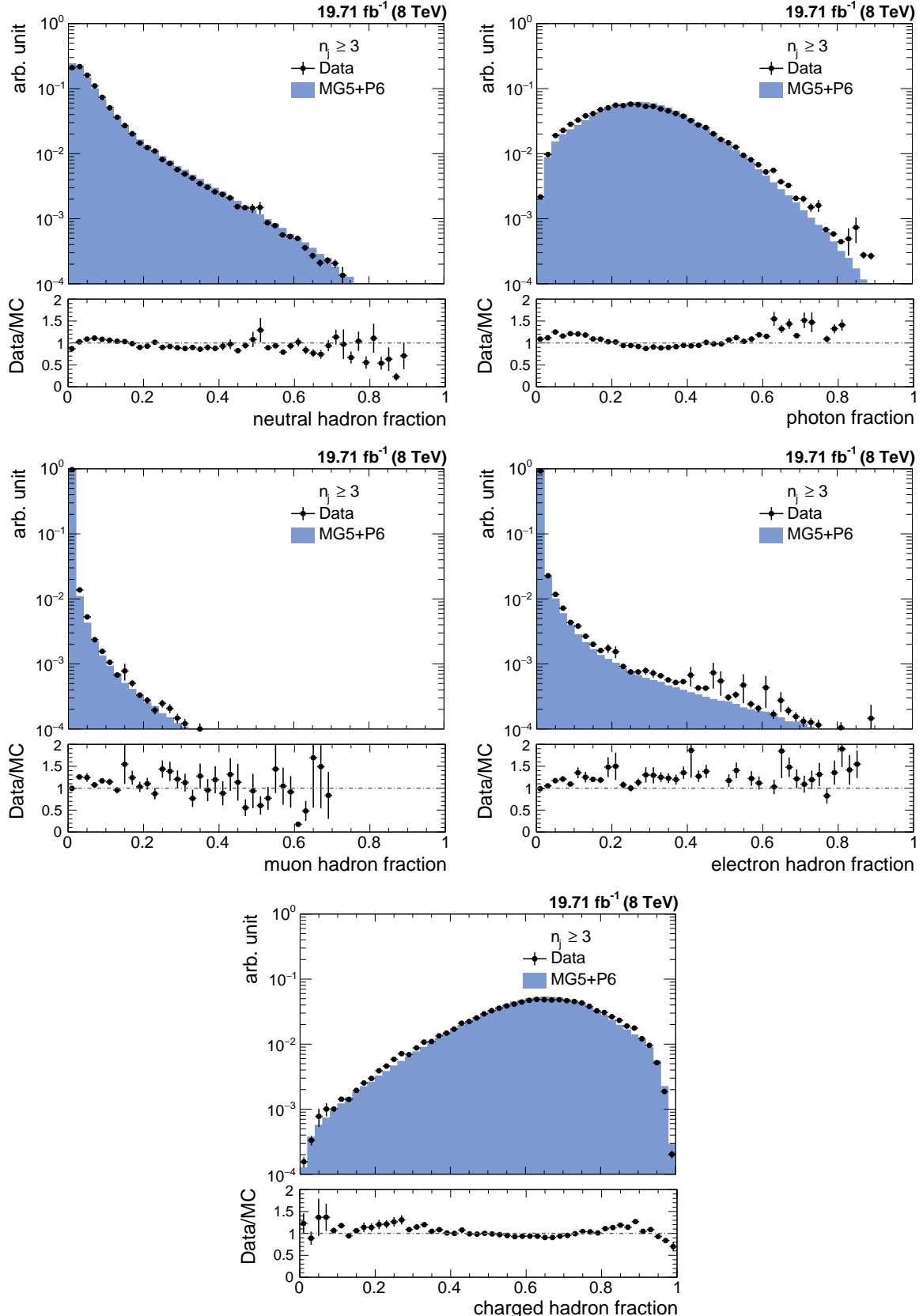


Figure 5.4: The fractions of jet constituents as observed in data (black solid circles) and simulated Monte Carlo events (blue histogram) for different types of PF candidates for inclusive 3-jet events. Data and simulations are normalized to the same number of events. The distributions are shown after the application of the jet ID.

Table 5.4: The jet ID removes noise and fake jets based on the properties of the reconstructed jets and the clustered particle candidates. All the selection cuts which are recommended by the JETMET group are applied [69].

	Property	Loose ID	Tight ID
Whole $\eta$ region	neutral hadron fraction	< 0.99	< 0.90
	neutral EM fraction	< 0.99	< 0.90
	number of constituents	> 1	> 1
	muon fraction	< 0.80	< 0.80
only $ \eta  < 2.4$	charged hadron fraction	> 0	> 0
	charged multiplicity	> 0	> 0
	charged EM fraction	< 0.99	< 0.90

as a “tag” jet which is required to fulfill the tight jet ID criteria. The other jet is called “probe” jet for which it is examined, whether it also passes the tight jet ID. The ID efficiency is defined as the ratio of events where the probe jet passes the ID requirements, over the total number of dijet events. It is shown as function of  $H_{T,2}/2$  in Fig. 5.5 and as expected, it is always greater than 99%. The QCD cross-section decreases as a function of  $H_{T,2}/2$  and hence the number of events decrease on moving to higher  $H_{T,2}/2$ . Consequently the statistical fluctuations for ID efficiency are larger at higher  $H_{T,2}/2$ .

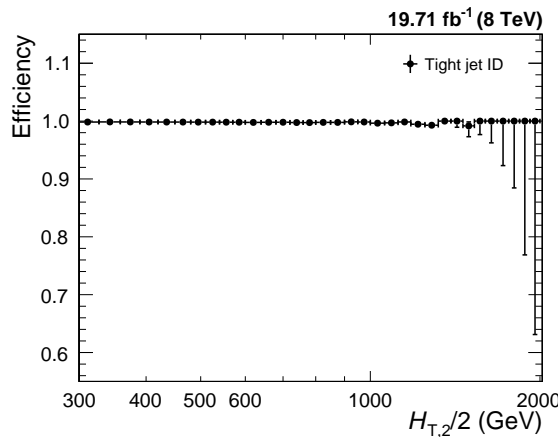


Figure 5.5: The jet ID efficiency is studied as a function of  $H_{T,2}/2$  with tag-and-probe technique using dijet event topologies and it always exceeds 99%.

### 5.2.5 Jet Selection

The measurement of differential cross-sections and their ratio uses jets clustered from particle flow candidates using the anti- $k_t$  jet algorithm with a size parameter,  $R = 0.7$ . The energy scale of the jets is corrected with the CMS recommended jet energy corrections, described in Sec. 4.3.2. These corrections are applied to jets in both data<sup>11</sup> as well those in simulated events<sup>12</sup>. As a convention, the jets in one event are in decreasing order of  $p_T$ , with the first (leading) jet being the jet with highest  $p_T$ . The jet selection, based on phase space cuts on transverse momentum and rapidity of jets in an event, is as follows :

- All jets having  $p_T > 150$  GeV and  $|y| < 5.0$  are selected.
- Events with at least two jets are selected.
- The two leading jets should have  $|y| < 2.5$  and further jets are counted only, if they lie within the same central rapidity range of  $|y| < 2.5$ .

These cuts assure high detector acceptance and exactly same selection is applied in the measurement, simulated events as well in theoretical calculations for a consistent comparison.

## 5.3 Comparison with Simulation

### 5.3.1 Pileup Reweighting

While generating the official Monte-Carlo samples, the number of pileup interactions describing the conditions expected for each data-taking period are taken care of. But the number of pileup events implemented in the simulation  $N_{\text{MC}}(N_{\text{PU,truth}})$ , does not

---

<sup>11</sup>Winter14\_V8 jet energy corrections

<sup>12</sup>START53\_V27 jet energy corrections

match exactly with the one measured actually in data  $N_{\text{data}}(N_{\text{PU,est.}})$ . To match the pileup distributions in data, a reweighting factor  $w_{\text{PU}}$ , as given by Eq. 5.5 is applied to the simulated events. In Fig. 5.6 the number of reconstructed vertices are shown before (left) and after pileup reweighting (right). It is observed that before pileup reweighting there was a significant mismatch of the pileup distributions in data (black solid circles) and simulated MC events (blue histogram), which completely vanishes after reweighting.

$$w_{\text{PU}} = \frac{N_{\text{data}}(N_{\text{PU,est.}}) / \sum N_{\text{data}}}{N_{\text{MC}}(N_{\text{PU,truth}}) / \sum N_{\text{MC}}} \quad (5.5)$$

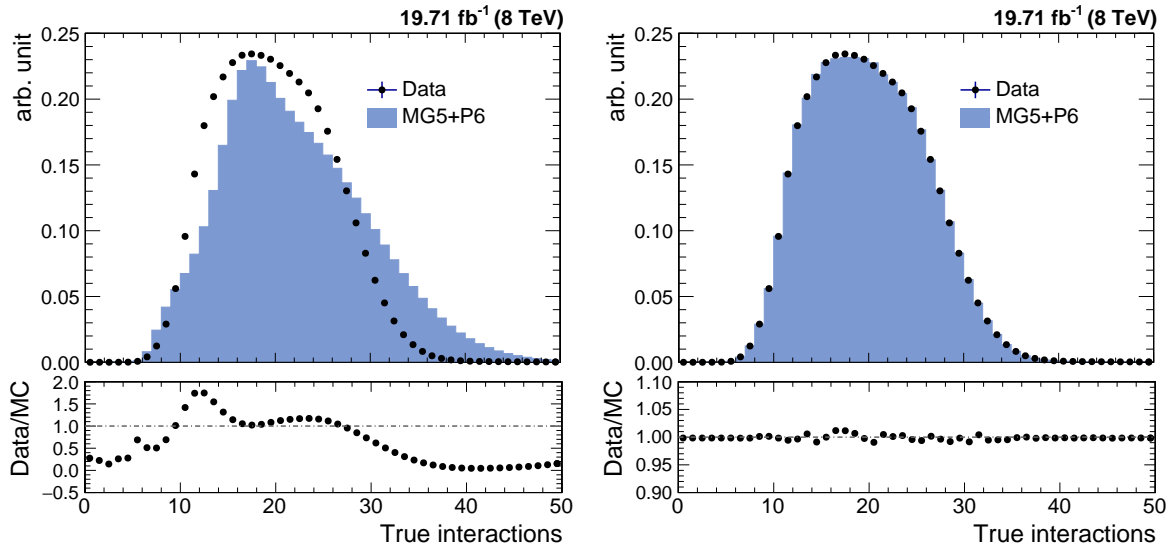


Figure 5.6: Number of reconstructed vertices in data (black solid circles) and simulated Monte Carlo events (blue histogram) before (left) and after (right) the pileup reweighting.

### 5.3.2 Comparison of Cross-sections and their Ratio

The measured data distribution of differential cross-section at detector level is compared to the predictions of Monte Carlo simulation using **MADGRAPH5** generator interfaced with **PYTHIA6** (MG5+P6) including the detector simulation as well as to a fixed-order theory prediction obtained using CT10-NLO PDF set. Figure 5.7 shows

the comparison of differential cross-section as a function of  $H_{T,2}/2$  for  $n_j \geq 2$  (left) and  $n_j \geq 3$  events (right), for data (black solid circles), MG5+P6 MC (red empty circles) and CT10-NLO (blue histogram). The bottom panel in each plot shows the ratio of data to the MC predictions (red line) as well as to the CT10-NLO theory predictions (blue line). The NLO predictions on parton level are not corrected for non-perturbative effects. Still the NLO predictions describe the data better as compared to the LO MC simulations which roughly describes the spectrum on detector level. The sufficient data for  $n_j \geq 2$  and  $n_j \geq 3$  events are available up to  $H_{T,2}/2 = 2000$  GeV and 1680 GeV, respectively. Due to some kinematical constraints, the minimum cut on  $H_{T,2}/2$  is 300 GeV (explained in Sec. 6.1.1). Hence the differential cross-sections are studied in the range  $300 \text{ GeV} \leq H_{T,2}/2 < 2000 \text{ GeV}$  for  $n_j \geq 2$  and  $300 \text{ GeV} \leq H_{T,2}/2 < 1680 \text{ GeV}$  for  $n_j \geq 3$  events.

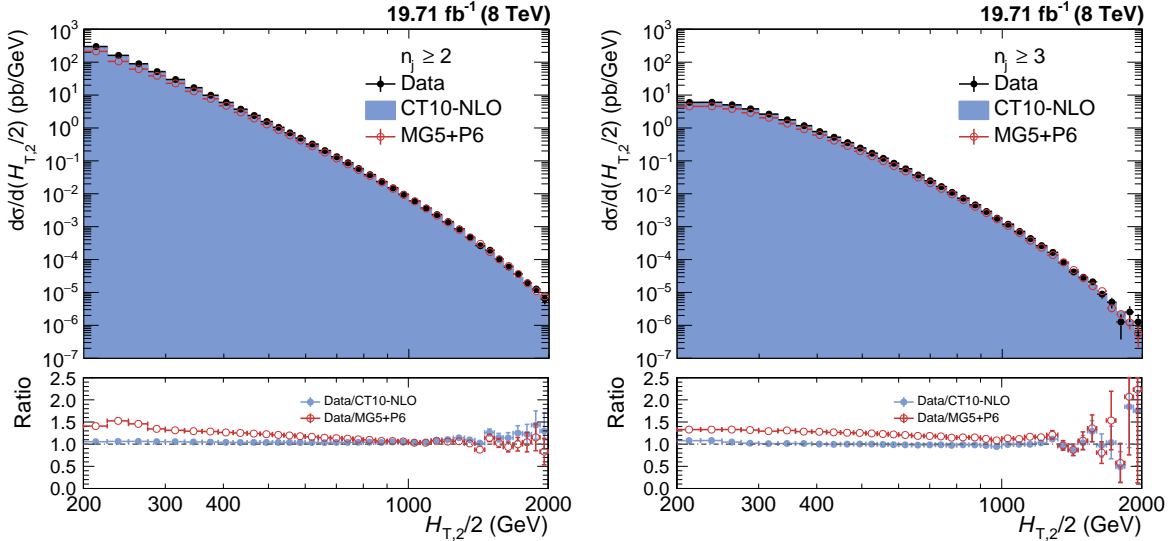


Figure 5.7: The differential cross-sections are compared for data (black solid circles) and LO MADGRAPH5+PYTHIA6 (MG5+P6) Monte Carlo (red empty circles), at reconstructed level with CT10-NLO theory predictions (blue histogram), as a function of  $H_{T,2}/2$  for inclusive 2-jet (left) and 3-jet events (right). Ratios of data to the Monte Carlo predictions (red line) as well as to the CT10-NLO predictions (blue line) are shown in bottom panel of each plot.

The ratio of differential cross-sections,  $R_{32}$  as a function of  $H_{T,2}/2$ , is extracted by dividing the cross-section of selected inclusive 3-jet events to that of

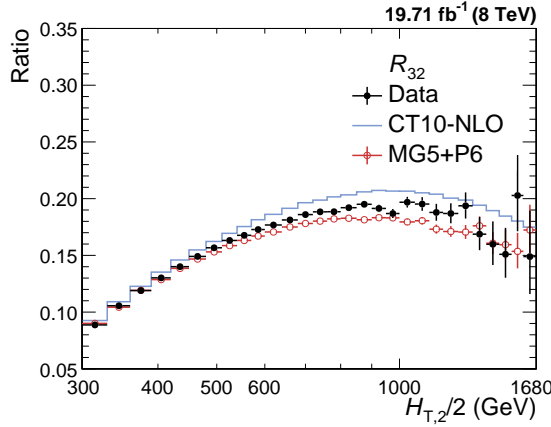


Figure 5.8: Comparison of the cross-section ratio  $R_{32}$  as a function of  $H_{T,2}/2$ , for data (black solid circles) and LO MADGRAPH5+PYTHIA6 (MG5+P6) Monte Carlo (red empty circles), at reconstructed level with CT10-NLO theory predictions (blue line). The error bars give the asymmetrical statistical uncertainty, calculated by the Wilson score interval method which takes into the account the correlation between the numerator and denominator.

inclusive 2-jet events at any given bin size of  $H_{T,2}/2$ . In the cross-section ratios, the numerator and denominator are not independent samples. So to calculate the statistical uncertainty for the cross-section ratios at reconstructed level, the Wilson score interval method is used which takes into account the correlation between the numerator and the denominator and give asymmetric errors. Figure 5.8 shows the comparison of the cross-section ratio  $R_{32}$  as a function of  $H_{T,2}/2$ , for data (black solid circles) and LO MADGRAPH5+PYTHIA6 (MG5+P6) Monte Carlo (red empty circles), at reconstructed level with CT10-NLO theory predictions (blue line). Since in  $n_j \geq 3$  events, the enough statistics for differential cross-section is available up to 1680 GeV of  $H_{T,2}/2$  only,  $R_{32}$  is also studied in the range  $300 \text{ GeV} \leq H_{T,2}/2 < 1680 \text{ GeV}$ . The bin-wise inclusive 2-jet and 3-jet events differential cross-sections as well as their ratio  $R_{32}$ , calculated at detector level, along with statistical uncertainty (in %) are tabulated in Table A.1.

## 5.4 Jet Energy Resolution (JER)

In an ideal experiment, the value of a physical quantity would be determined exactly with an infinite precision. For e.g. whenever a particle with energy  $E$  passes an ideal calorimeter having infinite resolution, the measured energy should always be equal to  $E$ . But in real world, the measured energy of the above mentioned particle might differ from the value  $E$ . This difference of the measured quantity from its true value may be due to detector noise, uncertainties in the calibration, non-linearity of the response etc. Hence this results in the finite value of the resolution of the detector known as jet energy resolution (JER). In such case, the measured values of energy of different particles, passing through the same detector with same energy  $E$ , will be different. Such measurements are described by a Gaussian distribution which is centered around the true value of the measured quantity and its width is generally interpreted as detector resolution. Hence the importance of the detector resolution lies in the fact that it indicates how much the measured value of the observable differs from the true one i.e. how precisely a physical observable can be measured. The narrower the distribution, the higher the resolution is and hence the more efficient is the detector.

Due to finite resolution of the CMS detector, the measured transverse momentum of jets gets smeared. Since the observable in this study i.e.  $H_{T,2}/2$  is the average sum of transverse momentum of leading and sub-leading jets, the resolution of the detector has to be studied in terms of the observable. CMS detector simulation based on MG5+P6 MC event generators is used to determine the resolution as both the particle and reconstructed level information is available. The jets clustered from stable generator particles called Gen jets as well as from particle flow candidates reconstructed from the simulated detector output called Reco jets, are used. The studies of the JETMET working group at CMS has shown that the jet energy resolution in data is actually worse than in simulation [70]. So the reconstructed jet transverse momentum needs to be smeared additionally to match the

resolution in data. Table 5.5 shows the scaling factors (c) which need to be applied on the transverse momentum of simulated reconstructed jets. The scaling factors depend on the absolute  $\eta$  of the jet. The uncertainty on these measured scaling factors ( $c_{central}$ ) needs to be taken into account in a physics analysis. This is done by smearing the reconstructed jets with two additional sets of scaling factors,  $c_{up}$  and  $c_{down}$ , that correspond to varying the factors up and down respectively, by one sigma and evaluating the impact of these new sets.

Table 5.5: JETMET working group at CMS has shown that the jet energy resolution in data is actually worse than in simulation [70]. To match the resolution in data, the reconstructed jet transverse momentum in simulated events need to be smeared by applying the scale factors. The uncertainty on the resolution is given by an upwards and downwards variation  $c_{up}$  and  $c_{down}$  of the measured scaling factor  $c_{central}$ .

$\eta$	0.0 - 0.5	0.5 - 1.1	1.1 - 1.7	1.7 - 2.3	2.3 - 2.8
$c_{central}$	1.079	1.099	1.121	1.208	1.254
$c_{down}$	1.053	1.071	1.092	1.162	1.192
$c_{up}$	1.105	1.127	1.150	1.254	1.316

The reconstructed jet  $p_T$  is smeared randomly using a Gaussian width widened by the scaling factor ( $c_{central}$ )

$$p_T \rightarrow Gauss \left( \mu = p_T, \sigma = \sqrt{c_{central}^2 - 1} \cdot \text{JER}(p_T) \right) \quad (5.6)$$

where  $\text{JER}(p_T)$  is the resolution determined as a function of jet  $p_T$  using MG5+P6 MC simulated events. After smearing transverse momentum of each reco jet,  $H_{T,2}/2$  is calculated from both generator particle jets (Gen  $H_{T,2}/2$ ) as well as the particle flow or reconstructed jets (Reco  $H_{T,2}/2$ ). Then the response is calculated as defined in the Eq. 5.7.

$$R = \frac{\text{Reco } H_{T,2}/2}{\text{Gen } H_{T,2}/2} \quad (5.7)$$

The width of the response distribution in a given Gen  $H_{T,2}/2$  bin is interpreted

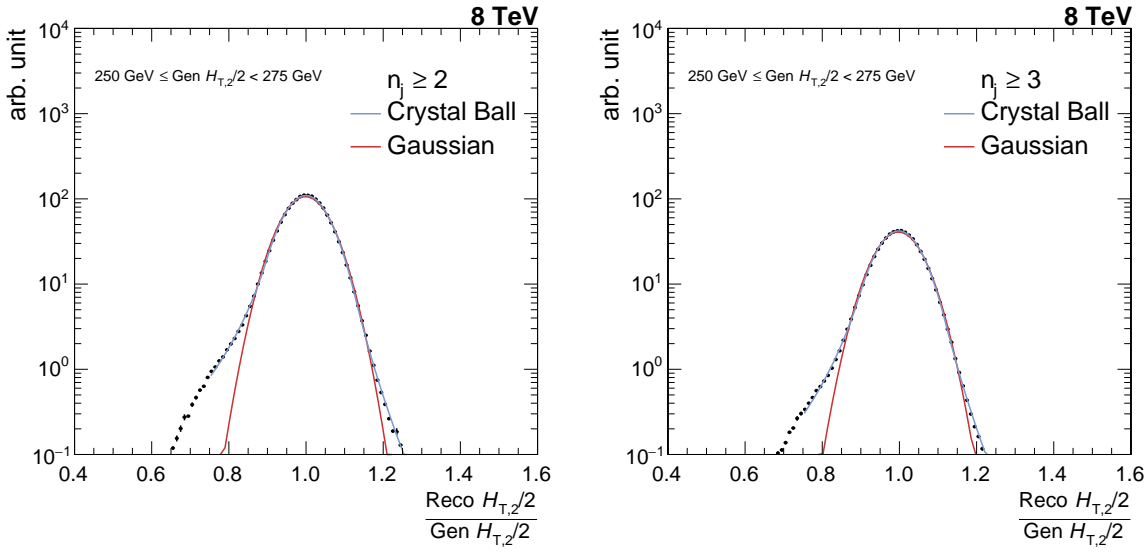


Figure 5.9: Fitting of the resolution distribution, obtained using LO MADGRAPH5+PYTHIA6 (MG5+P6) Monte Carlo simulated events, as a function of  $H_{T,2}/2$  for inclusive 2-jet (left) and 3-jet events (right). The blue line shows the double-sided Crystal Ball function fit of  $\frac{\text{Reco } H_{T,2}/2}{\text{Gen } H_{T,2}/2}$  in each Gen  $H_{T,2}/2$  bin, overlaid by Gaussian fitting the core of the resolution (red line).

as the resolution which in good approximation can be described by the  $\sigma$  of a Gaussian fit of the response distribution. A double-sided Crystal-Ball function takes into account the non-Gaussian tails of the jet response distribution. The resolution as a function of  $H_{T,2}/2$  is calculated separately for both  $n_j \geq 2$  and  $n_j \geq 3$  events. A fit example for one Gen  $H_{T,2}/2$  bin is shown in Fig. 5.9 for  $n_j \geq 2$  (left) and 3-jet events (right). Here the black dots represent the jet response distribution and the double-sided Crystal-Ball fit (blue line) is overlayed by the Gaussian fit (red line). The resolution in each Gen  $H_{T,2}/2$  bin is then plotted as a function of Gen  $H_{T,2}/2$ .

As expected, it has been observed from Fig. 5.10 that the Crystal Ball function (blue solid circles) describes the measured distributions better as compared to Gaussian function fit (red solid circles), especially in the low- $H_{T,2}/2$  region where the non-Gaussian tails are more pronounced. Hence JER is determined using Crystal Ball function fit. Figure 5.11 shows the final relative jet energy resolution (JER) which is described by a modified version of the NSC formula (blue solid line) [71],

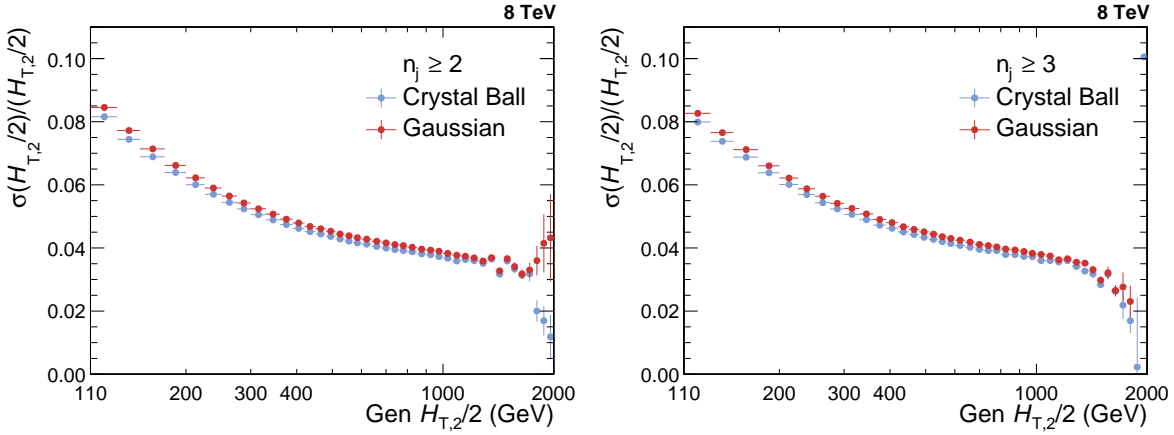


Figure 5.10: Comparison of jet energy resolution calculated using Crystal-Ball fit function (blue solid circles) and Gaussian fit function (red solid circles) for inclusive 2-jet (left) and 3-jet events (right).

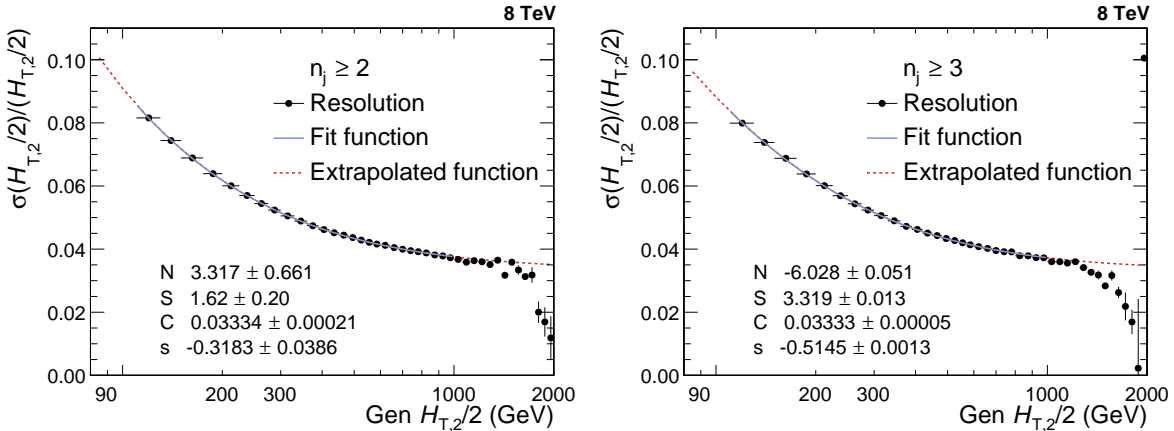


Figure 5.11: Jet energy resolution (JER) is shown as a function of  $\text{Gen } H_{T,2}/2$  for inclusive 2-jet (left) and 3-jet events (right). JER (black solid circles) is fitted by using the modified NSC-formula (blue solid line) which is extrapolated to 80 GeV and up to 2000 GeV (red dashed line) to consider the migration into lower as well as higher bins.

as mentioned in Equation 5.8. To consider the migration to lower as well higher bins and to obtain the resolution with reasonable statistics over the full range of  $\text{Gen } H_{T,2}/2$ , the fit function is extrapolated to 80 GeV and up to 2000 GeV which is shown by red dashed line. The fit formula used here is basically the usual NSC formula which describes the resolution in terms of noise  $N$  originating due to electronic and pileup noise and is independent of  $H_{T,2}/2$ ; a stochastic component  $S$  due to sampling fluctuation and EM fraction fluctuation per hadrons; and a constant term  $C$

because of dead material, magnetic field and calorimeter cell to cell fluctuation. In the low  $H_{T,2}/2$  region the tracking has a non-negligible influence on the resolution due to the particle flow algorithm, so the additional parameter  $s$  is introduced to obtain slightly better fits. The parameters obtained after fitting the relative resolution using the above mentioned NSC formula are tabulated in Table 5.6 for  $n_j \geq 2$  and  $n_j \geq 3$  events. This calculated JER is used in unfolding procedure to smear the generated truth spectrum which is used as input in getting the response matrices and is explained in details in Sec. 5.5.1. Since JER in  $n_j \geq 2$  events is similar to that one in  $n_j \geq 3$  events, so N, S and C fit parameters obtained for  $n_j \geq 3$  events are used for unfolding  $R_{32}$ .

$$\frac{\sigma(x)}{x} = \sqrt{\operatorname{sgn}(N) \cdot \frac{N^2}{x^2} + S^2 \cdot x^{s-1} + C^2} \quad (5.8)$$

Table 5.6: The parameters obtained by fitting the relative resolution as a function of  $H_{T,2}/2$ , using the modified NSC formula, for inclusive 2-jet and 3-jet events.

	N	S	C	s
Inclusive 2-jet	3.32	1.62	0.0333	-0.318
Inclusive 3-jet	-6.03	3.32	0.0333	-0.515

Since the JER is calculated using MG5+P6 Reco and Gen  $H_{T,2}/2$  distributions, so it is expected that if Gen  $H_{T,2}/2$  is smeared using this JER, it should match the Reco  $H_{T,2}/2$ . But this extracted JER in one large rapidity bin, smears the Gen  $H_{T,2}/2$  too much because Smeared Gen/Gen ratio (red line) shows a discrepancy from simulated Reco/Gen ratio (blue line), as observed in Fig. 5.12 for  $n_j \geq 2$  (left) and  $n_j \geq 3$  events (right). Some shortcomings in the detector simulation of the theory spectra leads to these small nonclosures. When the 30% reduced JER is used to smear Gen, then the ratio Smeared Gen/Gen (pink line) matches with simulated Reco/Gen ratio (blue line) within the statistical fluctuations. Hence an additional

unfolding uncertainty is attributed by comparison to 30% reduced JER for both  $n_j \geq 2$  and  $n_j \geq 3$  events. Due to high statistical fluctuations at high  $H_{T,2}/2$ , range is presented up to 1680 GeV only.

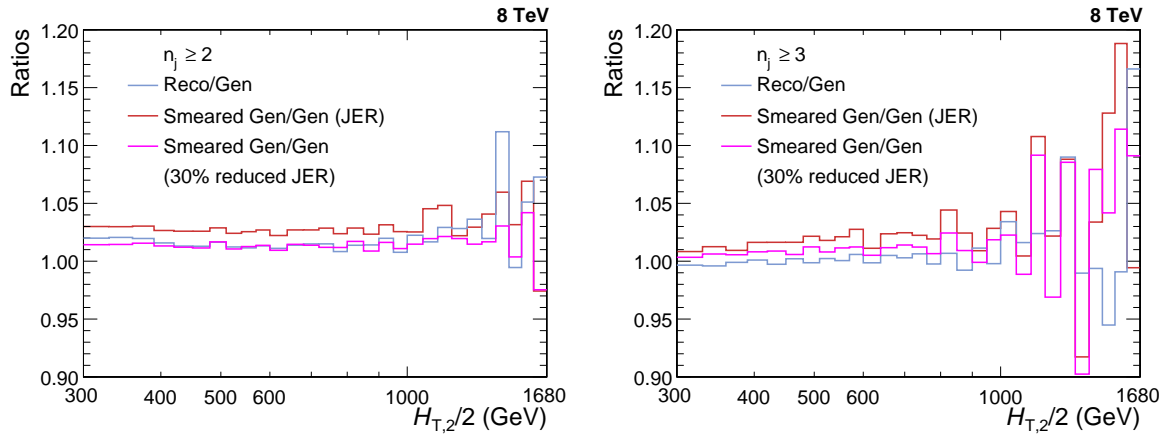


Figure 5.12: MADGRAPH5+PYTHIA6 (MG5+P6) Gen smeared using extracted jet energy resolution (JER) shows a discrepancy from simulated Reco as Smeared Gen/Gen ratio (red line) does not match with Reco/Gen ratio (blue line), for both inclusive 2-jet (left) and 3-jet events (right). Smeared Gen/Gen ratio (pink line) where Gen is smeared using 30% reduced JER matches with simulated Reco/Gen ratio (blue line) within the statistical fluctuations. Hence an additional unfolding uncertainty is attributed by comparison to 30% reduced JER.

## 5.5 Unfolding

One of the main goals in an experimental measurement is to do the comparison of data with theory predictions or with the results obtained from other experiments. But the finite resolution of a detector and the steeply falling jet  $p_T$  spectrum distorts the physical quantities. As a result, the measured observables are different from their corresponding true values. Each  $p_T$  bin content contains the migrated events from neighbouring bins along with the original events. So an unfolding process of the data should be followed in order to remove detector effects. In this analysis, the measurements are corrected for detector smearing effects and unfolded to stable particle level by using the iterative D'Agostini Bayesian algorithm [72, 73] as implemented in RooUnfold software package [74]. In this algorithm, the number of iterations reg-

ularize the unfolding process. The obtained distribution in one iteration is taken as the input in the next one.  $\chi^2$  between two successive iterations is given by Eq. 5.9. The number of iterations stop when  $\chi^2/N_{bins}$  is  $< 1$ . A reduced  $\chi^2$  is obtained by a higher number of iterations but this will also increase the uncertainty and there are larger bin-by-bin fluctuations and correlations. So the optimization of number of iterations is very important. In the current analysis, unfolding done with “four” iterations gives the best results with low  $\chi^2$  and low bin-by-bin correlations.

$$\chi^2 = \sum_{i=1}^{N_{bins}} \left( \frac{n_i^{j+} - n_i^j}{\sqrt{n_i^j}} \right)^2 \quad (5.9)$$

where  $n_i^j$  number of events in  $i$ -th bin for  $j$ -th iteration.

The measured differential cross-sections as a function of  $H_{T,2}/2$ , are unfolded separately for  $n_j \geq 2$  and  $n_j \geq 3$  events. The measured cross-section ratio  $R_{32}$  is also corrected for detector smearing effects and unfolded to particle level. There can be two ways to obtain unfolded cross-section ratio :

- **Method I :** First unfold separately the inclusive 2-jet and 3-jet measured cross-sections and then construct the ratio  $R_{32}$
- **Method II :** Unfold directly the cross-section ratio  $R_{32}$

In further analysis, unfolded cross-section ratio  $R_{32}$  and its systematic uncertainties are calculated using Method I, whereas Method II is used only to propagate the statistical uncertainties including bin-by-bin correlations and statistical correlations between the inclusive 3-jet and 2-jet events cross-sections. Unfolding takes the response matrix as an input which are explained in the next section.

### 5.5.1 Response Matrices

The response matrix is a two dimensional mapping between the true and measured distributions. It is usually derived from simulated Monte Carlo (MC) samples, which takes the true distribution from MC as an input and smears it by taking into account the detector resolution. Then this response matrix is used to unfold the measured data spectrum. But there are several drawbacks of constructing response matrix using this method. In some phase space regions, the shape of the distribution is not well described by the LO predictions. Also, the limited number of events in the MC samples at high transverse momenta introduces high statistical fluctuations in the response matrix.

However, there is an indirect way of constructing the response matrix which uses a custom Toy Monte Carlo method. In this method, the particle level or true  $H_{T,2}/2$  spectrum is obtained by fitting the theoretically predicted NLO spectrum. Then this distribution is smeared with forward smearing technique, using the extracted jet energy resolution (JER) to obtain the reconstructed level or measured  $H_{T,2}/2$  spectrum. After that, the response matrix is constructed from these two distributions is used for the unfolding procedure.

#### 5.5.1.1 Inclusive Cross-sections

The NLO spectrum of the differential cross-sections for  $n_j \geq 2$  and  $n_j \geq 3$  events obtained using CT10-NLO PDF set are fitted with the following two different functions defined in Eq. 5.10 and 5.13. These functions describes the shape as well as normalization of the distribution.

- **Function I :**

$$f(H_{T,2}/2) = N[x_T]^{-a}[1 - x_T]^b \times \exp[-c/x_T] \quad (5.10)$$

where  $N$  is normalization factor and  $a, b, c$  are fit parameters.

This function is derived from the below function [75] :

$$f(p_T; \alpha, \beta, \gamma) = N_0[p_T]^{-\alpha} \left[ 1 - \frac{2 p_T \cosh(y_{min})}{\sqrt{s}} \right]^{\beta} \times \exp[-\gamma/p_T] \quad (5.11)$$

using

$$\alpha = a, \quad \beta = b, \quad \gamma = c * \sqrt{s}/2, \quad x_T = \frac{2 * H_{T,2}/2 * \cosh(y_{min})}{\sqrt{s}} = \frac{2 * H_{T,2}/2}{\sqrt{s}} \quad (5.12)$$

where transverse scaling variable  $x_T$  corresponds to the proton fractional momentum  $x$  for dijets with rapidity  $y = 0$ ,  $\sqrt{s} = 8000$  GeV and  $y_{min}$  is low-edge of the rapidity bin  $y$  under consideration (here  $y_{min}$  is taken equal to 0)

### • Function II :

$$f(H_{T,2}/2) = A_0 \left( 1 - \frac{H_{T,2}/2}{A_6} \right)^{A_7} \times 10^{F(H_{T,2}/2)}, \text{ where } F(x) = \sum_{i=1}^5 A_i \left( \log \left( \frac{x}{A_6} \right) \right)^i \quad (5.13)$$

where the parameter  $A_6$  is fixed to  $\frac{\sqrt{s}}{2 \cosh(y_{min})}$ , where  $\sqrt{s} = 8000$  GeV and  $y_{min}$  is the minimum rapidity. The other parameters are derived from the fitting.

Figure 5.13 shows the fitted CT10-NLO spectrum of differential cross-section as a function of  $H_{T,2}/2$  (green solid circles) using Function I (top) and using Function II (bottom) : for inclusive 2-jet (left) and 3-jet events (right). Function I is used primarily to generate response matrices and perform the closure tests and Function II is used as an alternative function to calculate unfolding uncertainty, described in Sec. 5.6.3. To include the migration to lower bins, the fit functions described by red lines are extrapolated to 80 GeV (blue dashed lines).

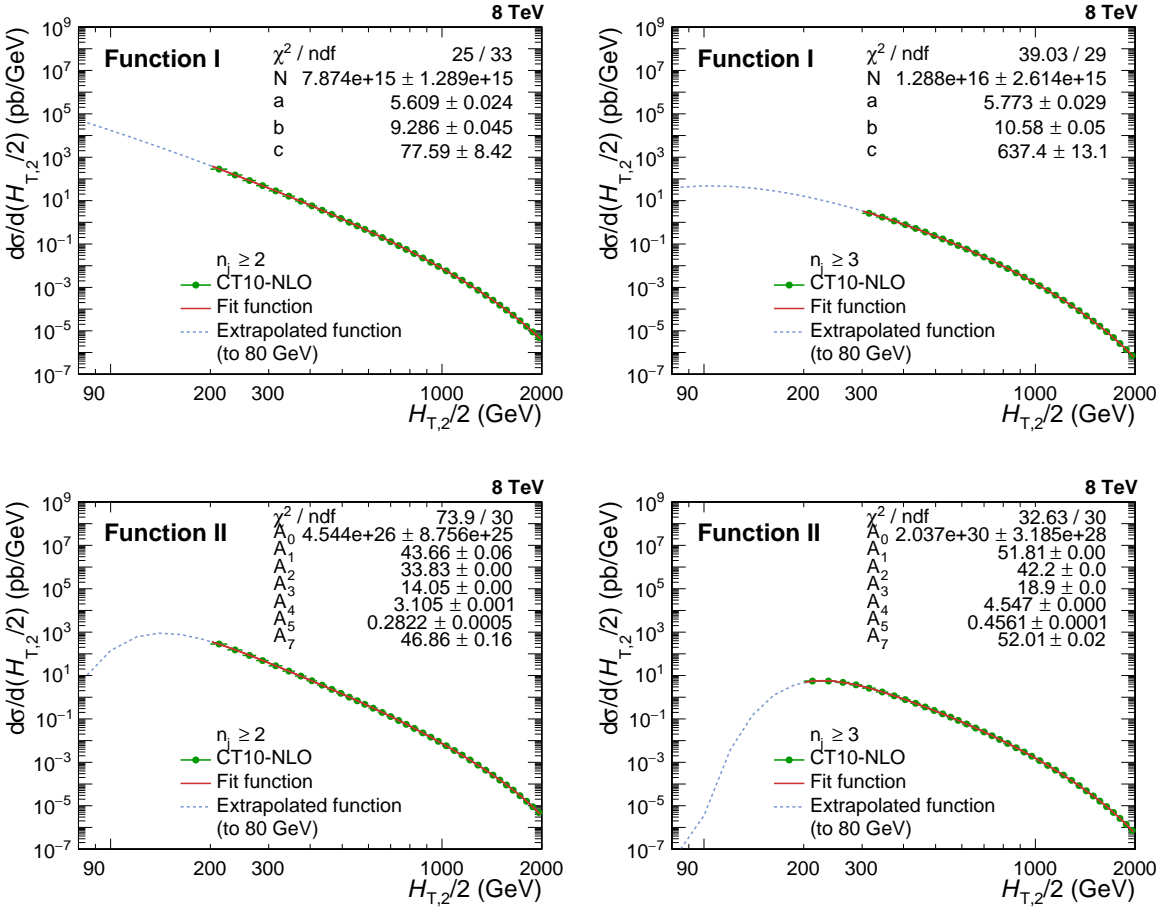


Figure 5.13: Fitted CT10-NLO spectrum of differential cross-section as a function of  $H_{T,2}/2$  (green solid circles) using Function I (top) defined in Eq. 5.10 and using Function II (bottom) given by Eq. 5.13, for inclusive 2-jet (left) and 3-jet events (right). To consider the migration to lower  $H_{T,2}/2$  bins, the fit functions described by red lines are extrapolated to 80 GeV (blue dashed lines).

A flat  $H_{T,2}/2$  spectrum is generated by using toy Monte Carlo events and the fit parameters obtained from the NLO spectrum using function I (as shown in Fig. 5.13) provides weights to the flat spectrum. A total of ten million events are generated randomly (in  $H_{T,2}/2$  range 80-2000). These generated values are then smeared with a Gaussian function, where  $\sigma$  of the Gaussian is determined from the relative resolution parametrization as a function of  $H_{T,2}/2$  calculated from NSC formula mentioned in equation 5.8. The parameters N, S, C used for smearing are taken from Table 5.6. These randomly generated ( $\text{Gen}_{\text{Toy}}$ ) and smeared ( $\text{Measured}_{\text{Toy}}$ ) values are used to fill the response matrices. Figure 5.14 shows the response matrices derived using

the Toy MC for  $n_j \geq 2$  (left) and  $n_j \geq 3$  events (right). The matrices are normalized to the number of events in each column. The response matrices are diagonal as the migrations in off-diagonal bins are much smaller than the bins along the diagonal.

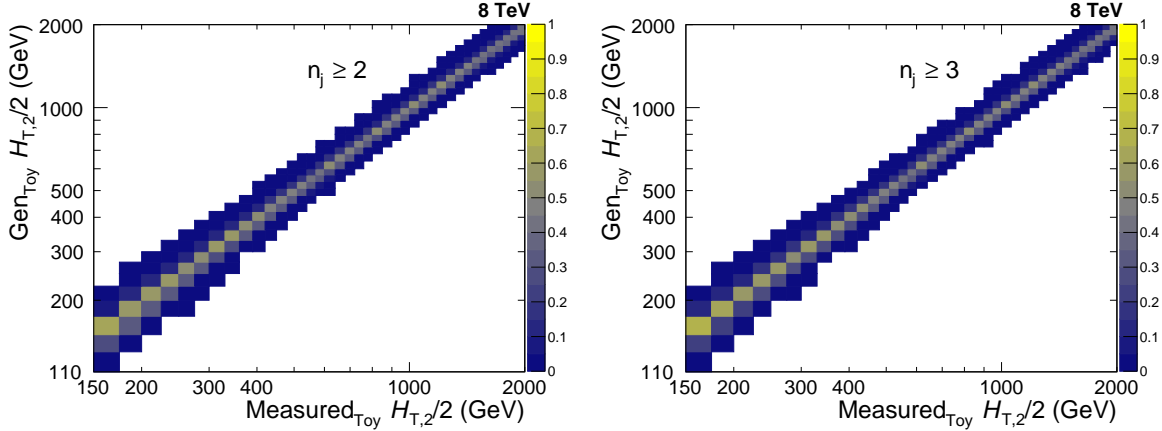


Figure 5.14: The response matrices are derived using the Toy Monte Carlo and forward smearing method, for inclusive 2-jet (left) and 3-jet events (right). The matrices are normalized to the number of events in each column and are diagonal with small off-diagonal migrations between close-by  $H_{T,2}/2$  bins.

### 5.5.1.2 Cross-section Ratio, $R_{32}$

To obtain the statistical uncertainty on the unfolded cross-section ratio  $R_{32}$ , Method II is used. In this method, the response matrix is constructed using Toy MC method as done in Sec. 5.5.1.1 for differential cross-sections. To obtain the true spectrum for  $R_{32}$ , the ratio of cross-section spectrum described by Eq. 5.10 for inclusive 3-jet to that of 2-jet events is taken. This ratio is shown by green solid circles in Fig. 5.15 (left) which is fitted using a polynomial function of degree 8 (red line). Then as explained in above section, response matrix is derived for  $R_{32}$  using the Toy Monte Carlo and forward smearing method which is shown in Fig. 5.15 (right). The matrix is normalized to the number of events in each column and is diagonal with small off-diagonal migrations between close-by  $H_{T,2}/2$  bins.

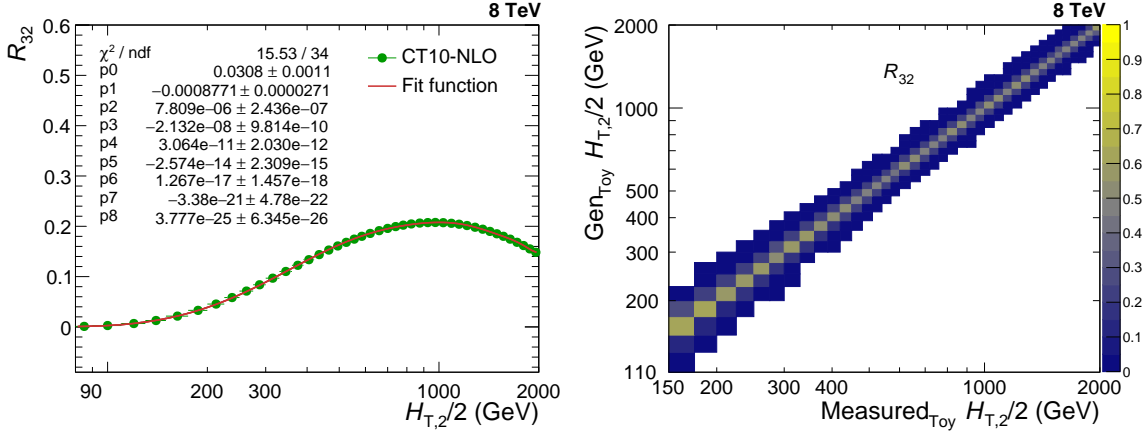


Figure 5.15: Left : The ratio of cross-sections described by Eq. 5.10 for inclusive 3-jet to that of 2-jet events is shown as a function of  $H_{T,2}/2$  (green solid circles). It is fit using a polynomial function of degree 8 (red line). Right : The response matrix is derived using the Toy Monte Carlo and forward smearing method, for the cross-section ratio  $R_{32}$ . The matrix is normalized to the number of events in each column and is diagonal with small off-diagonal migrations between close-by  $H_{T,2}/2$  bins.

### 5.5.2 Closure Test

A closure test has been performed to confirm the working of the unfolding procedure. In this test,  $\text{Measured}_{\text{Toy}}$  spectrum is unfolded using the constructed response matrices shown in Figure 5.14. It is expected that the same  $\text{Gen}_{\text{Toy}}$  spectrum should be re-obtained after unfolding. Figure 5.16 confirms that the unfolded  $\text{Measured}_{\text{Toy}}$  spectrum matches exactly with  $\text{Gen}_{\text{Toy}}$  spectrum as the ratio of these distributions is perfectly flat at one for both  $n_j \geq 2$  (top left) and  $n_j \geq 3$  events (top right) cross-sections as well as the cross-section ratio  $R_{32}$  (bottom).

For another closure test, Reco MG5+P6 MC differential cross-section distribution is unfolded using the above constructed response matrices using JER for forward smearing the randomly generated spectrum. While taking ratio of the unfolded distribution to that of Gen MG5+P6 MC, it is observed that a well closure is not obtained. This is represented by blue line in Fig. 5.17 for  $n_j \geq 2$  (top left) and  $n_j \geq 3$  events (top right). As observed in Fig. 5.12 in Sec. 5.4, if Reco MG5+P6 MC is unfolded using the response matrices obtained using 30% reduced JER, then the

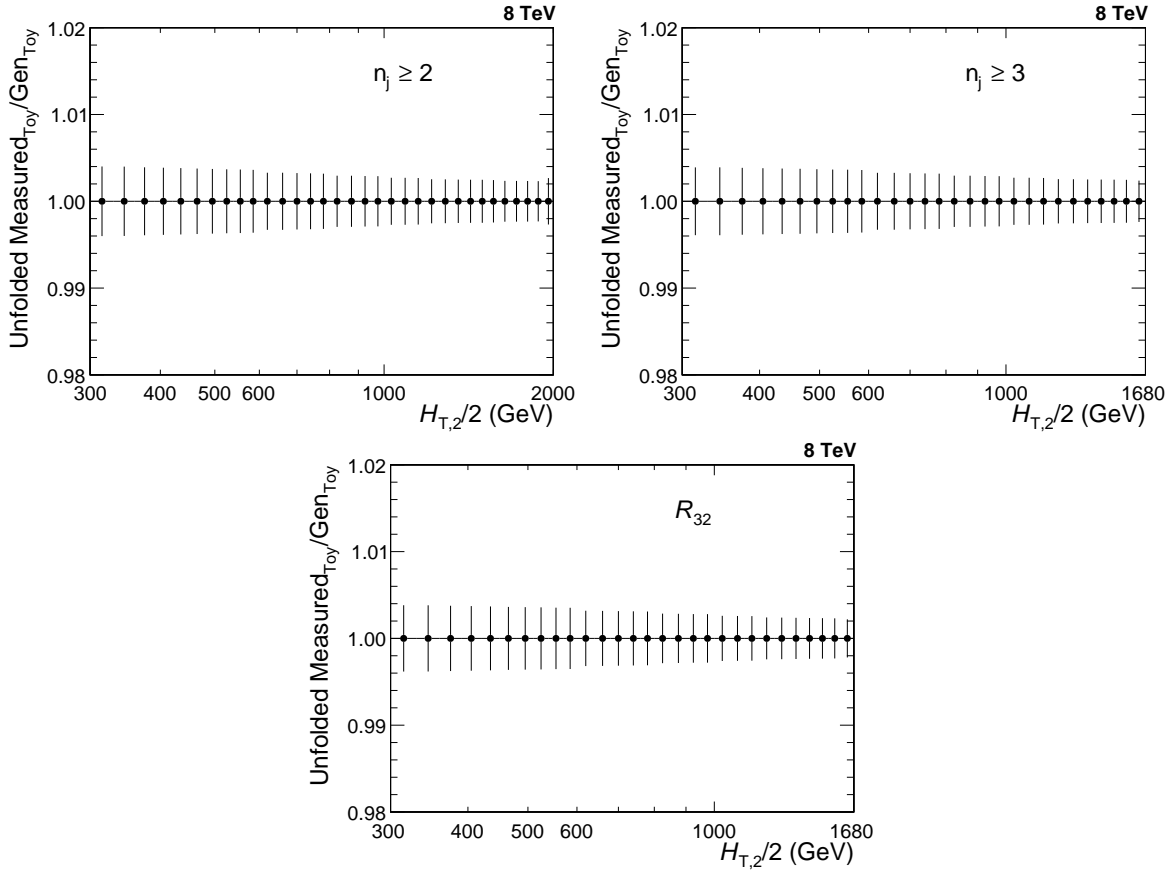


Figure 5.16: Closure test of the unfolding technique where the smeared spectrum obtained from Toy Monte Carlo method (Measured<sub>Toy</sub>), is unfolded using the constructed response matrices (obtained by forward smearing the randomly generated spectrum (Gen<sub>Toy</sub>) using extracted jet energy resolution (JER)). As expected, the unfolded measured<sub>Toy</sub> spectrum matches exactly with Gen<sub>Toy</sub> spectrum as the ratio of these distributions is perfectly flat at one for both inclusive 2-jet (top left) and 3-jet events (top right) cross-sections as well as the cross-section ratio  $R_{32}$  (bottom).

good closure is obtained as shown by red line in Fig. 5.17. Since unfolded cross-section ratio  $R_{32}$  is the ratio of unfolded differential cross-sections (Method I), same behaviour is observed for  $R_{32}$  (bottom).

### 5.5.3 Unfolding of the Measurement

After validity the unfolding method, the measured differential cross-sections as well as  $R_{32}$  are unfolded using the above reconstructed response matrices. The unfolded data spectrum is compared to that of measured one in Fig. 5.18 for  $n_j \geq 2$  (top

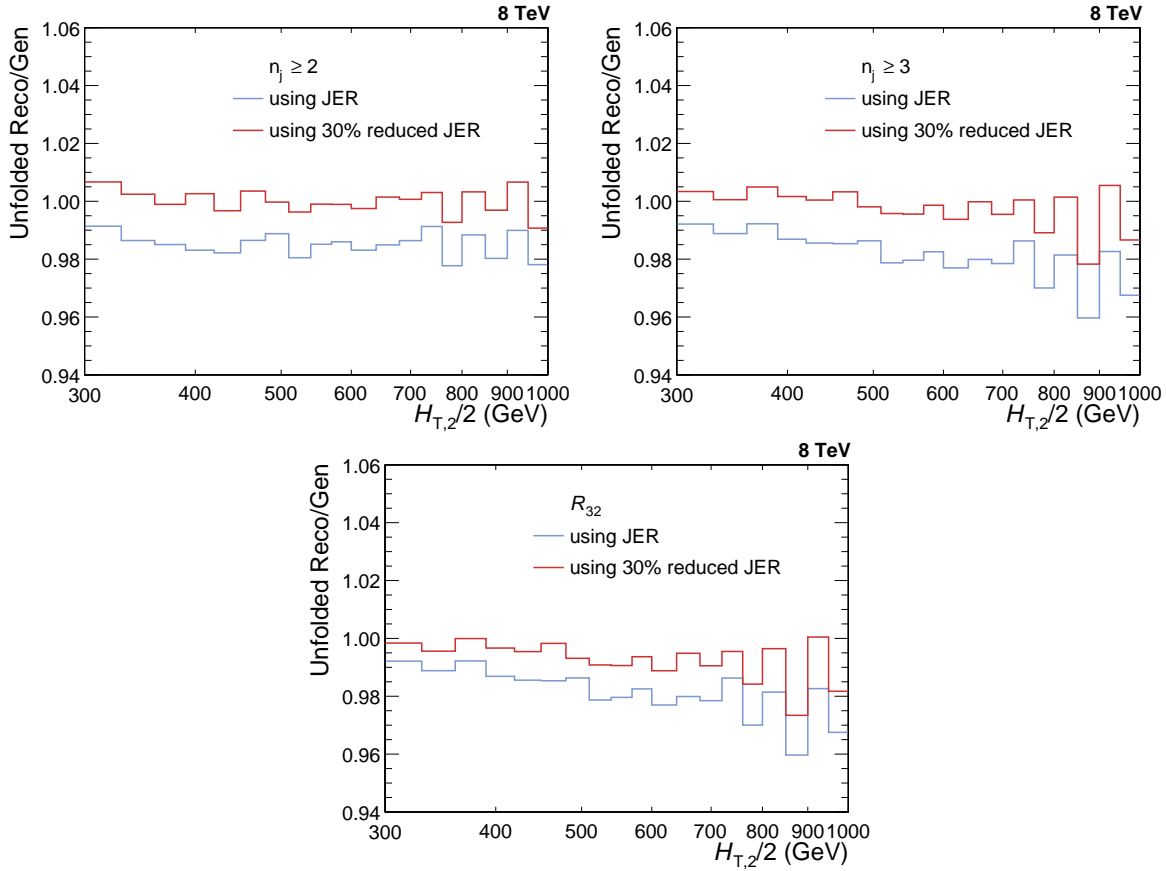


Figure 5.17: Reco MADGRAPH5+PYTHIA6 Monte Carlo (MG5+P6 MC) differential cross-section distributions unfolded with the response matrices (obtained by forward smearing the randomly generated spectrum (Gen) using extracted jet energy resolution (JER)), does not give a good closure with Gen MG5+P6 MC (blue line), for inclusive 2-jet (top left) and 3-jet events (top right). After performing the unfolding using 30% reduced JER, a good closure is obtained (red line). Since unfolded the cross-section ratio  $R_{32}$  is the ratio of unfolded differential cross-sections, same behaviour is observed for  $R_{32}$  (bottom).

left) and  $n_j \geq 3$  events (top right) cross-sections and for the cross-section ratio  $R_{32}$  (bottom). As already discussed that 30% reduced JER gives better closures than JER, so the unfolding of data is done with response matrices using JER (blue solid circles) as well as 30% reduced JER (red solid circles) for smearing. The difference between both is taken as an additional uncertainty on the unfolded measurement.

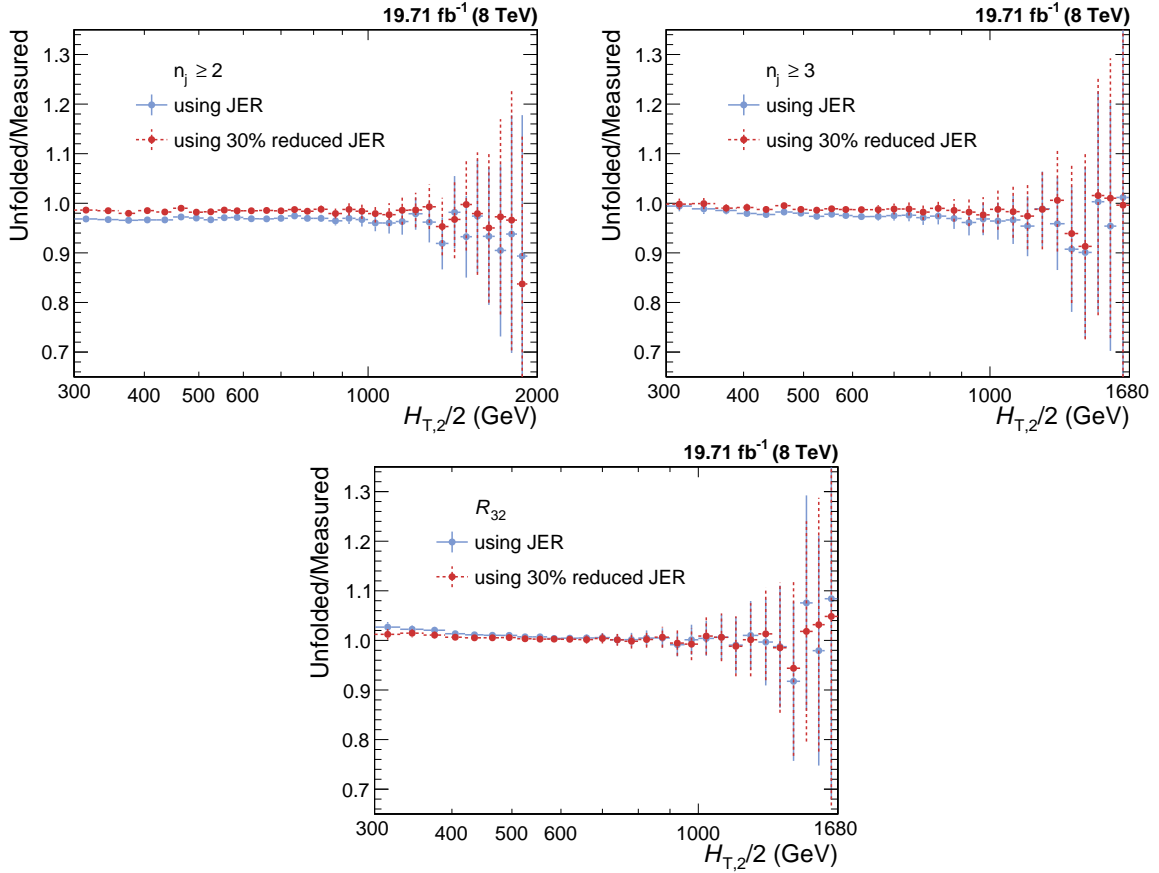


Figure 5.18: The measured differential cross-sections as well as the cross-section ratio  $R_{32}$  are unfolded as a function of  $H_{T,2}/2$  using the response matrices derived using the Toy Monte Carlo and forward smearing method. The unfolded spectrum are compared with that of the measured one for inclusive 2-jet (top left) and 3-jet events cross-sections (right) as well as for  $R_{32}$  (bottom). The unfolding is done with response matrices using JER (blue solid circles) as well as 30% reduced JER (red solid circles) for smearing. The difference between both is taken as an additional uncertainty on the unfolded measurement.

## 5.6 Experimental Uncertainties

In an experimental measurement of any physical observable, the uncertainties play a key role and hence are important to study in a physics analysis. The uncertainties can be categorized into two types : statistical and systematic. The statistical uncertainties arise due to random fluctuations depending on the number of events. The more the number of events, less is the statistical uncertainty. The systematic uncertainties may be due to known detector effects, model dependence, assumptions made or various corrections applied. In general, if the statistical and systematic un-

certainties are uncorrelated, these can be added in quadrature to obtain the total uncertainty on the measurement. In this section, all the experimental uncertainties affecting the measurement of cross-sections and the cross-section ratio  $R_{32}$  are described. The systematic experimental uncertainties for  $R_{32}$  are propagated from the cross-sections to the ratio taking into account correlations. Due to this, the systematic uncertainties may cancel for  $R_{32}$  completely or partially as compared to those for the individual cross-sections.

### 5.6.1 Statistical Uncertainty

Statistical uncertainty on the measurement is obtained through the unfolding procedure using a toy MC method. The measured data points are smeared within their statistical uncertainties to get the smeared spectrum. Such smeared spectrums are produced million in number and the unfolding is performed multiple times for each smeared spectra. The differences between the unfolded spectrums and the measured one give the statistical uncertainty. The unfolding process introduces more statistical fluctuations which can be observed in Fig. 5.19. Here the fractional statistical uncertainties of the unfolded data (red line) are compared with those of the measured one (blue line) for  $n_j \geq 2$  (top left) and  $n_j \geq 3$  events cross-sections (top right) as well as for the cross-section ratio  $R_{32}$  (bottom).

After the unfolding, the final statistical uncertainties become correlated among the bins such that the size of these correlations varies between 10 and 20%. The correlation (anti-) is more significant for neighbouring bins in  $H_{T,2}/2$  as compared to the far off ones. In Fig. 5.20, the correlations of the statistical uncertainty after the unfolding can be seen for  $n_j \geq 2$  (top left) and  $n_j \geq 3$  events cross-sections (top right) and for the cross-section ratio  $R_{32}$  (bottom). These correlations must be considered while performing the fits to extract the value of the strong coupling constant,  $\alpha_S$ .

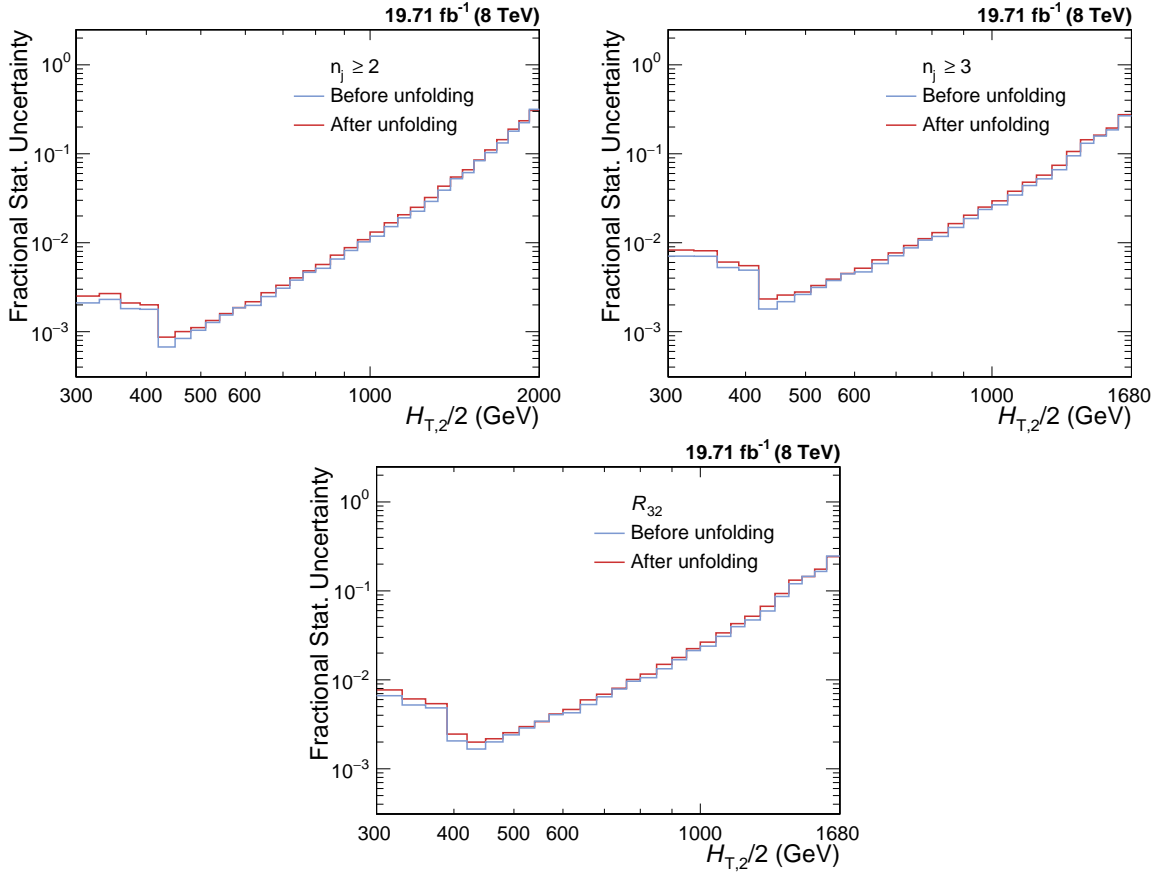


Figure 5.19: The fractional statistical uncertainties of the unfolded data (red line) are compared with those of the measured one (blue line) for inclusive 2-jet (top left) and 3-jet events cross-sections (top right) as well as for the cross-section ratio  $R_{32}$  (bottom). After unfolding, the statistical uncertainty increases slightly.

### 5.6.2 Jet Energy Corrections Uncertainty

As explained in Sec. 4.3.2, the measured jet energy is corrected for a variety of detector effects by using jet energy corrections (JEC). This process introduces uncertainties in the final corrected jet energy. There are 25 mutually independent sources which contribute to JEC. Each source presents a  $1\sigma$  shift and is fully correlated in  $p_T$  and  $\eta$  but uncorrelated to all other sources. The observable is studied with the nominal values of the jet energy which gives nominal distributions as well as by varying up and down the energy of all jets by the uncertainty. The differences between the nominal distributions and the ones obtained by varying the jet energy gives the uncertainties from each source. The JEC uncertainties can be asymmetric

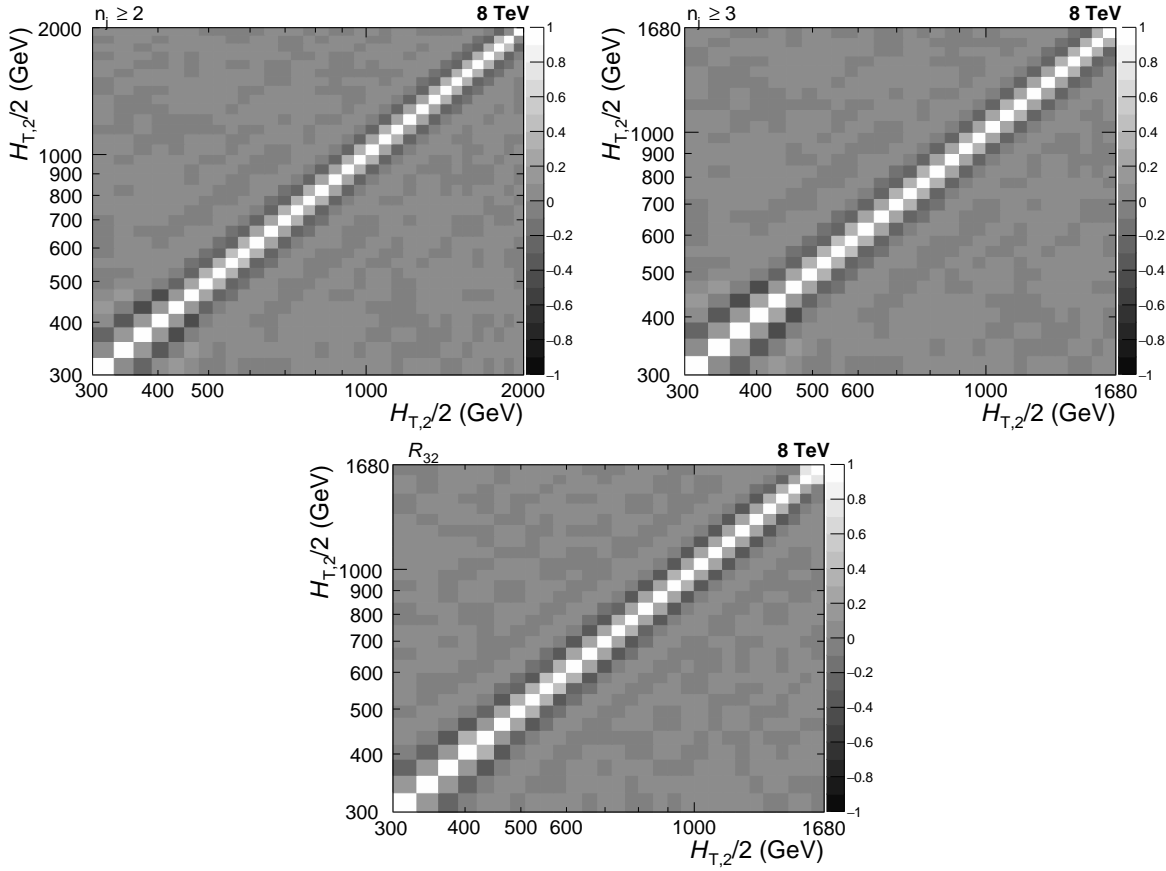


Figure 5.20: The unfolding procedure introduces the correlations of the statistical uncertainty through bin migrations which are shown here for inclusive 2-jet (top left) and and 3-jet events cross-sections (top right) as well as for the cross-section ratio  $R_{32}$  (bottom). The correlation (anti-) is more significant between neighbouring bins than far-ff ones.

in nature which leads to separate treatment of upwards and downwards variation of each source. The sum in quadrature of uncertainties from all sources gives the total JEC uncertainty. In the current analysis, JEC uncertainties are a dominant source of experimental uncertainty at low  $H_{T,2}/2$ . The JEC uncertainty ranges from 3% to 10% for  $n_j \geq 2$  and from 3% to 8% for  $n_j \geq 3$  events cross-sections measurement. To calculate JEC uncertainty for ratio  $R_{32}$ , the inclusive 2-jet and 3-jet events cross-sections are measured as a function of  $H_{T,2}/2$  by shifting the jet  $p_T$  according to the JEC uncertainty for each source of JEC separately. Then the ratio of these cross-sections is taken and the difference of these from the central ratio  $R_{32}$ , gives the JEC uncertainty for  $R_{32}$ . As expected, JEC uncertainty for  $R_{32}$  is small as compared to

that for individual cross-sections and is about 1 to 2% over all  $H_{T,2}/2$  bins.

The sources of JEC considered in the current measurements are : AbsoluteStat, AbsoluteScale, AbsoluteFlavMap, AbsoluteMPFBias, Fragmentation, SinglePionECAL, SinglePionHCAL, FlavorQCD, RelativeJEREC1, RelativeJEREC2, RelativeJERHF, RelativePtBB, RelativePtEC1, RelativePtEC2, RelativePtHF, RelativeFSR, RelativeStatFSR, RelativeStatEC2, RelativeStatHF, PileUpDataMC, PileUpPtRef, PileUpPtBB, PileUpPtEC1, PileUpPtEC2 and PileUpPtHF. The AbsoluteFlavMap uncertainty is exactly zero for the 8 TeV and can be ignored. For the four sources : RelativeJERHF, RelativePtHF, RelativeStatHF, PileUpPtHF, the JEC uncertainty is exactly zero because of  $|y| < 2.5$  cut used in the analysis. So only 20 sources contribute to the total JEC uncertainty. The Figs. A.1-A.3 show the JEC uncertainty from each source separately for inclusive 2-jet (top) and 3-jet events cross-sections (middle) as for cross-section  $R_{32}$  (bottom). Depending on the origin of sources, they are categorized into four groups which are described below in brief :

1. **Pileup** - This uncertainty originates from the differences in the transverse momentum between the true offset and the Random Cone method (i.e. essentially difference of pileup inside and outside of jets), in simulated events. This uncertainty is derived from  $Z/\gamma$ +jet, dijet and multijet data using fit procedure to estimate the residual pileup uncertainty after the calibration.
2. **Relative** - The forward jets are calibrated by the relative  $\eta$ -dependent corrections using dijet events. The main contribution to the uncertainty comes from jet energy resolution (JER), derived by varying JER scale factors up and down by quoted uncertainties and the initial and final state radiation bias corrections.
3. **Absolute** - A global fit to  $Z/\gamma$ +jet and multi-jet events gives the absolute calibration of the jet energy scale. The uncertainties are related to the lepton

momentum scale for muons in  $Z \rightarrow \mu\mu$ +jet and the single pion response in the HCAL.

4. **Flavor** - Flavor response differences are studied from simulation by cross-checking the results with quark- and gluon-tagged  $\gamma$ +jet and  $Z$ +jet events. These uncertainties are based on PYTHIA6.4 and HERWIG++2.3 differences propagated through the data-based calibration method.

The details of the jet energy corrections and uncertainties can be found in [76].

### 5.6.3 Unfolding Uncertainty

The unfolding uncertainty is comprised of three uncertainties which are explained as follows :

1. **Jet Energy Resolution** - The calculation of the jet energy resolution (JER) using simulated MG5+P6 Monte Carlo events is already explained in Sec. 5.4. As mentioned before, the measured jet transverse momentum ( $p_T$ ) in simulated MC events needs to be smeared additionally to match the resolution in data. This smearing is done by using measured scale factors ( $c_{central}$ ) mentioned in Table 5.5. It is recommended by JETMET group that the uncertainty on these measured scaling factors must be taken into account in a physics analysis. Since JER is used in constructing the response matrix which is an input in unfolding procedure, so the uncertainty on scale factors accounts for the unfolding uncertainty. To calculate JER uncertainty,  $p_T$  is smeared with two additional sets of scale factors corresponding to varying the factors up and down by one sigma, and corresponding  $H_{T,2}/2$  is calculated. Then again JER is calculated as a function of  $H_{T,2}/2$  using these upwards ( $c_{up}$ ) and downwards ( $c_{down}$ ) variations of the scaling factors. Alternative response matrices are built using the JER with above variations and the unfolding is performed again. The

differences of the obtained unfolded spectrums to the nominal ones accounts for a systematic JER uncertainty.

2. **Model Dependence** - It is explained in Sec. 5.5.1 that to obtain the true  $H_{T,2}/2$  spectrum to be used in constructing response matrix using Toy MC method, the fitting of the CT10-NLO predictions is performed with the Function I described in Eq. 5.10. Using the alternative function, Function II given by Eq. 5.13, for this fitting and then constructing different response matrix, gives the model dependence of the true  $H_{T,2}/2$  spectrum. The differences in unfolded distributions using the above mentioned two different response matrices gives the model dependence uncertainty.
3. **Additional Uncertainty** - Small nonclosures observed in Fig. 5.12 introduces a supplementary uncertainty which is attributed by comparison of distributions unfolded using response matrices constructed using JER from simulation with that obtained with a 30% reduced JER.

All the three above mentioned uncertainties are added in quadrature to get the total unfolding uncertainty which increases from about 1% at low  $H_{T,2}/2$  up to 2% at the high  $H_{T,2}/2$  ends of the cross-sections for both  $n_j \geq 2$  and  $n_j \geq 3$  events. This uncertainty account for about less than 1% for  $R_{32}$ .

#### 5.6.4 Luminosity Measurement Uncertainty

As discussed in Sec. 3.2, the luminosity delivered to CMS detector by LHC in the proton-proton collisions in the year of 2012 is measured by using the silicon pixel cluster counting method [29]. The uncertainty related to the integrated luminosity measurement is estimated to be 2.5% (syst.) and 0.5% (stat.). This uncertainty propagates directly to any absolute cross-section measurement. Hence, a total systematic uncertainty of 2.6% is considered across all the  $H_{T,2}/2$  bins. At low  $H_{T,2}/2$ ,

it is similar in size as the one from JEC. This uncertainty cancels completely for  $R_{32}$ .

### 5.6.5 Residual Uncertainty

The small trigger and jet identification inefficiencies account for smaller than 1% uncertainties on the cross-section measurements [65, 77]. Hence, an uncorrelated residual uncertainty of 1% is assumed across all  $H_{T,2}/2$  bins for both  $n_j \geq 2$  and  $n_j \geq 3$  events cross-sections whereas for  $R_{32}$ , it gets cancel completely.

### 5.6.6 Total Experimental Uncertainty

After calculating the uncertainties from all the above mentioned sources, the total experimental uncertainty on measurement of cross-sections as well as cross-section ratio  $R_{32}$ , is obtained by adding in quadrature the uncertainties from individual sources. Figure 5.21 shows the experimental uncertainties, from different sources as well as the total uncertainty, affecting the measurement of  $n_j \geq 2$  (top left) and  $n_j \geq 3$  events cross-sections (top right) and cross-section ratio  $R_{32}$  (bottom). The error bars represent the statistical uncertainty obtained after unfolding. The systematic uncertainties due to jet energy corrections (JEC by blue line), luminosity (red dashed line), unfolding (green dashed line) and residual effects (light purple line) are also presented. The uncertainties due to luminosity and residual effects cancel completely in  $R_{32}$ . The total uncertainty (black dashed line) on the measurements is asymmetric in nature and dominated by the uncertainty due to the jet energy corrections (JEC) at lower  $H_{T,2}/2$  values and by statistical uncertainty at higher  $H_{T,2}/2$  values.

The experimental uncertainties from each source as well as total uncertainty are also quoted in Table 5.7. The values of uncertainties (in %) from each source as well as total uncertainty, for each  $H_{T,2}/2$  bin, are tabulated in Tables A.2, A.3

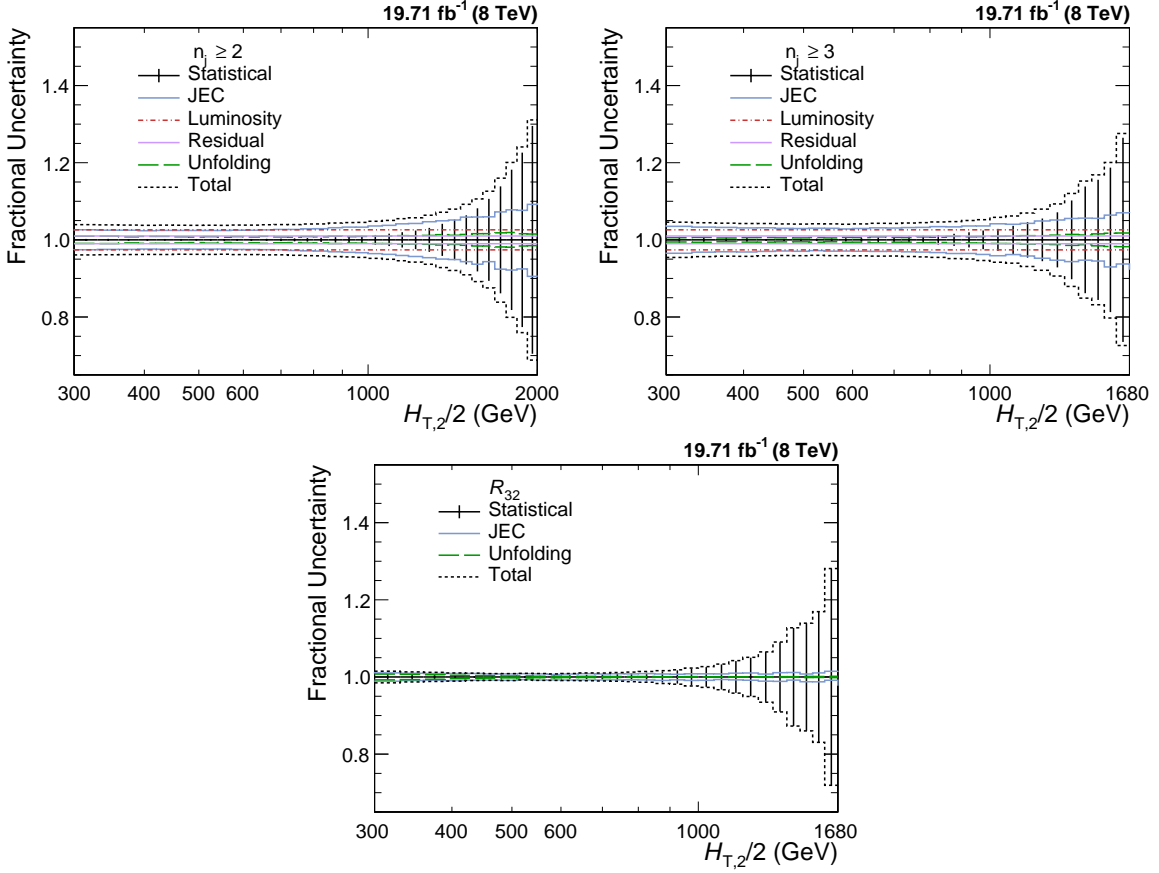


Figure 5.21: Experimental uncertainties from different sources affecting the measurement of cross-sections for inclusive 2-jet (top left) and 3-jet events (top right) and cross-section ratio  $R_{32}$  (bottom). The error bars represent the statistical uncertainty after unfolding. The systematic uncertainties due to jet energy corrections (JEC by blue line), luminosity (red dashed line), unfolding (green dashed line) and residual effects (light purple line) are also presented. The uncertainties due to luminosity and residual effects cancel completely in  $R_{32}$ . The total uncertainty (black dashed line) is the quadrature sum of the individual sources of uncertainty.

and A.4 for  $n_j \geq 2$  and  $n_j \geq 3$  events cross-sections and cross-section ratio  $R_{32}$ , respectively.

The complete data analysis of the differential inclusive 2-jet and 3-jet events cross-sections as well as their ratio  $R_{32}$  has been presented as a function of  $H_{T,2}/2$ . The measured spectrums after correcting for detector effects through the unfolding procedure, are compared with the next-to-leading order (NLO) pQCD calculations in the next chapter.

Table 5.7: Overview of all experimental uncertainties affecting the measurement of cross-sections for inclusive 2-jet (left) and 3-jet events (middle) and cross-section ratio  $R_{32}$  (right). The uncertainties due to luminosity and residual effects cancel completely in  $R_{32}$ . The total uncertainty is the quadrature sum of the individual sources of uncertainty.

Uncertainty Source	Inclusive 2-jet	Inclusive 3-jet	$R_{32}$
Statistical	< 1 to 30%	< 1 to 27%	< 1 to 28%
Jet energy corrections (JEC)	3 to 10%	3 to 8%	1 to 2%
Unfolding	1 to 2%	1 to 2%	< 1%
Luminosity	2.6%	2.6%	cancels
Residual	1%	1%	cancels
Total	4 to 32%	4 to 28%	1 to 28%

# Chapter 6

## Theoretical Calculations

In an experiment, the measurements are validated by doing the comparison with the perturbative QCD (pQCD) theoretical calculations. The lowest order (LO) calculations describe well the shapes of the measured distributions but not the normalization due to the dependence on the unphysical renormalization ( $\mu_r$ ) and factorization ( $\mu_f$ ) scales. The next-to-leading order calculations (NLO) improves the precision by reducing the dependence on  $\mu_r$  and  $\mu_f$  scales and become an essential feature in the determination of fundamental parameters such as  $\alpha_S$  and the parton distribution functions (PDF). This chapter describes the next-to-leading order pQCD calculations used for comparison with the measurements. NLO pQCD calculations need to be corrected for the multiparton interactions (MPI) and hadronization effects by applying non-perturbative (NP) corrections and also for the electroweak interactions (EW).

### 6.1 Fixed Order NLO Calculations

The predictions of the inclusive differential jet event cross-section at NLO accuracy in pQCD are computed with the NLOJET++ program version 4.1.3 [49, 50]. The results are provided within the framework of FASTNLO version 2.3 [51, 52]. The

PDFs are accessed through the LHAPDF6 library [53, 54]. The FASTNLO is preferred over the direct calculation with NLOJET++ because with FASTNLO the calculations of the cross-sections can be repeated several times with different PDFs and scale choices required for calculating the PDF and scale uncertainties. Here the factorization and renormalization scales are chosen equal to  $H_{T,2}/2$ , i.e.  $\mu_f = \mu_r = H_{T,2}/2$ .

In the current study, different PDF sets available for a series of different assumptions on the strong coupling constant at the scale of the  $Z$  boson mass  $\alpha_s(M_Z)$  are used for NLO calculations. Table 6.1 summarizes the already existing PDF sets in LHC Run 1 (upper rows) and the newer PDF sets for Run 2 (lower rows). The different columns list the number of flavours  $N_f$ , the assumed masses  $M_t$  and  $M_Z$  of the top quark and the  $Z$  boson, respectively, the default values of  $\alpha_s(M_Z)$ , and the range in  $\alpha_s(M_Z)$  variation available for fits for different PDF sets. All sets uses a variable-flavour number scheme with at most five or six flavours apart from the ABM11 PDFs, which employ a fixed-flavour number scheme with  $N_F = 5$ . Out of these eight PDF sets the following three are not considered further because of the below mentioned reasons :

- At NLO, predictions based on ABM11 do not describe LHC jet data at small jet rapidity [78–81].
- The HERAPDF2.0 set exclusively fits HERA DIS data with only weak constraints on the gluon PDF.
- The range in values available for  $\alpha_s(M_Z)$  is too limited for the NNPDF3.0 set.

Mainly CT10 PDF set is considered for comparison between data and theory predictions as well as for calculating theoretical uncertainties.

Table 6.1: NLO PDF sets are available via LHAPDF6 with various assumptions on the value of  $\alpha_s(M_Z)$ . The upper rows list the already existing sets in LHC Run 1 and newer ones for Run 2 are listed in lower rows, along with the corresponding number of flavours  $N_f$ , the assumed masses  $M_t$  and  $M_Z$  of the top quark and the  $Z$  boson, respectively, the default values of  $\alpha_s(M_Z)$ , and the range in  $\alpha_s(M_Z)$  variation available for fits.

Base set	$N_F$	$M_t$ ( GeV)	$M_Z$ ( GeV)	$\alpha_s(M_Z)$	$\alpha_s(M_Z)$ range
ABM11 [82]	5	180	91.174	0.1180	0.110 - 0.130
CT10 [83]	$\leq 5$	172	91.188	0.1180	0.112 - 0.127
MSTW2008 [84, 85]	$\leq 5$	$10^{10}$	91.1876	0.1202	0.110 - 0.130
NNPDF2.3 [86]	$\leq 6$	175	91.1876	0.1180	0.114–0.124
CT14 [87]	$\leq 5$	172	91.1876	0.1180	0.111–0.123
HERAPDF2.0 [88]	$\leq 5$	173	91.1876	0.1180	0.110–0.130
MMHT2014 [89]	$\leq 5$	$10^{10}$	91.1876	0.1200	0.108–0.128
NNPDF3.0 [90]	$\leq 5$	173	91.2	0.1180	0.115–0.121

### 6.1.1 NLO Correction Factors

The differences between LO predictions and NLO predictions give the effect of the higher-order contributions to the pQCD predictions. These are described by a NLO correction factor, k-factor, which is derived as the ratio of cross-sections at NLO accuracy to that at LO i.e.

$$\text{k-factor} = \frac{\sigma_{\text{NLO}}}{\sigma_{\text{LO}}} \quad (6.1)$$

The impact of the higher-order corrections is determined by the size of k-factor. The small size of k-factor indicates that the cross-section predictions are precisely described at the LO whereas the larger size hints the contributions from NLO. Figure 6.1 shows the k-factors of the NLOJET++ calculations, for inclusive 2-jet and 3-jet event cross-sections and their ratio  $R_{32}$ , using five different PDF sets. k-factor for  $R_{32}$  is obtained by taking the ratio of k-factors for inclusive 3-jet event cross-sections to that of inclusive 2-jet. The k-factors are similar for all the PDF sets in the lower region, but the differences increase in regions with larger  $H_{T,2}/2$ . It is observed that for inclusive 3-jet event cross-sections, k-factor jumps at lowest

$H_{T,2}/2$ . This is because some jet configurations are kinematically forbidden near the  $p_T$  cut bin i.e. 150 GeV. Since the first few bins in  $H_{T,2}/2$  (below 225 GeV) still suffer from these kinematical effects, the minimum value of  $H_{T,2}/2$  studied is 300 GeV.

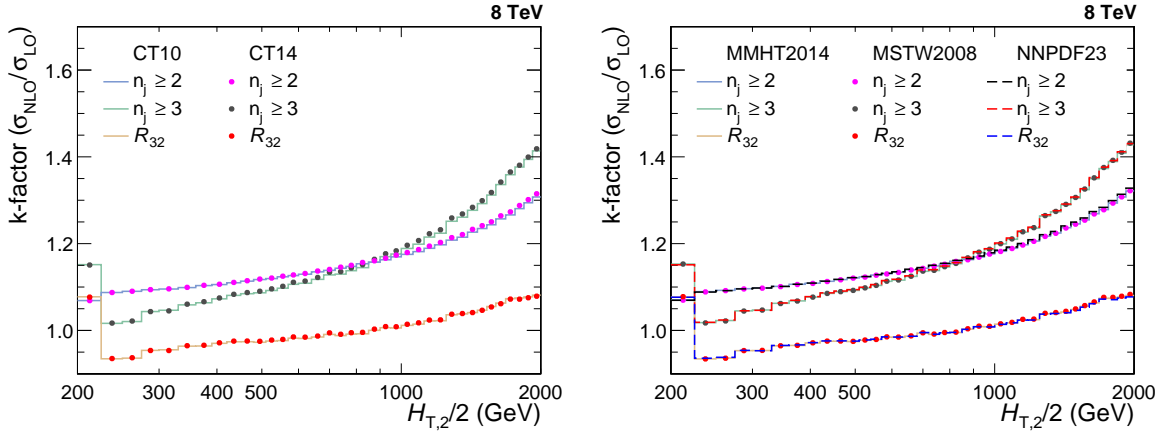


Figure 6.1: The k-factors of the NLOJET++ calculations, for inclusive 2-jet and 3-jet event cross-sections and their ratio  $R_{32}$ , using five different PDF sets.

### 6.1.2 Non-Perturbative Corrections

The fixed-order pQCD NLO calculations predict the parton-level cross-section but lacks accuracy due to several effects. The partons which are emitted close to each other in phase space are not handled well in lower order perturbation theories and hence requires a parton shower (PS) correction. The scattering phenomena between partons within a colliding proton, other than the hard scattering, give rise to multi-parton interactions (MPI). The partons of the hard scattering forms colorless bound states called hadrons through a process of hadronization (HAD). The MPI and hadronization cannot be modelled well within the perturbative framework. Since the fixed-order NLO calculations do not include these additional soft QCD effects, these calculations cannot be compared directly to unfolded data. So the corrections for non-perturbative effects (NP) should be taken into account in NLO calculations. The ratio of cross-section predicted with a nominal event generation interfaced to

the simulation of UE contributions and to the one without hadronization and MPI effects gives the NP correction factors which are defined as :

$$C^{\text{NP}} = \frac{\sigma^{\text{PS+HAD+MPI}}}{\sigma^{\text{PS}}} \quad (6.2)$$

In the current study, the NP effects are estimated by using samples obtained from various MC event generators with a simulation of parton shower and underlying-event (UE) contributions. The leading order (LO), HERWIG++ with the default tune of version 2.3 and PYTHIA6 with tune Z2\*, and the NLO POWHEG MC event generators are considered. The matrix-element calculation is performed with POWHEG interfaced to PYTHIA8 with tune CUETS1 for the UE simulation. The ratio, defined in Eq. 6.2, is obtained for each MC generator and is fitted by a power-law function defined in Eq. 6.3. Since this ratio obtained from different MC generators have large differences, so the average of the envelope, which covers all the differences, is taken as the correction factor which is then applied as bin-by-bin multiplicative factor to the parton-level NLO cross-section. The half of the envelope it is taken as the uncertainty on the NP correction factor.

$$f(H_{\text{T},2}/2) = a \cdot (H_{\text{T},2}/2)^b + c \quad (6.3)$$

The NP correction factors,  $C_{3\text{-jet}}^{\text{NP}}$  and  $C_{2\text{-jet}}^{\text{NP}}$  are calculated for  $n_j \geq 2$  and  $n_j \geq 3$  event cross-sections respectively and then their ratio gives the correction factor for  $R_{32}$ . The correction factors are shown in Fig. 6.2 for the inclusive 2-jet (top left) and 3-jet event cross-sections (top right), and for ratio  $R_{32}$  (bottom). At  $H_{\text{T},2}/2 \sim 300$  GeV, the NP corrections amount to  $\sim 4\text{-}5\%$  for inclusive 2-jet and 3-jet event cross-sections and  $\sim 1\%$  for  $R_{32}$ , and decrease rapidly for increasing  $H_{\text{T},2}/2$ . On comparing the NP correction factors of  $R_{32}$  with that for individual cross-sections, it has been observed that the non-perturbative effects get reduced in  $R_{32}$ .

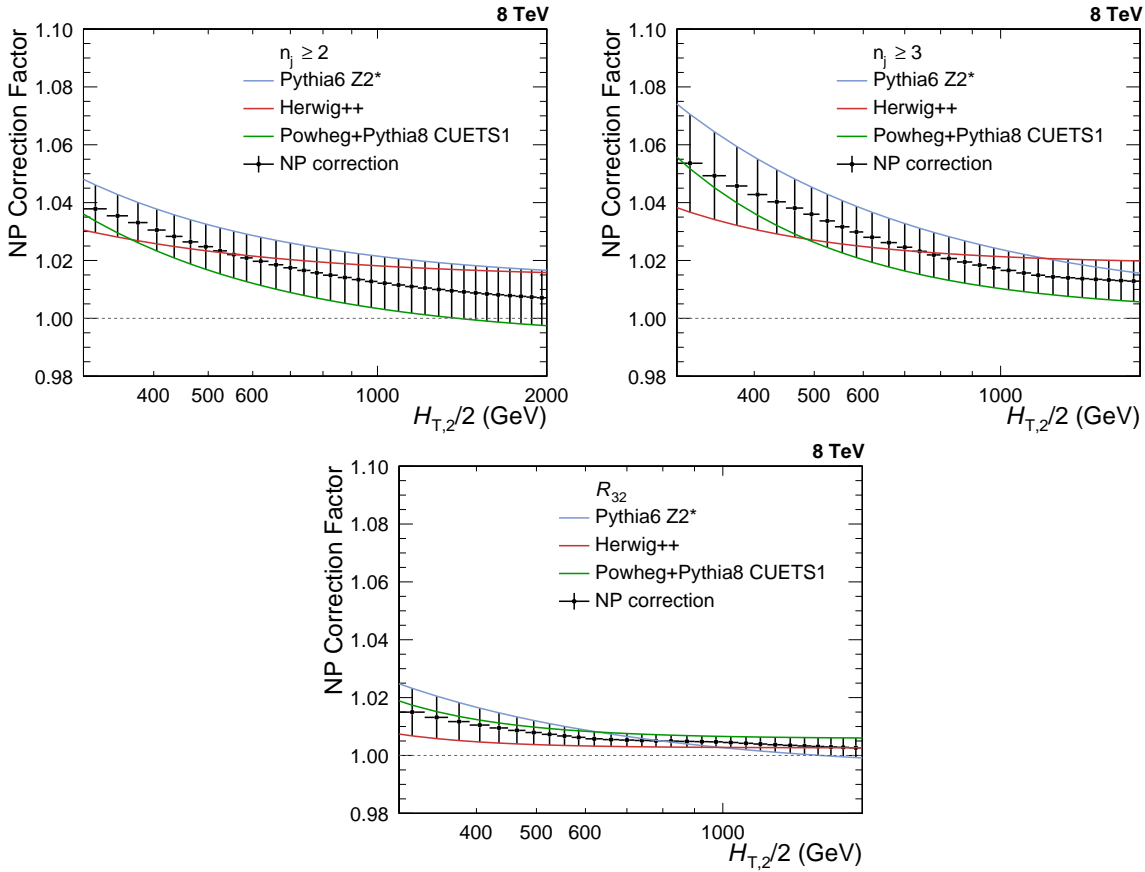


Figure 6.2: The nonperturbative (NP) corrections are presented as a function of  $H_{T,2}/2$  for inclusive 2-jet (top left) and 3-jet (top right) event cross-sections, as well as their ratio  $R_{32}$ . These corrections are calculated from the leading order HERWIG++ with the default tune of version 2.3 (red line) and PYTHIA6 with tune Z2\* (blue line); and the next-to-leading order POWHEG interfaced to PYTHIA8 with tune CUETS1 (green line) Monte Carlo event generators. The black solid circles give the average NP correction factor along with the uncertainty shown by the error bars.

### 6.1.3 Electroweak Corrections

In LHC, the centre-of-mass energy of proton-proton collisions is well beyond the electroweak (EW) scale  $\sim \mathcal{O}(100 \text{ GeV})$ . At such a high energy, the impact of higher order EW corrections is much more with respect to QCD effects [91] and affect jet cross-sections at large  $H_{T,2}/2$ . The quark-quark scattering processes involving virtual exchanges of massive  $W$  and  $Z$  bosons contribute to electroweak (EW) corrections. The fixed-order QCD calculations do not include EW corrections and hence the NLO theory calculations are corrected for EW effects. The EW corrections have

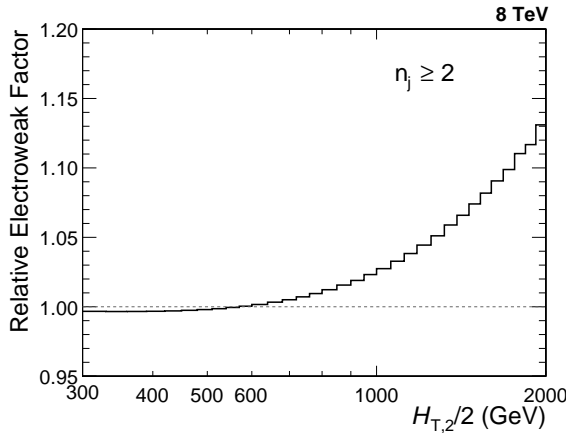


Figure 6.3: The electroweak (EW) corrections [92] in the phase space of the measurement are shown as a function of  $H_{T,2}/2$  for inclusive 2-jet event cross-sections. These corrections are applied as a bin-by-bin correction factor to the fixed-order calculation of NLOJET++ as well as the MC predictions of MADGRAPH5+PYTHIA6. The EW correction factor increases up to 13% at high ends of  $H_{T,2}/2$  and significantly improves the agreement between data and prediction.

been calculated for inclusive 1-jet and 2-jet case, in Ref. [92]. The EW correction factors in the phase space of the measurement are shown as a function of  $H_{T,2}/2$  in Fig. 6.3 for inclusive 2-jet event cross-sections. These correction factor increases up to 13% at high ends of  $H_{T,2}/2$  which are applied as a bin-by-bin correction factor to the fixed-order NLOJET++ calculations. To see the effects of EW corrections, a ratio of data to theory predictions obtained using CT10-NLO PDF set and corrected with NP effects without including EW corrections (left) and including EW corrections (right) is plotted for inclusive 2-jet event cross-sections in Fig. 6.4. On comparing both the figures, it is observed that the EW corrections significantly improve the agreement between data and prediction in the high  $H_{T,2}/2$  region. EW corrections are not available yet for inclusive 3-jet production and hence not applied for inclusive 3-jet event cross-sections. The guess from theory side is that EW for inclusive 2-jet and 3-jet will be similar, so for  $R_{32}$ , it is assumed to be equal to the factor of 1. Since the EW effects are not taken care of in MC simulations so these corrections are applied to MC predictions also.

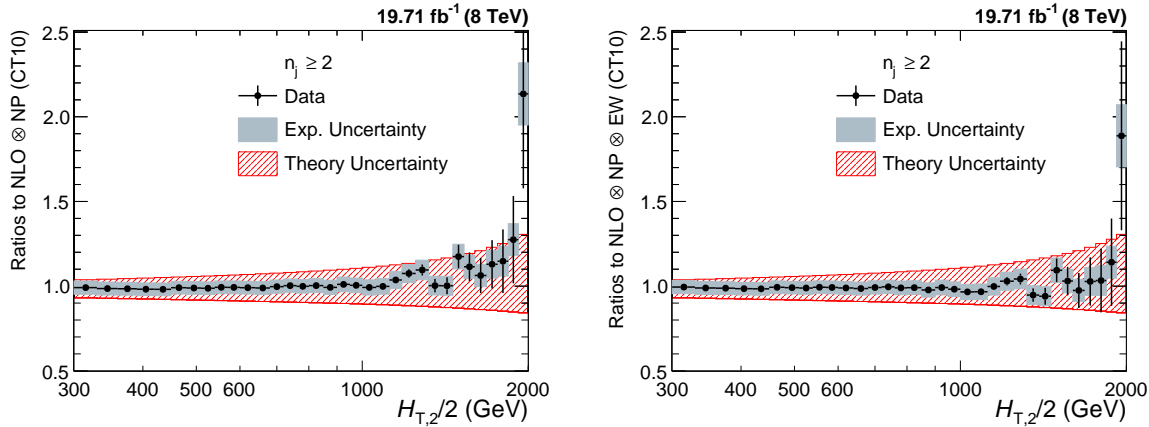


Figure 6.4: Ratio of data over theory obtained using the CT10-NLO PDF set and corrected with non-perturbative effects (NP) without including electroweak (EW) corrections (left) and including EW corrections (right) is shown for inclusive 2-jet event cross-sections. The error bars represents the statistical uncertainty of the data and the shaded rectangles represents the total experimental systematic uncertainty. The shaded band around unity indicate the total uncertainty of the theory. The EW corrections significantly improve the agreement between data and prediction in the high  $H_{T,2}/2$  region.

## 6.2 Theoretical Uncertainties

The measurements are not only sensitive to experimental uncertainties but also to the theoretical uncertainties. The renormalization and factorization scale variations, PDF uncertainties and the non-perturbative corrections contribute to theoretical uncertainties which are described below :

### 6.2.1 Scale Uncertainty

In perturbative QCD calculations of cross-sections, one has to choose a renormalization ( $\mu_r$ ) and factorization ( $\mu_f$ ) scale. The dependence on scales is negligible if these calculations are performed for all orders of the perturbative series. But the perturbative series is truncated at NLO, so there is a scale dependence of the measurement which is covered by systematic uncertainty known as scale uncertainty. The scale uncertainty is evaluated with the conventional recipe of varying the default scale  $H_{T,2}/2$  chosen for  $\mu_r$  and  $\mu_f$  independently in the following six combinations:  $(\mu_r/H_{T,2}/2, \mu_f/H_{T,2}/2) = (1/2, 1/2), (1/2, 1), (1, 1/2), (1, 2), (2, 1)$  and  $(2, 2)$ . The

maximal upwards and downwards deviations in cross-section from the central prediction give the scale uncertainty. To calculate the scale uncertainty for cross-section ratio  $R_{32}$ , first  $R_{32}$  is obtained for each above mentioned scale choice and then its difference from central  $R_{32}$  is taken. The scale uncertainty calculated using CT10-NLO PDF set ranges from 5% to 13% and 11% to 17% for inclusive 2-jet and 3-jet events cross-sections respectively, and from 6% to 8% for  $R_{32}$ .

### 6.2.2 PDF Uncertainty

The calculation of jet cross-sections in proton-proton collisions relies upon the knowledge of PDFs. These PDF sets are determined by global fits to all the available deep inelastic scattering (DIS) and related hard scattering data from different experiments. The various sources affect the PDFs such as theory model, input parameters like the strong coupling constant  $\alpha_S$ , the quark masses and the statistical and systematic uncertainty sources of the data included in the PDF fit. These sources contribute to PDF uncertainty which is evaluated according to the prescriptions given for each PDF set. The CT10-NLO PDF set [83, 93] employ the eigenvector method to evaluate the PDF uncertainties. The CT10-PDF set consists of  $N_{\text{ev}} = 26$  eigenvectors with two PDF members per eigenvector  $k$ , which are varied upwards and downwards to generate a set of eigenvector pairs. The asymmetric uncertainties,  $\Delta X^+$  and  $\Delta X^-$ , of a quantity  $X$  are given by Eq. 6.4 where  $X_0$  is the central prediction,  $X_k^+$  and  $X_k^-$  are the predictions using the upwards and downwards variation of each eigenvector  $k$ .

$$\Delta X^+ = \sqrt{\sum_{k=1}^{N_{\text{ev}}} [\max(X_k^+ - X^0, X_k^- - X^0, 0)]^2} \quad (6.4)$$

$$\Delta X^- = \sqrt{\sum_{k=1}^{N_{\text{ev}}} [\min(X_k^+ - X^0, X_k^- - X^0, 0)]^2}$$

The symmetric uncertainty ( $\Delta X^\pm$ ) is given by half the difference of the upwards and downwards variations :

$$\Delta X^\pm = \sqrt{\sum_{k=1}^{N_{\text{ev}}} \left[ \frac{X_k^+ - X_k^-}{2} \right]^2} \quad (6.5)$$

The CT10-NLO PDF set uncertainties are downscaled by a factor of 1.64 in order to have the uncertainties at the 68.3% confidence level  $\text{CL}(1\sigma)$  instead of 90%  $\text{CL}(2\sigma)$  such that to have a uniform treatment with respect to other PDF sets. The PDF uncertainty as derived with the CT10-NLO PDF set is the dominant source of uncertainty and ranges from 3% to 30% for inclusive 2-jet and from 4% to 32% for 3-jet cross-sections. For  $R_{32}$ , the ratio of predictions for inclusive 3-jet to that of 2-jet is taken for each eigen vector with upwards and downwards variations separately and then PDF uncertainty is calculated as done for individual cross-sections. The PDF uncertainty ranges and from 2% to 10% for cross-section ratio  $R_{32}$ .

### 6.2.3 Non-perturbative Uncertainty

As discussed in [6.1.2](#), the differences in the non-perturbative (NP) corrections calculated from various Monte Carlo event generators introduce the NP uncertainty which is of the order of 1% and 1 to 2% for inclusive 2-jet and 3-jet event cross-sections respectively, and < 1% for cross-section ratio  $R_{32}$ .

### 6.2.4 Total Theoretical Uncertainty

The total systematic theoretical uncertainties are obtained as the quadratic sum of the scale, PDF and NP uncertainties. Figure [6.5](#) presents the systematic theoretical uncertainties affecting the cross-section measurement for inclusive 2-jet (top left) and 3-jet events (top right) and the cross-section ratio  $R_{32}$  (bottom), using CT10-

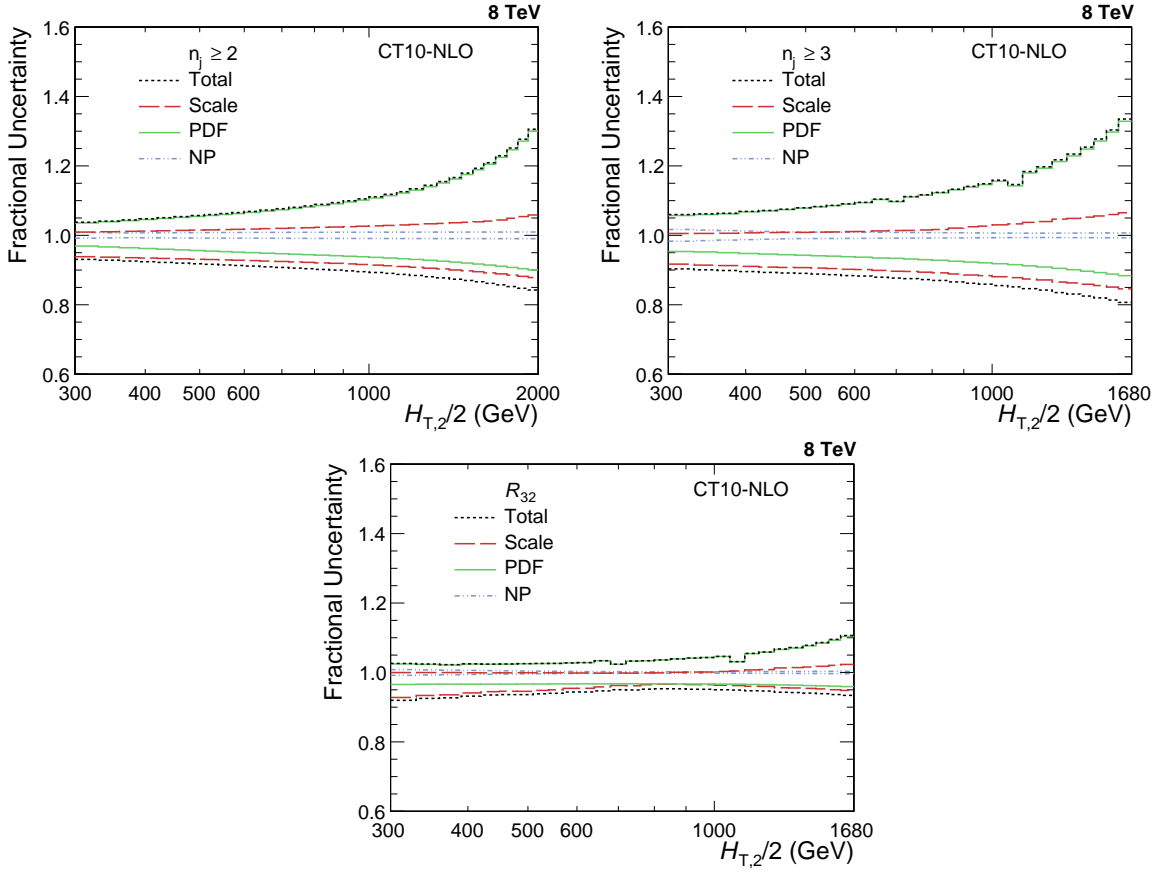


Figure 6.5: The systematic theoretical uncertainties affecting the cross-section measurement for inclusive 2-jet (top left) and 3-jet events (top right) and their ratio  $R_{32}$  (bottom). The scale (red dashed line), PDF (green line) and NP (blue dashed line) uncertainties as well as total uncertainty (black dashed line) obtained using CT10-NLO PDF set are shown. The total theoretical uncertainty is asymmetric and is dominated by PDF uncertainty.

NLO PDF set. The scale (red dashed line), PDF (green line) and NP (blue dashed line) uncertainties as well as total theoretical uncertainty (black dashed line) are shown. The total theoretical uncertainty is asymmetric and is dominated by PDF uncertainty which grows in magnitude with increasing value of  $H_{T,2}/2$ . Table 6.2 quotes the values of the theoretical uncertainty from each source as well as total uncertainty affecting the measurements. The bin-wise values of uncertainties (in %) from each source as well as total uncertainty are shown in Tables A.5, A.6 and A.7 for  $n_j \geq 2$  and  $n_j \geq 3$  event cross-sections and cross-section ratio  $R_{32}$ , respectively. The computation of the NLO predictions with NLOJET++ is also

subject to statistical fluctuations from the complex numerical integrations. For the inclusive 2-jet event cross-sections this uncertainty is smaller than about a per mille, while for the inclusive 3-jet event cross-section it amounts to 1-9 per mille. Hence the statistical uncertainty is not considered in the total theoretical uncertainty. The small dips at  $\sim 700$  and  $1000$  GeV in the PDF uncertainty for inclusive 3-jet events cross-sections and cross-section ratio  $R_{32}$  is a feature of the CT10-NLO PDF set.

Table 6.2: Overview of all systematic theoretical uncertainties, obtained using CT10-NLO PDF set, affecting the measurement of cross-sections for inclusive 2-jet (left) and 3-jet events (middle) and cross-section ratio  $R_{32}$  (right).

Uncertainty Source	Inclusive 2-jet	Inclusive 3-jet	$R_{32}$
Scale	5 to 13%	11 to 17%	6 to 8%
PDF	3 to 30%	4 to 32%	2 to 10%
Non-perturbative (NP)	1%	1 to 2%	< 1%
Total	3 to 30%	5 to 34%	3 to 11%

## 6.3 Comparison of Theory to Data

After correcting the measurement for detector effects as well as NLO pQCD calculations for non-perturbative (NP) and electroweak (EW) effects, it is now feasible to compare the measured cross-sections with the theory predictions. Figure 6.6 shows the measured differential inclusive 2-jet and 3-jet event cross-sections as a function of  $H_{T,2}/2$  after unfolding for detector effects. On the left, the measurements (points) are compared to the NLOJET++ predictions using the CT10-NLO PDF set (line), corrected for NP effects and in addition for EW effects in the 2-jet case. On the right, the comparison is made to the predictions from MADGRAPH5+PYTHIA6 (MG+P6) with tune Z2\* (line), corrected for EW effects in the 2-jet case. The error bars give the total experimental uncertainty, given by the quadrature sum of the statistical and systematic uncertainties. On a logarithmic scale, the data are in well agreement with the NLO predictions over the whole range of  $H_{T,2}/2$  from 300 GeV up to 2000

(2-jet) and 1680 GeV (3-jet) respectively.

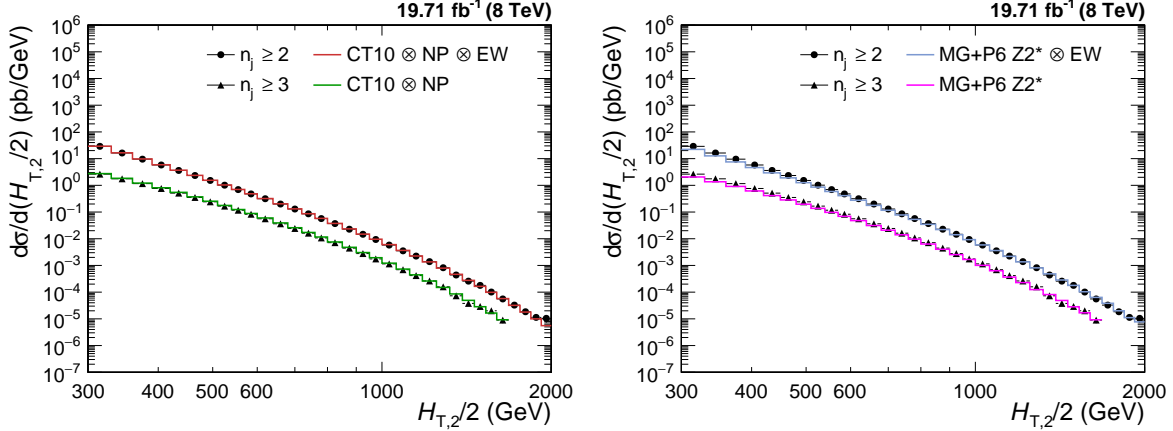


Figure 6.6: Comparison of the measured differential inclusive 2-jet and 3-jet event cross-sections as a function of  $H_{T,2}/2$  to theoretical predictions. On the left, the data (points) are shown together with NLO JET++ predictions (line) using the CT10-NLO PDF set, corrected for non-perturbative (NP) and electroweak (EW) effects (2-jet) or only NP effects (3-jet). On the (right), the data (points) are compared to predictions from MADGRAPH5+PYTHIA6 (MG+P6) with tune Z2 $^{*}$  (line), corrected for EW effects in the 2-jet case. The error bars give the total experimental uncertainty, given by the quadratic sum of the statistical and systematic uncertainties.

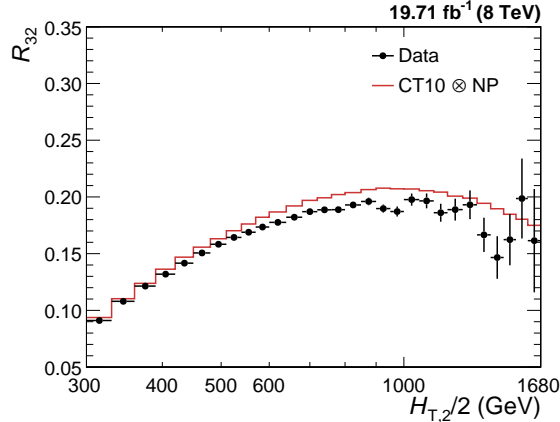


Figure 6.7: Cross-section ratio  $R_{32}$  as a function of  $H_{T,2}/2$  calculated from data (solid circles) in comparison to that from NLO pQCD predictions obtained using the CT10-NLO PDF set corrected with non-perturbative (NP) corrections (line). The error bars correspond to the total experimental uncertainty derived as quadratic sum from all uncertainty sources.

Figure 6.7 shows the cross-section ratio  $R_{32}$  obtained from unfolded data (solid circles) in comparison to that from NLO pQCD predictions obtained using the CT10-NLO PDF set corrected with NP corrections (line). The error bars here

represents the total experimental uncertainty derived as quadratic sum from all uncertainty sources. The deviations of measured  $R_{32}$  from the theoretical predicted value can be explained by the electroweak effects which are not considered yet because of their unavailability for inclusive 3-jet event cross-sections.

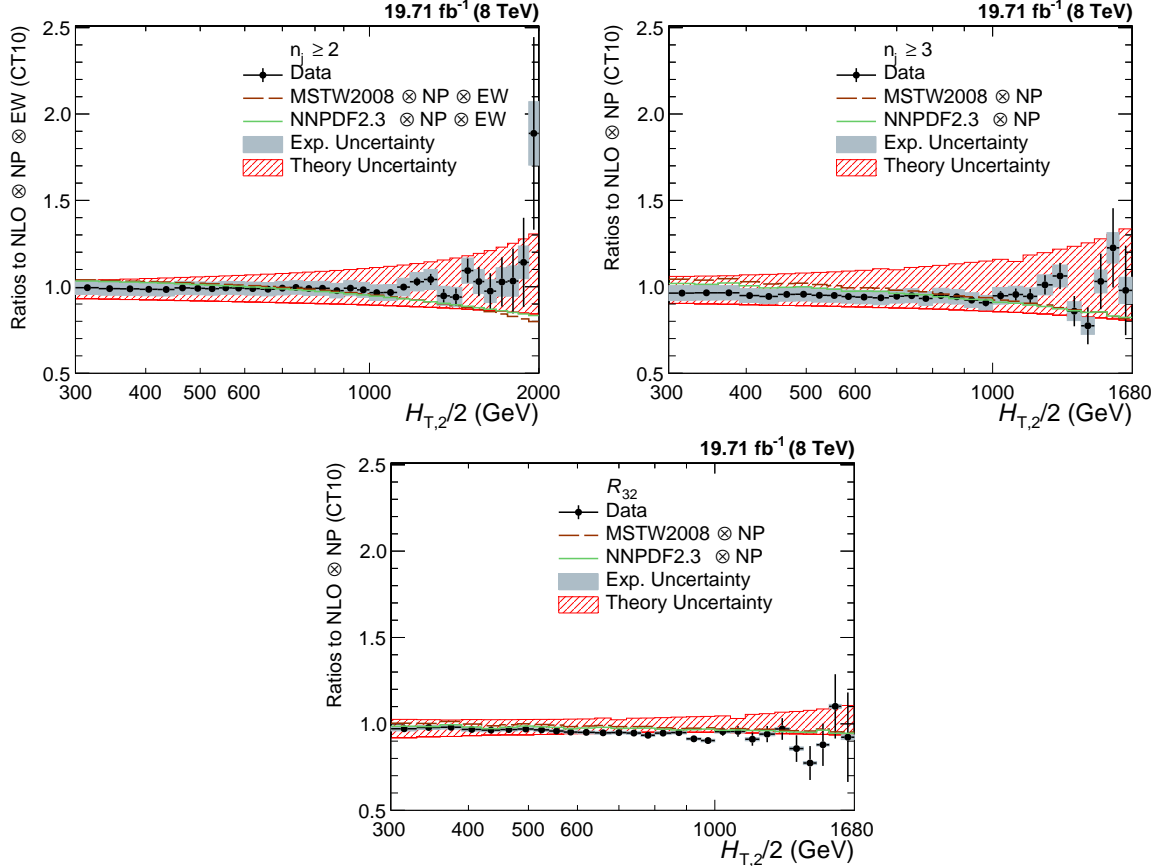


Figure 6.8: Ratio of data over theory using the CT10-NLO PDF set for inclusive 2-jet (top left) and 3-jet event cross-sections (top right) and their ratio  $R_{32}$  (bottom). The theory predictions are corrected for non-perturbative effects (NP) and also for electroweak effects (EW) for inclusive 2-jet only. For comparison predictions employing two other PDF sets, MSTW2008 and NNPDF2.3, are also shown. The error bars represents the statistical uncertainty of the data and the shaded rectangles represents the total experimental systematic uncertainty. The shaded band around unity indicate the total uncertainty of the theory.

For better visibility, the ratios of data over the theory at NLO are also studied in details. In Fig. 6.8, the ratios of data over NLOJET++ predictions using the CT10-NLO PDF set are shown for inclusive 2-jet (top left) and 3-jet event cross-sections (top right) as well as their ratio  $R_{32}$  (bottom). The data are well described by the predictions within their uncertainty, which is dominated at large  $H_{T,2}/2$  by

PDF effects in the upwards and by scale variations in the downwards direction. A trend towards an increasing systematic excess of the 2-jet data with respect to theory, starting at about 1 TeV in  $H_{T,2}/2$ , is remedied by the inclusion of EWK corrections. In the 3-jet case the statistical precision of the data and the reach in  $H_{T,2}/2$  is insufficient to observe any effect. The alternative PDF sets MSTW2008 and NNPDF2.3 exhibit a small underestimation of the cross-sections at high  $H_{T,2}/2$ .

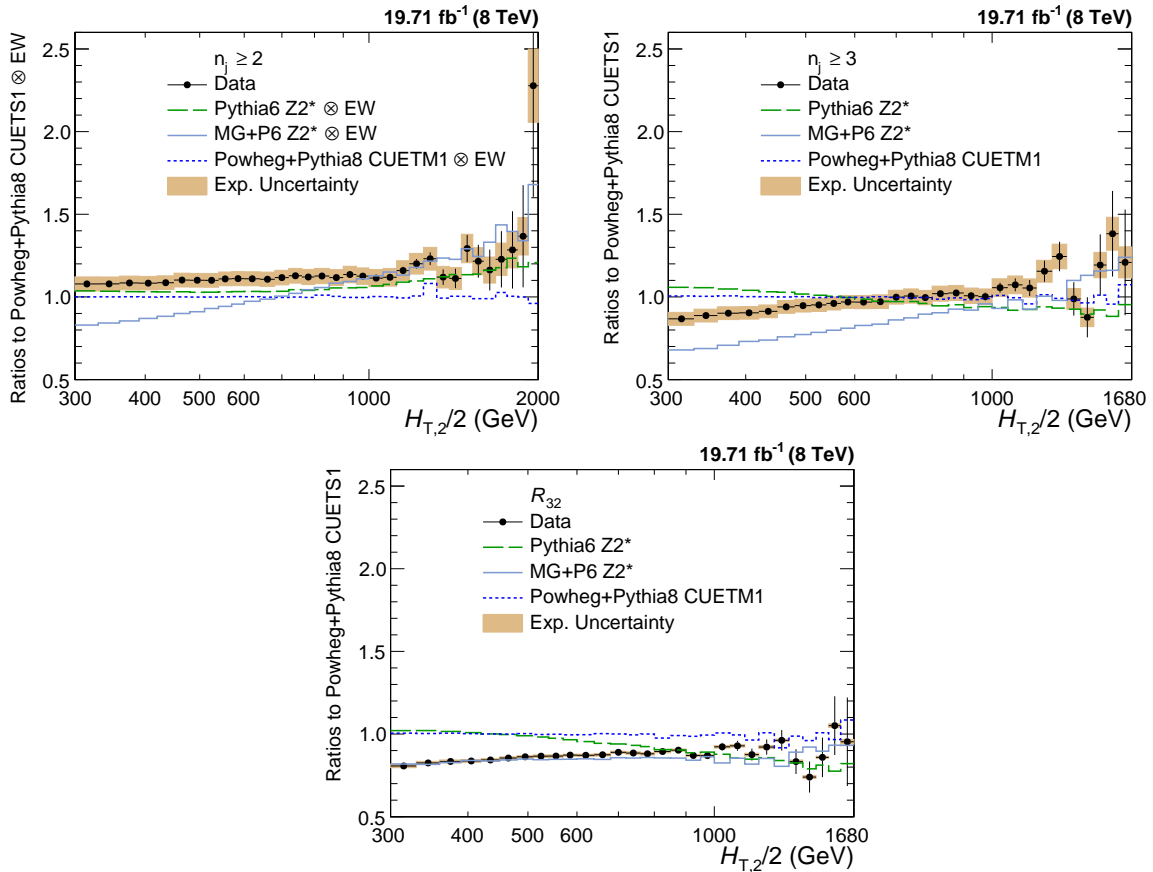


Figure 6.9: Ratio of data over the prediction from POWHEG+PYTHIA8 with tune CUETS1 are presented for inclusive 2-jet (top left) and 3-jet event cross-sections (top right) as well as their ratio  $R_{32}$  (bottom). For comparison the alternative tune CUETM1 of POWHEG+PYTHIA8, the tree-level multi-leg improved prediction by MADGRAPH5+PYTHIA6 with tune  $Z2^*$ , and the the LO MC predictions from PYTHIA6 tune  $Z2^*$  are shown as well. The error bars correspond to the statistical uncertainty of the data and the shaded rectangles to the total experimental systematic uncertainty. EW corrections have been accounted for in this comparison in the 2-jet case only.

The POWHEG framework providing a NLO dijet calculation matched to the parton showers of PYTHIA8 employed with the CUETS1 and CUETM1 tunes [39] is also

used for a comparison. The ratios of data over theory from POWHEG+PYTHIA8 with tune CUETS1 are shown for inclusive 2-jet (top left) and 3-jet event cross-sections (top right) as well as their ratio  $R_{32}$  (bottom) in Fig. 6.9. For comparison, the LO prediction from PYTHIA6 with tune Z2\*, the tree-level multi-leg improved prediction by MADGRAPH5+PYTHIA6 with tune Z2\*, and the matched NLO prediction from POWHEG+PYTHIA8 with tune CUETM1 are shown as well. EW corrections have been accounted for in this comparison in the 2-jet case only. Significant discrepancies, which are cancelled to a large extent in the ratio  $R_{32}$ , are visible in the comparison with the LO prediction from MADGRAPH5+PYTHIA6 with tune Z2\*, in particular for small  $H_{T,2}/2$ . In contrast, the employed dijet MC POWHEG+PYTHIA8 better describe the 2-jet event cross-section, but fail for the 3-jet case.

The jet measurements at hadron colliders can be used to extract the strong coupling constant  $\alpha_S$ , which is discussed in the next chapter.

# Chapter 7

## Determination of the Strong Coupling Constant

The inclusive jet production cross-section at hadron colliders mainly depends on the strong coupling constant  $\alpha_S$  for a given centre-of-mass energy. Hence the measurements of the inclusive jet cross-section and jet properties provide a direct probe to measure the strong coupling constant. The measurement of  $\alpha_S$  has been already done by various experiments such as CMS [1, 65, 80, 94, 95], ATLAS [96], D0 [97, 98], H1 [99, 100], and ZEUS [101]. In this thesis, the measurements of differential inclusive 2-jet and 3-jet event cross-sections as well as the cross-section ratio  $R_{32}$ , as a function of  $H_{\text{T},2}/2$  are used to extract the value of the strong coupling constant at the scale of the  $Z$  boson mass  $\alpha_s(M_Z)$ . The differential inclusive jet production cross-section up to at NLO is given by [102] :

$$\frac{d\sigma}{d(H_{\text{T},2}/2)} = \alpha_S^2(\mu_r) \hat{X}^{(0)}(\mu_f, H_{\text{T},2}/2) [1 + \alpha_S(\mu_r) K1(\mu_r, \mu_f, H_{\text{T},2}/2)] \quad (7.1)$$

where  $\frac{d\sigma}{d(H_{\text{T},2}/2)}$  is the differential inclusive jet production cross-section as a function of  $H_{\text{T},2}/2$ ,  $\mu_r$  and  $\mu_f$  are the renormalization and factorization scales set equal to  $H_{\text{T},2}/2$ ,  $\alpha_S^2(\mu_r) \hat{X}^{(0)}(\mu_f, H_{\text{T},2}/2)$  is the leading order

(LO) contribution to the differential inclusive jet production cross-section and  $\alpha_S^3(\mu_r)\hat{X}^{(0)}(\mu_f, H_{T,2}/2)K1(\mu_r, \mu_f, H_{T,2}/2)$  is the next-to-leading order (NLO) contribution. Equation 7.1 shows how the inclusive jet production cross-section varies with  $\alpha_s(\mu_r)$ .

## 7.1 Sensitivity of Measurements to $\alpha_s(M_Z)$

For a fixed choice of  $\mu_r$  and  $\mu_f$ , different input values of  $\alpha_s(M_Z)$  to a PDF set will lead to different theory predictions of the differential cross-section distribution. This will give an estimate of the sensitivity of the theory predictions to the varying input value of  $\alpha_s(M_Z)$ . A comparison of the measured spectrum with the theory predictions obtained using all  $\alpha_s(M_Z)$  inputs will give a hint of the input value of  $\alpha_s(M_Z)$  for which the theory distribution has the closest matching with data. In this section, the sensitivity of the inclusive differential jet event cross-sections and cross-section ratio,  $R_{32}$  to varying input values of  $\alpha_s(M_Z)$  for different PDF sets is demonstrated by plotting the ratios of data over theory predictions with central value of  $\alpha_s(M_Z)$ .

Figures 7.1, 7.2 and 7.3 present the ratio of data to the theory predictions, corrected for NP effects, for all variations in  $\alpha_s(M_Z)$  available for the PDF sets CT10, CT14, MSTW2008, MMHT2014 and NNPDF2.3 at NLO evolution order as specified in Table 6.1, for inclusive 2-jet event cross-sections, inclusive 3-jet events cross-sections and ratio  $R_{32}$  respectively. The  $\alpha_s(M_Z)$  value is varied in the range 0.112-0.127, 0.111-123, 0.110-0.130, 0.108-0.128 and 0.114-0.124 in steps of 0.001 for the CT10, CT14, MSTW2008, MMHT2014 and NNPDF2.3PDF sets, respectively. The error bars correspond to the total experimental uncertainty derived as quadratic sum from all uncertainty sources. The theory predictions are also corrected for EW effects for inclusive 2-jet events cross-section. A small slope increasing with  $H_{T,2}/2$  is visible for most PDFs in both cross-sections. This effect is largely cancelled in

the cross-section ratio.  $R_{32}$  exhibits a flat behaviour with respect to the predictions for all five PDF sets in the whole range of  $H_{T,2}/2$  up to 1680 GeV. Therefore, these data can be used to determine the strong coupling constant, although only up to 1 TeV for the cross-sections as long as electroweak corrections are not taken into account.

Moreover, the different sensitivity to  $\alpha_s(M_Z)$  caused by the leading power in  $\alpha_S$  in the expansion of the 2-jet inclusive ( $\propto \alpha_S^2$ ) and the 3-jet inclusive cross-section ( $\propto \alpha_S^3$ ), and their ratio ( $\propto \alpha_S^1$ ) is clearly visible from the spread between the calculations for the smallest and largest value of  $\alpha_s(M_Z)$  within the same PDF set when passing through Figures 7.1–7.3. This also demonstrates the potential of ratios  $R_{mn}$  with  $m-n > 1$ .

## 7.2 Determination of $\alpha_s(M_Z)$

As discussed in the previous section, the measured inclusive 2-jet and 3-jet event cross-sections and their ratio  $R_{32}$  can be used for a determination of the strong coupling constant  $\alpha_s(M_Z)$ . To extract the value of  $\alpha_s(M_Z)$ , a general fit procedure [1, 65, 95] has been followed and is described in the following section.

### 7.2.1 Fitting Procedure

The value of  $\alpha_s(M_Z)$  is determined by minimizing the chi-square ( $\chi^2$ ) between the experimental measurements and the theoretical predictions. The  $\chi^2$  is given by the following equation :

$$\chi^2 = M^T C^{-1} M \quad (7.2)$$

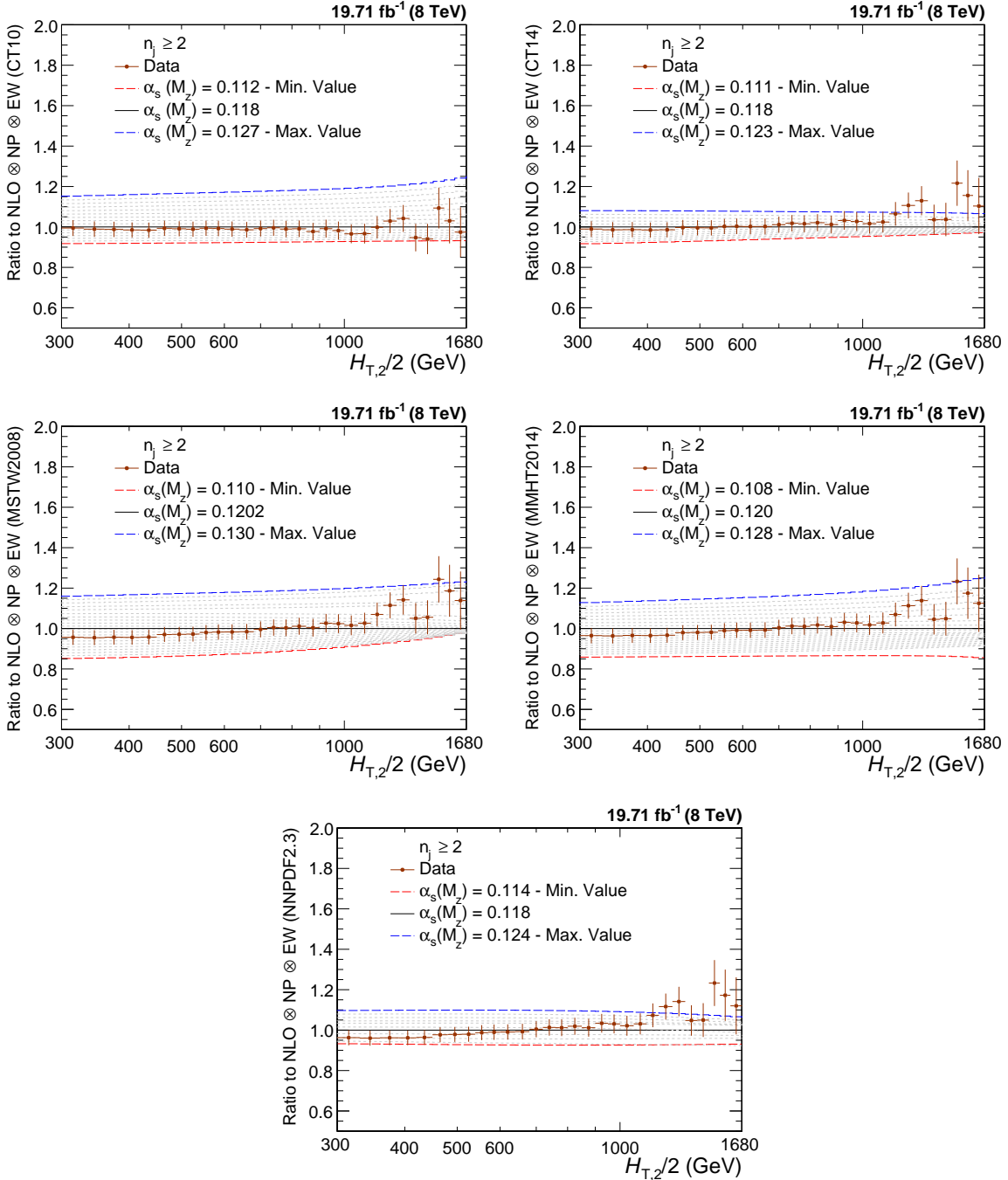


Figure 7.1: Ratio of the inclusive 2-jet differential cross-section to theory predictions using the CT10 (top left), the CT14 (top right), the MSTW2008 (middle left), the MMHT2014 (middle right) and NNPDF2.3 (bottom) NLO PDF sets for a series of values of  $\alpha_s(M_Z)$ . The  $\alpha_s(M_Z)$  value is varied in the range 0.112-0.127, 0.111-123, 0.110-0.130, 0.108-0.128 and 0.114-0.124 in steps of 0.001 for the CT10, CT14, MSTW2008, MMHT2014 and NNPDF2.3 NLO PDF sets, respectively. The error bars correspond to the total experimental uncertainty. The theory predictions are corrected for non-perturbative (NP) and electroweak (EW) effects.

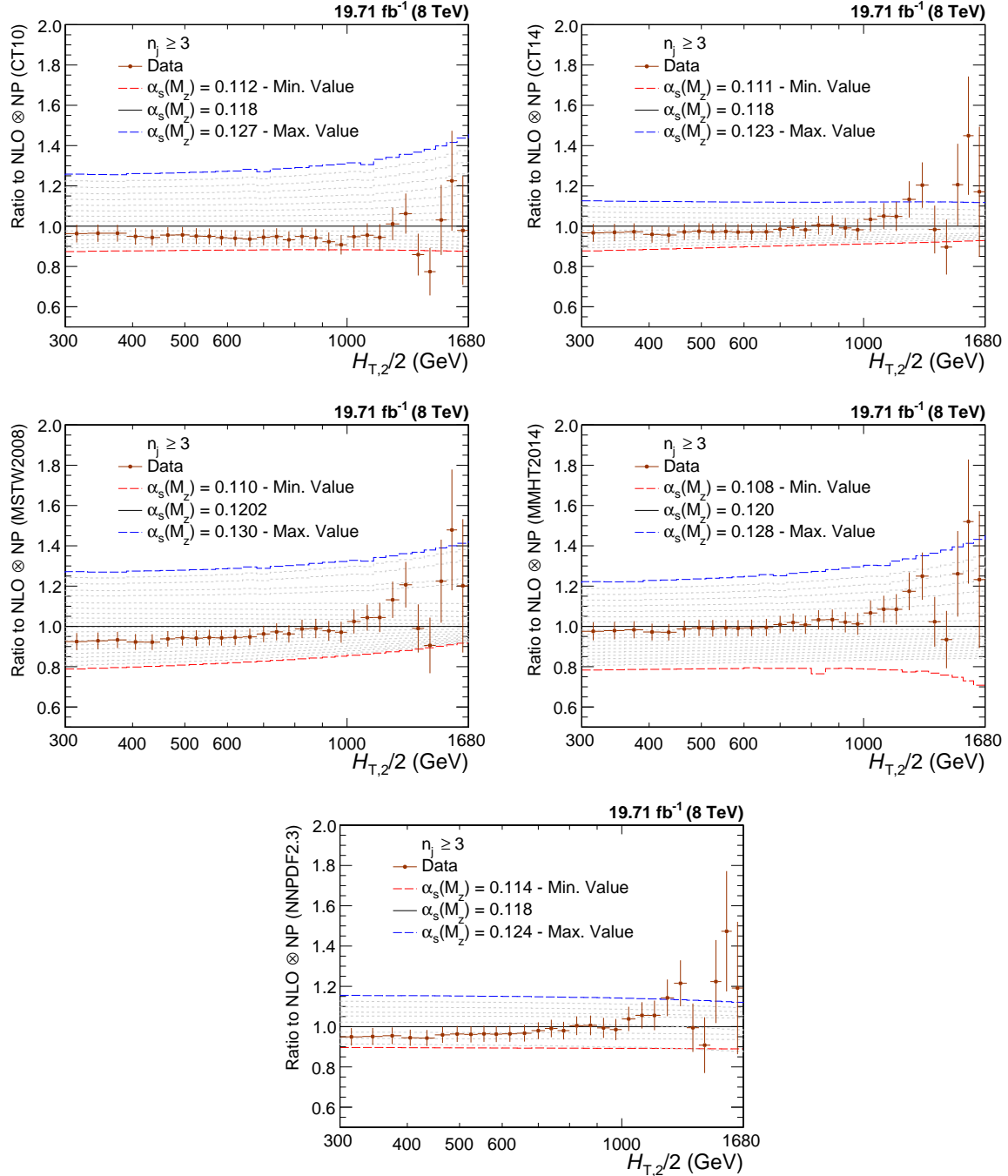


Figure 7.2: Ratio of the inclusive 3-jet differential cross-section to theory predictions using the CT10 (top left), the CT14 (top right), the MSTW2008 (middle left), the MMHT2014 (middle right) and NNPDF2.3 (bottom) NLO PDF sets for a series of values of  $\alpha_s(M_Z)$ . The  $\alpha_s(M_Z)$  value is varied in the range 0.112-0.127, 0.111-123, 0.110-0.130, 0.108-0.128 and 0.114-0.124 in steps of 0.001 for the CT10, CT14, MSTW2008, MMHT2014 and NNPDF2.3 NLO PDF sets, respectively. The error bars correspond to the total experimental uncertainty. The theory predictions are corrected for non-perturbative (NP) effects.

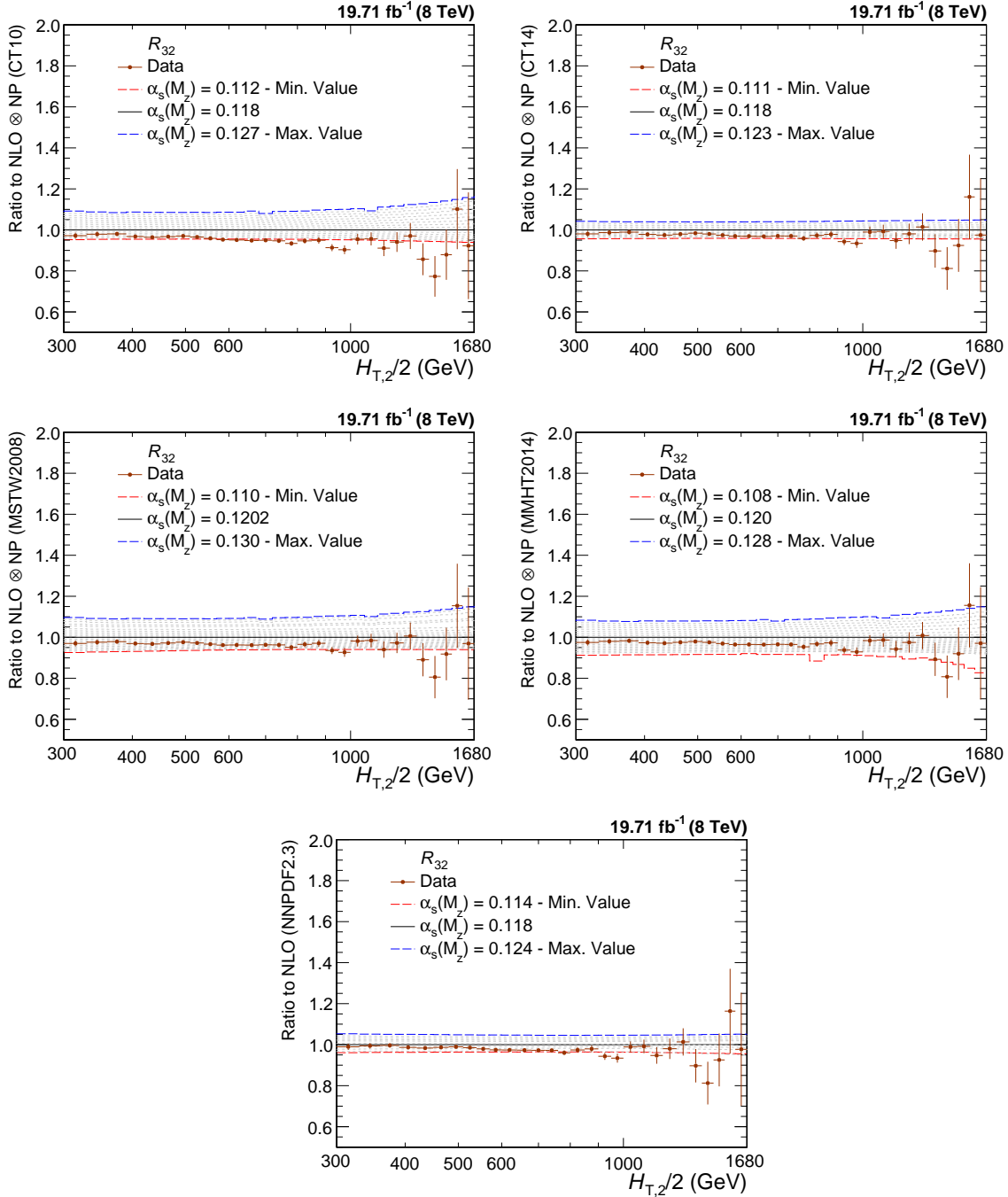


Figure 7.3: Ratio of the cross-section ratio,  $R_{32}$  to theory predictions using the CT10 (top left), the CT14 (top right), the MSTW2008 (middle left), the MMHT2014 (middle right) and NNPDF2.3 (bottom) NLO PDF sets for a series of values of  $\alpha_s(M_Z)$ . The  $\alpha_s(M_Z)$  value is varied in the range 0.112-0.127, 0.111-123, 0.110-0.130, 0.108-0.128 and 0.114-0.124 in steps of 0.001 for the CT10, CT14, MSTW2008, MMHT2014 and NNPDF2.3 NLO PDF sets, respectively. The error bars correspond to the total experimental uncertainty. The theory predictions are corrected for non-perturbative (NP) effects.

where  $M$  is the vector of the differences between the data ( $D^i$ ) and the theoretical values ( $T^i$ ) in each bin  $i$ ,

$$M^i = D^i - T^i \quad (7.3)$$

and  $C$  is the covariance matrix including all experimental uncertainties as described in Sec. 5.6 and some theoretical uncertainties discussed in Sec. 6.2. The covariance matrix  $C = C_{\text{exp}} + C_{\text{theo}}$  is defined as the sum of covariances of experimental and theoretical sources of uncertainty as follows :

$$C_{\text{exp}} = \text{Cov}^{\text{ExpStat}} + \sum \text{Cov}^{\text{JEC}} + \text{Cov}^{\text{Unfolding}} + \text{Cov}^{\text{Lumi}} + \text{Cov}^{\text{Residual}} \quad (7.4)$$

$$C_{\text{theo}} = \text{Cov}^{\text{TheoStat}} + \text{Cov}^{\text{NP}} + \text{Cov}^{\text{PDF}} \quad (7.5)$$

where the labelled covariance matrices account for the following effects:

- $\text{Cov}^{\text{ExpStat}}$ : statistical uncertainty of the data including correlations introduced by the unfolding
- $\text{Cov}^{\text{JEC}}$ : the jet energy corrections (JEC) systematic uncertainty
- $\text{Cov}^{\text{Unfolding}}$ : the unfolding systematic uncertainty including the resolution (JER) and model dependence
- $\text{Cov}^{\text{Lumi}}$ : the luminosity uncertainty
- $\text{Cov}^{\text{Residual}}$ : a residual uncorrelated systematic uncertainty summarizing individual causes such as small trigger and identification inefficiencies, time dependence of the jet  $p_T$  resolution, and uncertainty on the trigger prescale factors
- $\text{Cov}^{\text{TheoStat}}$ : statistical uncertainty caused by numerical integrations in the cross-section computations

- $\text{Cov}^{\text{NP}}$ : the systematic uncertainty of the non-perturbative (NP) corrections
- $\text{Cov}^{\text{PDF}}$ : the PDF uncertainties

While taking the differences between theory and data, the treatment of experimental and theoretical systematic uncertainties is crucial. The Unfolding, JEC, Lumi and PDF and NP systematic uncertainties are treated as 100% correlated among  $H_{T,2}/2$  bins. If  $\delta_i$  is the total uncertainty on the differential cross-section, for the  $i$ -th  $H_{T,2}/2$  bin, for any of these fully correlated sources, then the  $i, j$ -th element of the corresponding covariance matrix is given by  $\text{COV}_{ij} = \delta_i \times \delta_j$ . The JEC, unfolding, and luminosity uncertainties are treated as multiplicative to avoid the statistical bias that arises when estimating uncertainties from data. In fits of the ratio  $R_{32}$ , the luminosity and residual uncorrelated uncertainties cancel completely. Partial cancellations between the other sources of uncertainty are taken into account in the fit.

The evaluation of PDF uncertainty depends on the individual PDF set as already discussed in Sec. 6.2.2. The PDF covariance matrix construction varies among different PDF sets. The CT10, CT14, MMHT2014 and MSTW2008 NLO PDF sets employ the eigenvector method to evaluate the PDF uncertainties as explained in Sec. 6.2.2. The number of eigenvectors ( $N_{\text{ev}}$ ) with two PDF members per eigenvector for CT10, CT14, MMHT2014 and MSTW2008 NLO PDF sets are 26, 28, 25 and 20, respectively. The NNPDF2.3 PDF set comes with hundred different replicas ( $N_{\text{rep}}$ ) instead of different eigenvectors, as for CT10 or CT14 PDF sets. The mean uncertainty is calculated as average uncertainty from 100 different replicas. Following the prescription given in [103], the PDF uncertainty is calculated as :

$$(\Delta X)^2 = \frac{1}{N_{\text{rep}} - 1} \sum_{k=1}^{N_{\text{rep}}} [X_k - \langle X_k \rangle]^2 \quad (7.6)$$

where  $\Delta X$  is the uncertainty on predicted differential cross-section,  $X_k$  is the differ-

ential cross-section for  $k$ -th replica and  $\langle X_k \rangle$  is the average differential cross-section from all the replicas.

Scale uncertainties of the pQCD predictions are taken into account by employing the offset method, i.e. by performing separate fits with varying scale factors as described in the Sec. 6.2.1. The largest upwards and downwards deviations from the default factors are defined as the uncertainty. At NLO such scale variations predominantly lead to smaller cross-sections and also a smaller ratio  $R_{32}$  as visible in Fig. 6.5. As a consequence the scale uncertainty in fits is equally asymmetric, where smaller cross-sections or ratios are compensated by an increase in the fitted value for  $\alpha_s(M_Z)$ .

### 7.2.2 Fit Results

To determine the value of the strong coupling constant at the scale of the  $Z$  boson mass  $\alpha_s(M_Z)$ , fits to the differential inclusive 2-jet and 3-jet events cross-sections are performed using five different NLO PDF sets : CT10, CT14, MSTW2008, MMHT2014 and NNPDF2.3. The range in  $H_{\mathrm{T},2}/2$  is restricted to be between 300 GeV and 1 TeV to avoid the region close to the minimal  $p_{\mathrm{T}}$  threshold of 150 GeV for each jet at low  $p_{\mathrm{T}}$  and the onset of electroweak effects at high  $H_{\mathrm{T},2}/2$ , which are available for the dijet case only. The  $\alpha_s(M_Z)$  results obtained from a simultaneous fit to all 19  $H_{\mathrm{T},2}/2$  bins in the above mentioned range are reported in Table 7.1. For comparison, a simultaneous fit to both cross-sections ignoring any correlations, and a fit to the cross-section ratio  $R_{32}$ , fully accounting for correlations is also performed and the results are tabulated in Table 7.2. The electroweak effects are assumed to cancel in the ratio as do the luminosity and the uncorrelated uncertainty.

All cross-section fits give compatible values for  $\alpha_s(M_Z)$  in the range of 0.115–0.118 whereas for the ratio  $R_{32}$  somewhat smaller values are obtained. But for individual cross-sections,  $\chi^2/n_{\mathrm{dof}}$  values are small as compared to the cross-section

ratio  $R_{32}$ . A possible explanation is an overestimation of the residual uncorrelated uncertainty of 1% that is cancelled for  $R_{32}$ . If the fits are repeated with an assumed uncertainty of 0.25% instead, the  $\chi^2/n_{\text{dof}}$  values lie around unity while the  $\alpha_s(M_Z)$  values are still compatible with the previous results but with slightly reduced uncertainties.

Table 7.1: Determination of  $\alpha_s(M_Z)$  from the inclusive 2-jet and 3-jet event cross-sections using five PDF sets at NLO. Only total uncertainties without scale variations are quoted. The results are obtained from a simultaneous fit to all 19  $H_{\text{T},2}/2$  bins in the restricted range of  $0.3 < H_{\text{T},2}/2 < 1.0$  TeV.

PDF set	Inclusive 2-jets			Inclusive 3-jets		
	$\alpha_s(M_Z)$	$\pm \Delta \alpha_s(M_Z)$	$\chi^2/n_{\text{dof}}$	$\alpha_s(M_Z)$	$\pm \Delta \alpha_s(M_Z)$	$\chi^2/n_{\text{dof}}$
CT10	0.1174	0.0032	3.0/18	0.1169	0.0027	5.4/18
CT14	0.1160	0.0035	3.5/18	0.1159	0.0031	6.1/18
MSTW2008	0.1159	0.0025	5.3/18	0.1161	0.0021	6.7/18
MMHT2014	0.1165	0.0034	5.9/18	0.1166	0.0025	7.1/18
NNPDF2.3	0.1183	0.0025	9.7/18	0.1179	0.0021	9.1/18

Table 7.2: Determination of  $\alpha_s(M_Z)$  from the inclusive 2-jet and 3-jet event cross-sections simultaneously and from their ratio  $R_{32}$  using five PDF sets at NLO. Only total uncertainties without scale variations are quoted. The results are obtained from a simultaneous fit to all 38 (left) and 19 (right)  $H_{\text{T},2}/2$  bins in the restricted range of  $0.3 < H_{\text{T},2}/2 < 1.0$  TeV. For comparison, correlations between the two cross-sections are neglected in the simultaneous fit on the left, but fully taken into account in the ratio fit on the right.

PDF set	Inclusive 2- and 3-jets			$R_{32}$		
	$\alpha_s(M_Z)$	$\pm \Delta \alpha_s(M_Z)$	$\chi^2/n_{\text{dof}}$	$\alpha_s(M_Z)$	$\pm \Delta \alpha_s(M_Z)$	$\chi^2/n_{\text{dof}}$
CT10	0.1170	0.0026	8.2/37	0.1141	0.0028	19./18
CT14	0.1161	0.0029	9.1/37	0.1139	0.0032	15./18
MSTW2008	0.1161	0.0021	11./37	0.1150	0.0023	21./18
MMHT2014	0.1168	0.0025	11./37	0.1142	0.0022	19./18
NNPDF2.3	0.1188	0.0019	15./37	0.1184	0.0021	12./18

To investigate how the electroweak (EW) corrections affect the fit results for  $\alpha_s(M_Z)$ , the range in  $H_{\text{T},2}/2$  is extended to  $0.3 < H_{\text{T},2}/2 < 1.68$  TeV.  $\alpha_s(M_Z)$  values are obtained from fits to the inclusive 2-jet event cross-section in this range with or without EW correction factors and the results are presented in Table 7.3. The largest impact is a reduction in  $\chi^2/n_{\text{dof}}$ , which indicates a better agreement when

EW effects are included. In addition, a tendency to slightly smaller  $\alpha_s(M_Z)$  values is observed without the EW corrections. For the ratio  $R_{32}$ , it is expected that these effects are much reduced.

Table 7.3: Determination of  $\alpha_s(M_Z)$  from the inclusive 2-jet event cross-section using five PDF sets at NLO without (left) and with (right) electroweak (EW) corrections. Only total uncertainties without scale variations are quoted. The results are obtained from a simultaneous fit to all 29  $H_{T,2}/2$  bins in the range of  $0.3 < H_{T,2}/2 < 1.68$  TeV.

PDF set	without EW			with EW		
	$\alpha_s(M_Z)$	$\pm \Delta \alpha_s(M_Z)$	$\chi^2/n_{\text{dof}}$	$\alpha_s(M_Z)$	$\pm \Delta \alpha_s(M_Z)$	$\chi^2/n_{\text{dof}}$
CT10	0.1163	0.0034	15./28	0.1165	0.0032	14./28
CT14	0.1137	0.0033	24./28	0.1144	0.0033	17./28
MSTW2008	0.1093	0.0028	27./28	0.1133	0.0023	19./28
MMHT2014	0.1127	0.0032	32./28	0.1141	0.0032	21./28
NNPDF2.3	0.1162	0.0024	31./28	0.1168	0.0024	23./28

From Fig. 7.3 follows that only the PDF sets MSTW2008 and MMHT2014 provide a large enough range in  $\alpha_s(M_Z)$  values to ensure fits without extrapolation. The other three PDF sets are at the limit such that reliable fits cannot be performed for all scale settings and/or bins in scale  $Q = H_{T,2}/2$ . Since many systematic uncertainties cancel completely or partially in the cross-section ratio  $R_{32}$  as compared to the individual cross-sections,  $R_{32}$  is used mainly to determine the value of  $\alpha_s(M_Z)$ . Table 7.4 give the complete results for MSTW2008 and MMHT2014 for the full range in  $H_{T,2}/2$  of 300 GeV up to 1.68 TeV along with the corresponding components of PDF, scale, NP and total experimental except scale uncertainties are shown. In contrast to fits at NLO using cross-sections where the scale uncertainty recipe usually leads to a very asymmetric behaviour with larger downward uncertainties in the case, this is inverted for the fits to the cross-section ratio  $R_{32}$ . The scale uncertainty is the most dominant source of total uncertainty on  $\alpha_s(M_Z)$ . These values are determined with the central renormalization and factorization scales i.e.  $\mu_r = \mu_f = H_{T,2}/2$ . The values are also determined for the six scale factor combinations for the two PDF sets MSTW2008 and MMHT2014 and results are shown in Table 7.5.

The uncertainty decomposition for  $\alpha_s(M_Z)$  determined from cross-section ratio  $R_{32}$  is performed in four sub-ranges of  $H_{T,2}/2$  and the results are shown in Table 7.6. The statistical uncertainty of the NLO computation is negligible in comparison to any of the other sources of uncertainty. Electroweak corrections, significant only at high  $H_{T,2}/2$ , are assumed to cancel between the numerator and denominator.

Using the MSTW2008 PDF set, which dates from before the LHC start, the strong coupling constant finally is determined to

$$\begin{aligned} \alpha_s(M_Z) &= 0.1150 \pm 0.0010 \text{ (exp)} \pm 0.0013 \text{ (PDF)} \pm 0.0015 \text{ (NP)} {}^{+0.0050}_{-0.0000} \text{ (scale)} \\ &= 0.1150 \pm 0.0023 \text{ (all except scale)} {}^{+0.0050}_{-0.0000} \text{ (scale)} \end{aligned} \tag{7.7}$$

The MMHT2014 PDF set, although using LHC jet data to determine the PDF parameters, leads to a very similar result of

$$\begin{aligned} \alpha_s(M_Z) &= 0.1142 \pm 0.0010 \text{ (exp)} \pm 0.0013 \text{ (PDF)} \pm 0.0014 \text{ (NP)} {}^{+0.0049}_{-0.0006} \text{ (scale)} \\ &= 0.1142 \pm 0.0022 \text{ (all except scale)} {}^{+0.0049}_{-0.0006} \text{ (scale)} \end{aligned} \tag{7.8}$$

### 7.3 Running of the Strong Coupling Constant

The value of the strong coupling constant  $\alpha_S$  depends on the energy scale  $Q$  and it decreases with the increase of scale  $Q$ . To study this dependence, the determination of  $\alpha_S$  is carried out at different energies. The procedure to extract  $\alpha_S(Q)$  is same as the one followed for the  $\alpha_s(M_Z)$ . To have different energy scales, the fitted  $H_{T,2}/2$  range 300 - 1680 GeV is divided into four different sub-ranges as shown by the first column in Table 7.7. Each of the  $H_{T,2}/2$  range is associated with a scale  $Q$ , which

Table 7.4: Determination of  $\alpha_s(M_Z)$  from the ratio  $R_{32}$  using the two most compatible PDF sets MSTW2008 and MMHT2014 at NLO along with the corresponding components of PDF, scale, NP and total (except scale) experimental uncertainties. The results are obtained from a simultaneous fit to all 29  $H_{T,2}/2$  bins in the full range of  $0.3 < H_{T,2}/2 < 1.68$  TeV.

PDF set	$\alpha_s(M_Z)$	exp	PDF	NP	all exc.	scale	$\chi^2/n_{\text{dof}}$
MSTW2008	0.1150	$\pm 0.0010$	$\pm 0.0013$	$\pm 0.0015$	$\pm 0.0023$	$^{+0.0050}_{-0.0000}$	26./28
MMHT2014	0.1142	$\pm 0.0010$	$\pm 0.0013$	$\pm 0.0014$	$\pm 0.0022$	$^{+0.0049}_{-0.0006}$	24./28

Table 7.5: Determination of  $\alpha_s(M_Z)$  from the ratio  $R_{32}$  in the  $H_{T,2}/2$  range from 0.3 up to 1.68 TeV at the central scale and for the six scale factor combinations for the two PDF sets MSTW2008 and MMHT2014.

$\mu_r/H_{T,2}/2$	$\mu_f/H_{T,2}/2$	MSTW2008		MMHT2014	
		$\alpha_s(M_Z)$	$\chi^2/n_{\text{dof}}$	$\alpha_s(M_Z)$	$\chi^2/n_{\text{dof}}$
1	1	0.1150	26./28	0.1142	24./28
1/2	1/2	0.1165	77./28	0.1160	73./28
2	2	0.1200	18./28	0.1191	18./28
1/2	1	0.1150	53./28	0.1136	48./28
1	1/2	0.1150	30./28	0.1142	28./28
1	2	0.1155	23./28	0.1147	22./28
2	1	0.1180	19./28	0.1175	19./28

Table 7.6: Uncertainty decomposition for  $\alpha_s(M_Z)$  from the determination of  $\alpha_s$  from the jet event rate  $R_{32}$  in bins of  $H_{T,2}/2$ . The statistical uncertainty of the NLO computation is negligible in comparison to any of the other sources of uncertainty. Electroweak corrections, significant only at high  $H_{T,2}/2$ , are assumed to cancel between the numerator and denominator.

$H_{T,2}/2$ (GeV)	MSTW2008					MMHT2014				
	$\alpha_s(M_Z)$	exp	PDF	NP	scale	$\alpha_s(M_Z)$	exp	PDF	NP	scale
300-420	0.1157	$\pm 0.0015$	$\pm 0.0014$	$\pm 0.0019$	$^{+0.0053}_{-0.0000}$	0.1158	$\pm 0.0014$	$\pm 0.0010$	$\pm 0.0019$	$^{+0.0052}_{-0.0000}$
420-600	0.1153	$\pm 0.0011$	$\pm 0.0014$	$\pm 0.0018$	$^{+0.0057}_{-0.0000}$	0.1154	$\pm 0.0011$	$\pm 0.0012$	$\pm 0.0017$	$^{+0.0056}_{-0.0000}$
600-1000	0.1134	$\pm 0.0013$	$\pm 0.0016$	$\pm 0.0019$	$^{+0.0052}_{-0.0000}$	0.1140	$\pm 0.0012$	$\pm 0.0012$	$\pm 0.0018$	$^{+0.0045}_{-0.0000}$
1000-1680	0.1147	$\pm 0.0029$	$\pm 0.0017$	$\pm 0.0018$	$^{+0.0063}_{-0.0011}$	0.1154	$\pm 0.0025$	$\pm 0.0014$	$\pm 0.0015$	$^{+0.0056}_{-0.0011}$
300-1680	0.1150	$\pm 0.0010$	$\pm 0.0013$	$\pm 0.0015$	$^{+0.0050}_{-0.0000}$	0.1142	$\pm 0.0010$	$\pm 0.0013$	$\pm 0.0014$	$^{+0.0049}_{-0.0006}$

is the differential cross-section weighted average  $H_{\mathrm{T},2}/2$  scale from the inclusive 2-jet calculations and integrated over all the measured  $H_{\mathrm{T},2}/2$  bins contributing to that given  $H_{\mathrm{T},2}/2$  range. Let  $N_{\mathrm{bin}}^j$  be the total number of measured  $H_{\mathrm{T},2}/2$  bins contributing to the  $j$ -th  $H_{\mathrm{T},2}/2$  range, then the corresponding scale  $Q_j$ , shown in second column of Table 7.7, is calculated as :

$$Q_j = \frac{\sum_{i=1}^{N_{\mathrm{bin}}^j} H_{\mathrm{T},2}^i \left[ \frac{\mathrm{d}\sigma}{\mathrm{d}(H_{\mathrm{T},2}/2)} \right]^i}{\sum_{i=1}^{N_{\mathrm{bin}}^j} \left[ \frac{\mathrm{d}\sigma}{\mathrm{d}(H_{\mathrm{T},2}/2)} \right]^i} \quad (7.9)$$

The value of  $\alpha_s(M_Z)$  is extracted in each  $H_{\mathrm{T},2}/2$  range. These extracted  $\alpha_s(M_Z)$  values are evolved to the corresponding values  $\alpha_s(Q)$  and are quoted in Table 7.7 along with the extracted  $\alpha_s(M_Z)$  values and the total uncertainty. The evolution is performed for five flavours at 2-loop order with the RUNDEC program [104, 105]. The obtained  $\alpha_s(Q)$  points (black solid circles) are shown as a function of scale  $Q$  in Fig. 7.4. The black solid line and the yellow uncertainty band are evolved using  $\alpha_s(M_Z) = 0.1150 \pm 0.0023$  (all except scale)  $^{+0.0050}_{-0.0000}$  (scale) obtained using MSTW2008 NLO PDF set. The world average [18] (dashed line) and results from other measurements of the CMS [1, 65, 80, 94, 95], ATLAS [96], D0 [97, 98], H1 [99, 100], and ZEUS [101] experiments are also imposed. The current measurement is in very good agreement within the uncertainty with other results obtained by previous experiments as well as with the world average value of  $\alpha_s(M_Z) = 0.1181 \pm 0.0011$  derived in Ref. [18].

Table 7.7: Evolution of the strong coupling constant between the scale of the  $Z$  boson mass and the cross-section averaged  $H_{T,2}/2$  scale  $\langle Q \rangle$  for the separate determinations in each respective fit range. The evolution is performed for five flavours at 2-loop order with the RUNDEC program [104, 105].

$H_{T,2}/2$ (GeV)	$\langle Q \rangle$ (GeV)	$\alpha_s(M_Z)$	$\alpha_S(Q)$	No. of data points	$\chi^2/n_{\text{dof}}$
300-420	340	$0.1157^{+0.0060}_{-0.0030}$	$0.0969^{+0.0041}_{-0.0021}$	4	2.8/3
420-600	476	$0.1153^{+0.0062}_{-0.0025}$	$0.0928^{+0.0039}_{-0.0016}$	6	6.1/5
600-1000	685	$0.1134^{+0.0059}_{-0.0028}$	$0.0879^{+0.0035}_{-0.0017}$	9	7.1/8
1000-1680	1114	$0.1147^{+0.0074}_{-0.0040}$	$0.0841^{+0.0039}_{-0.0021}$	10	5.4/9

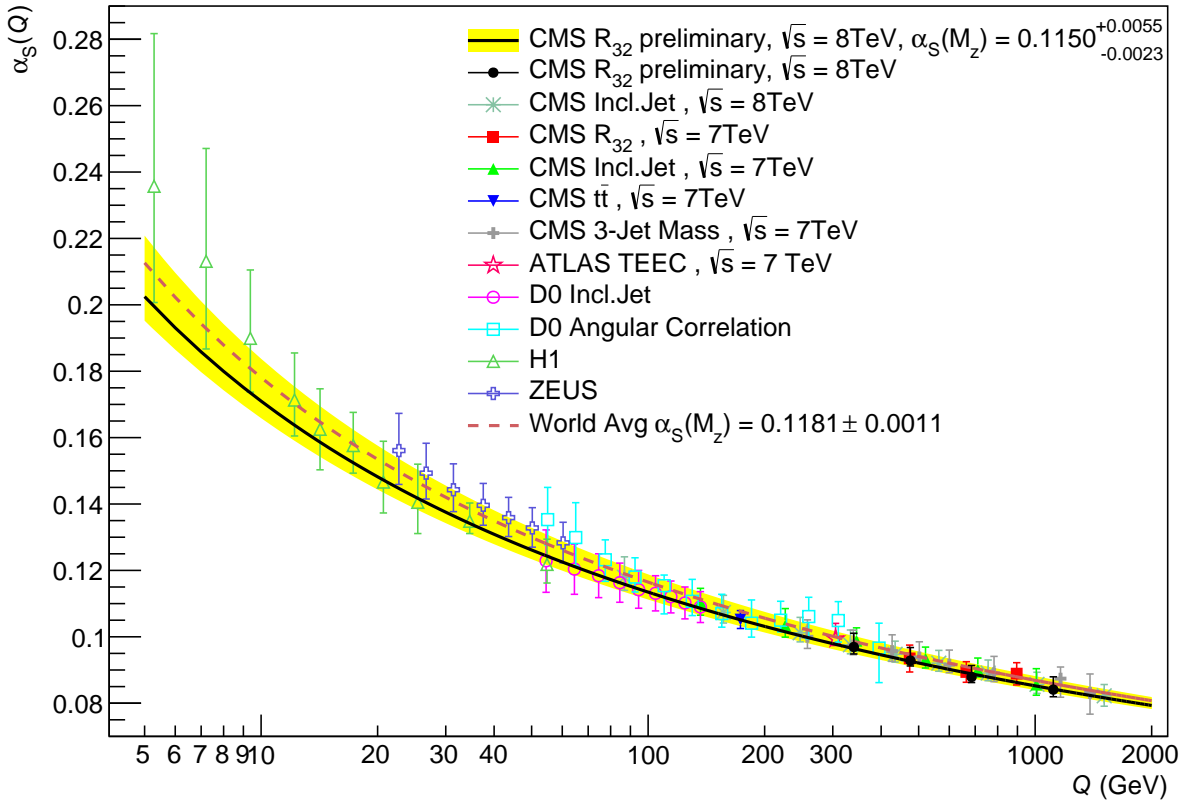


Figure 7.4: The running  $\alpha_S(Q)$  as a function of the scale  $Q$  is shown as obtained by using the MSTW2008 NLO PDF set. The solid line and the uncertainty band are drawn by evolving the extracted  $\alpha_s(M_Z)$  values using the 2-loop 5-flavour renormalization group equations as implemented in RUNDEC [104, 105]. The dashed line represents the evolution of the world average [18] and the black circles correspond to the  $\alpha_S(Q)$  determinations presented in Table 7.7. Results from other measurements of CMS [1, 65, 80, 94, 95], ATLAS [96], D0 [97, 98], H1 [99, 100], and ZEUS [101] are superimposed.

# Chapter 8

## Summary

Inclusive multijet production cross-section measured precisely in terms of jet transverse momentum is one of the important observables in understanding physics at hadron colliders. It provides the essential information about the structure of parton through parton distribution functions (PDFs) and the precise measurement of the strong coupling constant  $\alpha_S$ . The value of the strong coupling constant at the scale of the  $Z$  boson mass  $\alpha_s(M_Z)$  can be determined using cross-section ratio instead of individual cross-sections because many uncertainties of theoretical and experimental origin cancel between numerator and denominator which reduces the dependence on PDFs, renormalization and factorization scales, luminosity etc.

In this thesis, a measurement of the inclusive 2-jet and 3-jet event cross-sections as well as the cross-section ratio  $R_{32}$  has been presented. The data sample has been collected from proton-proton collisions recorded with the CMS detector at a centre-of-mass energy of 8 TeV and corresponds to an integrated luminosity of  $19.7\text{fb}^{-1}$ . The jets are reconstructed with the anti- $k_t$  clustering algorithm for a jet size parameter  $R = 0.7$ . The inclusive 2-jet and 3-jet event cross-sections are measured differentially as a function of the average transverse momentum of the two leading jets, referred as  $H_{T,2}/2$ . The ratio  $R_{32}$  is obtained by dividing the differential cross-sections of inclusive 3-jet events to that of inclusive 2-jet one in

each bin of  $H_{\mathrm{T},2}/2$ . An appropriate selection criteria has been designed for choosing the best events for analysis. The measurements are performed at a central rapidity of  $|y| < 2.5$  in a range of  $0.3 < H_{\mathrm{T},2}/2 < 2.0 \text{ TeV}$  for inclusive 2-jet event cross-sections and  $0.3 < H_{\mathrm{T},2}/2 < 1.68 \text{ TeV}$  for inclusive 3-jet event cross-sections and ratio  $R_{32}$ .

The measured cross-sections after correcting for detector effects by using an iterative unfolding procedure are compared to the perturbative QCD predictions computed, using NLOJET++ program, at next-to-leading order (NLO) accuracy and complemented with non-perturbative (NP) corrections that are important at low  $H_{\mathrm{T},2}/2$ . The data are found to be well described by NLO calculations. The upwards trend observed in the inclusive 2-jet and 3-jet data at high  $H_{\mathrm{T},2}/2$  in comparison to the prediction at NLO QCD, is explained by the onset of electroweak (EW) corrections in the 2-jet case. For the 3-jet event cross-sections these corrections have not yet been computed yet. In the 3-jet to 2-jet cross-section ratio  $R_{32}$ , the EW corrections are assumed to cancel. In fact, NLO QCD provides an adequate description of  $R_{32}$  in the accessible range of  $H_{\mathrm{T},2}/2$ . In contrast, leading order (LO) tree-level Monte Carlo (MC) predictions obtained using MADGRAPH5 event generator interfaced to PYTHIA6 exhibit significant deviations. The sources of experimental and theoretical uncertainties are studied in details. The experimental uncertainty ranges from 4 to 32% for inclusive 2-jet event cross-sections, from 4 to 28% for 3-jet event cross-sections and from 1 to 28% for cross-section ratio  $R_{32}$ . It is dominated by the uncertainty due to the jet energy corrections (JEC) at lower  $H_{\mathrm{T},2}/2$  values and by statistical uncertainty at higher  $H_{\mathrm{T},2}/2$  values. The theoretical uncertainty ranges from 3 to 30% and 5 to 34% for inclusive 2-jet and 3-jet event cross-sections respectively and from 3 to 11% for ratio  $R_{32}$ . The PDF uncertainty derived with the CT10-NLO PDF set is the dominant source of theoretical uncertainty.

The inclusive multijet cross-sections being proportional to the powers of the strong coupling constant  $\alpha_S$  ( $\sigma_{n\text{-jet}} \propto \alpha_S^n$ ) are used to extract the value of the strong coupling constant at the scale of the  $Z$  boson mass  $\alpha_s(M_Z)$ . In cross-section ratio  $R_{32}$  which proportional to  $\alpha_S$ , many uncertainties and PDF dependencies largely cancel and hence becomes the better tool to extract the value of  $\alpha_s(M_Z)$ . In this thesis, a fit of the ratio of the inclusive 3-jet event cross-section to that of 2-jet,  $R_{32}$  in the range  $0.3 < H_{T,2}/2 < 1.68$  TeV using the MSTW2008 PDF set gives :

$$\begin{aligned}\alpha_s(M_Z) &= 0.1150 \pm 0.0010 \text{ (exp)} \pm 0.0013 \text{ (PDF)} \pm 0.0015 \text{ (NP)} {}^{+0.0050}_{-0.0000} \text{ (scale)} \\ &= 0.1150 \pm 0.0023 \text{ (all except scale)} {}^{+0.0050}_{-0.0000} \text{ (scale)}\end{aligned}$$

Very similar results are obtained using the MMHT2014 PDF set which gives :

$$\begin{aligned}\alpha_s(M_Z) &= 0.1142 \pm 0.0010 \text{ (exp)} \pm 0.0013 \text{ (PDF)} \pm 0.0014 \text{ (NP)} {}^{+0.0049}_{-0.0006} \text{ (scale)} \\ &= 0.1142 \pm 0.0022 \text{ (all except scale)} {}^{+0.0049}_{-0.0006} \text{ (scale)}\end{aligned}$$

The equally compatible values of  $\alpha_s(M_Z)$  are determined with separate fits to the inclusive 2-jet and 3-jet event cross-sections provided the range in  $H_{T,2}/2$  is restricted to  $0.3 < H_{T,2}/2 < 1.0$  TeV. The extracted  $\alpha_s(M_Z)$  values in sub-ranges of  $H_{T,2}/2$  are evolved to corresponding  $\alpha_S(Q)$  along with the error bars at different scales  $Q$ . The current measurement of  $\alpha_s(M_Z)$  and the running of  $\alpha_S(Q)$  as a function of  $Q$  is in well agreement within uncertainties with the world average value of  $\alpha_s(M_Z) = 0.1181 \pm 0.0011$  [18] and already existing determinations performed by the CMS and other experiments.

The inclusion of the EW corrections in inclusive 2-jet event cross-sections become relevant at  $H_{T,2}/2$  beyond 1 TeV. Their availability for 3-jet one and hence cross-section ratio  $R_{32}$  can improve the precision of the measurement of  $\alpha_s(M_Z)$ . Also as the theoretical calculations will be available for inclusive 4-jet event cross-sections, the various cross-section ratios such as  $R_{43} \propto \alpha_S^1$  and  $R_{42} \propto \alpha_S^2$  can be measured to extract the value of the strong coupling constant more precisely. Currently LHC is running at high center-of-mass energy of 13 TeV delivering a higher

instantaneous luminosity and this makes possible to access the extended phase space and perform the measurements with more accuracy.

# **Appendix A**

## A.1 Cross-section Ratio, $R_{32}$

Table A.1: Differential cross-sections ( $\times 10^{-3}(\text{pb}/\text{GeV})$ ) and cross-section ratio  $R_{32}$  at detector level in each bin of  $H_{\text{T},2}/2$ , along with statistical uncertainty (in %).

Bin	2-jet cross-section	Stat. unc.	3-jet cross-section	Stat. unc.	Ratio $R_{32}$	Stat. unc.
300 - 330	29772.726	0.211	2640.629	0.707	0.089	+0.665 -0.661
330 - 360	16792.917	0.231	1773.485	0.704	0.106	+0.523 -0.521
360 - 390	9889.326	0.182	1176.544	0.526	0.119	+0.485 -0.483
390 - 420	5976.777	0.179	778.034	0.492	0.130	+0.206 -0.206
420 - 450	3731.760	0.067	522.624	0.180	0.140	+0.167 -0.167
450 - 480	2398.741	0.084	357.622	0.217	0.149	+0.201 -0.200
480 - 510	1570.192	0.104	246.051	0.262	0.157	+0.241 -0.241
510 - 540	1048.665	0.127	171.080	0.314	0.163	+0.288 -0.287
540 - 570	713.042	0.154	119.566	0.376	0.168	+0.344 -0.343
570 - 600	490.776	0.186	84.798	0.447	0.173	+0.407 -0.406
600 - 640	325.046	0.198	57.463	0.470	0.177	+0.427 -0.426
640 - 680	205.727	0.248	37.282	0.583	0.181	+0.529 -0.527
680 - 720	133.674	0.308	24.859	0.714	0.186	+0.646 -0.643
720 - 760	87.911	0.380	16.560	0.875	0.188	+0.791 -0.786
760 - 800	58.657	0.465	11.056	1.071	0.188	+0.968 -0.961
800 - 850	38.106	0.516	7.318	1.178	0.192	+1.063 -1.054
850 - 900	23.587	0.656	4.600	1.485	0.195	+1.339 -1.326
900 - 950	15.130	0.819	2.896	1.872	0.191	+1.694 -1.672
950 - 1000	9.696	1.023	1.812	2.366	0.187	+2.151 -2.116
1000 - 1060	6.026	1.185	1.186	2.670	0.197	+2.414 -2.371
1060 - 1120	3.668	1.518	0.716	3.436	0.195	+3.118 -3.046
1120 - 1180	2.327	1.906	0.437	4.398	0.188	+4.024 -3.903
1180 - 1250	1.419	2.260	0.265	5.227	0.187	+4.798 -4.627
1250 - 1320	0.853	2.915	0.165	6.623	0.194	+6.080 -5.811
1320 - 1390	0.477	3.898	0.080	9.492	0.169	+8.951 -8.355
1390 - 1460	0.263	5.249	0.042	13.131	0.160	+12.619 -11.449
1460 - 1530	0.192	6.143	0.029	15.811	0.151	+15.437 -13.698
1530 - 1600	0.104	8.362	0.021	18.570	0.203	+17.571 -15.536
1600 - 1680	0.060	10.314	0.009	26.726	0.149	+27.132 -22.170

## A.2 Individual Sources of Jet Energy Correction Uncertainties

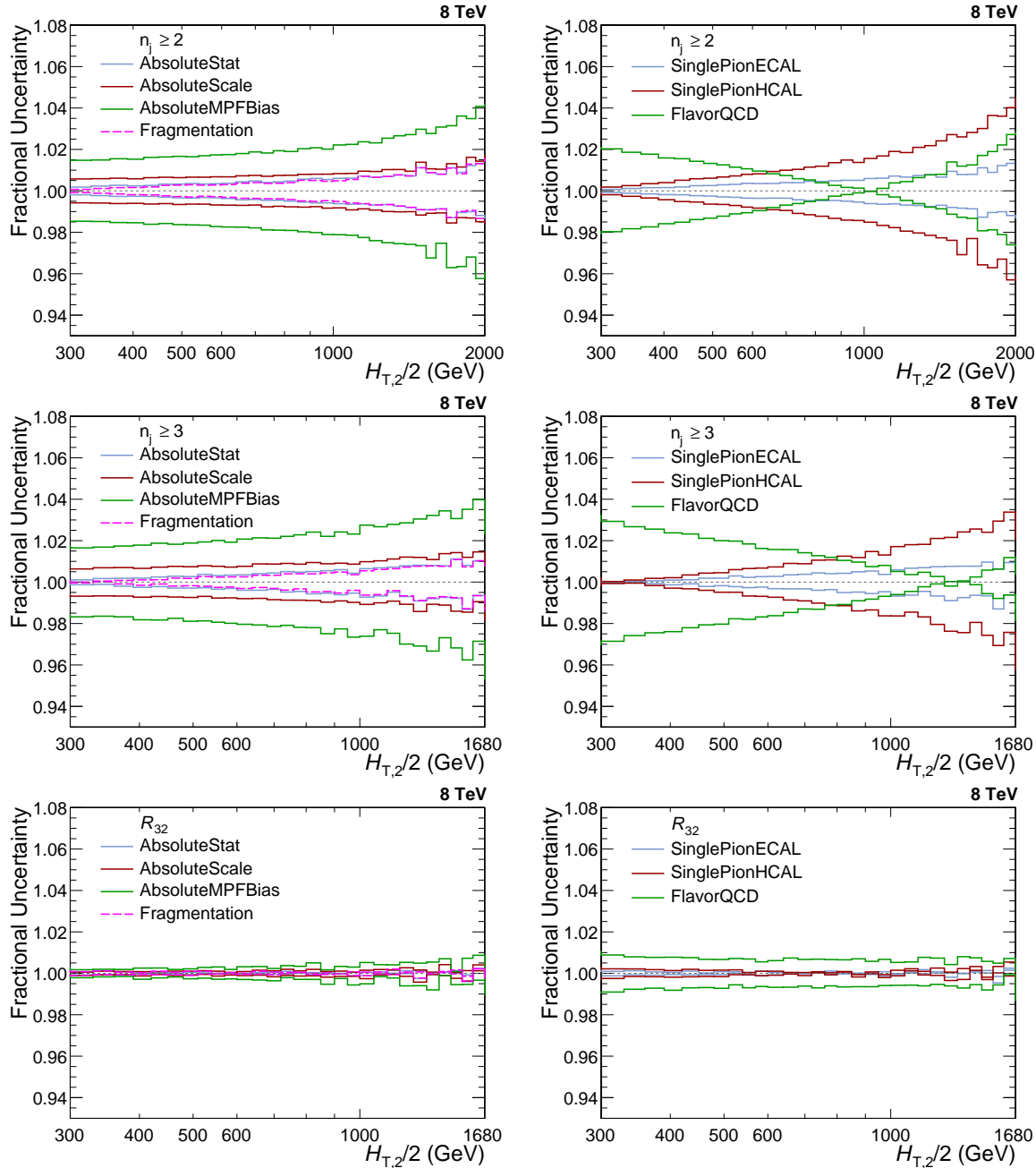


Figure A.1: The fractional jet energy correction (JEC) uncertainties from individual sources are shown for inclusive 2-jet (top) and 3-jet events cross-sections (middle); and cross-section ratio  $R_{32}$  (bottom). On left, JEC uncertainties are evaluated from AbsoluteStat (blue), AbsoluteScale (red), AbsoluteMPFBias (green) and Fragmentation (pink) sources whereas on right, these are evaluated from SinglePionECAL (blue), SinglePionHCAL (red) and FlavorQCD (green) sources.

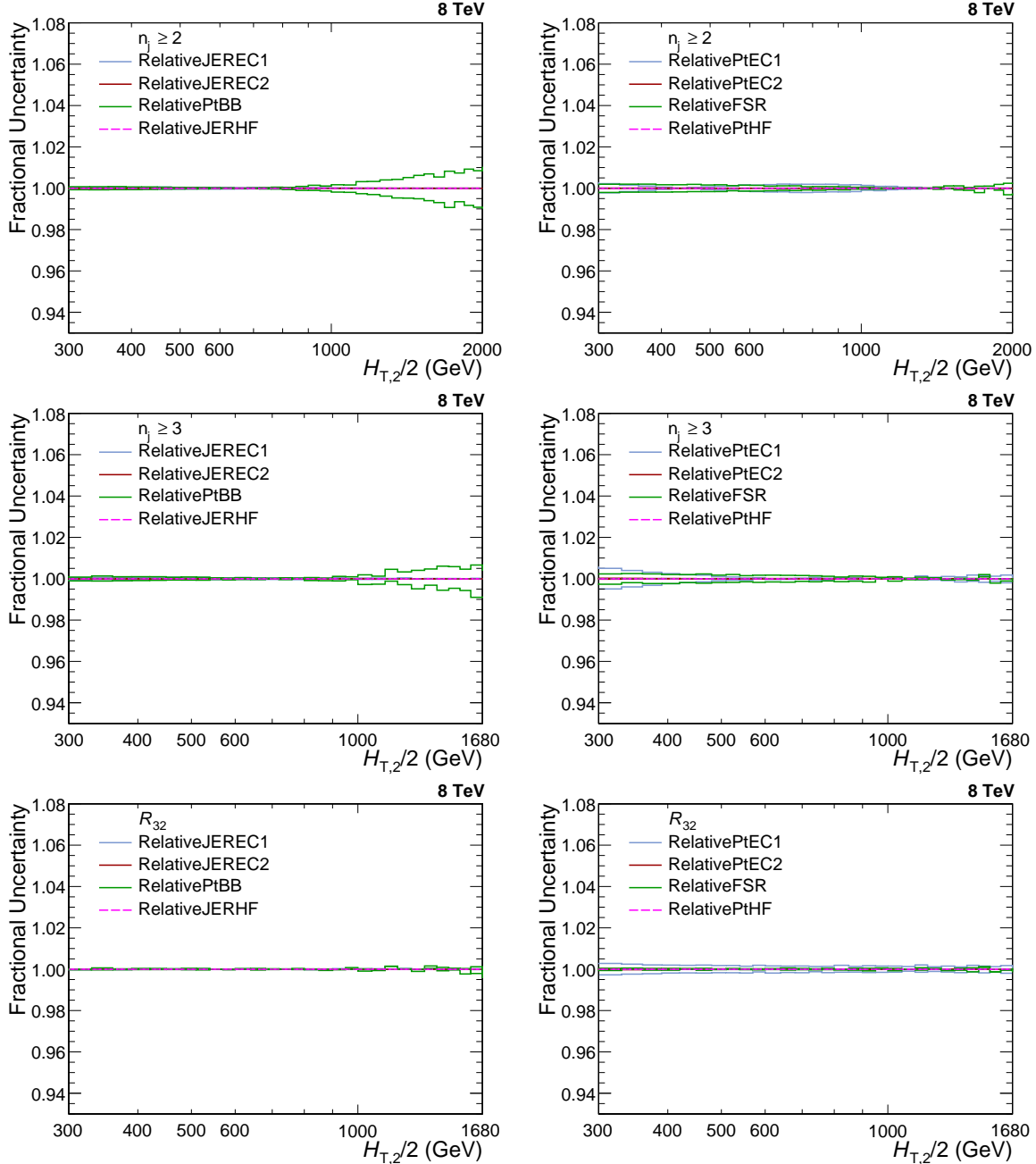


Figure A.2: The fractional jet energy correction (JEC) uncertainties from individual sources are shown for inclusive 2-jet (top) and 3-jet events cross-sections (middle); and cross-section ratio  $R_{32}$  (bottom). On left, JEC uncertainties are evaluated from RelativeJEREC1 (blue), RelativeJEREC2 (red), RelativePtBB (green) and RelativeJERHF (pink) sources whereas on right, these are evaluated from RelativePtEC1 (blue), RelativePtEC2 (red), RelativePFSR (green) and RelativePtHF (pink) sources.

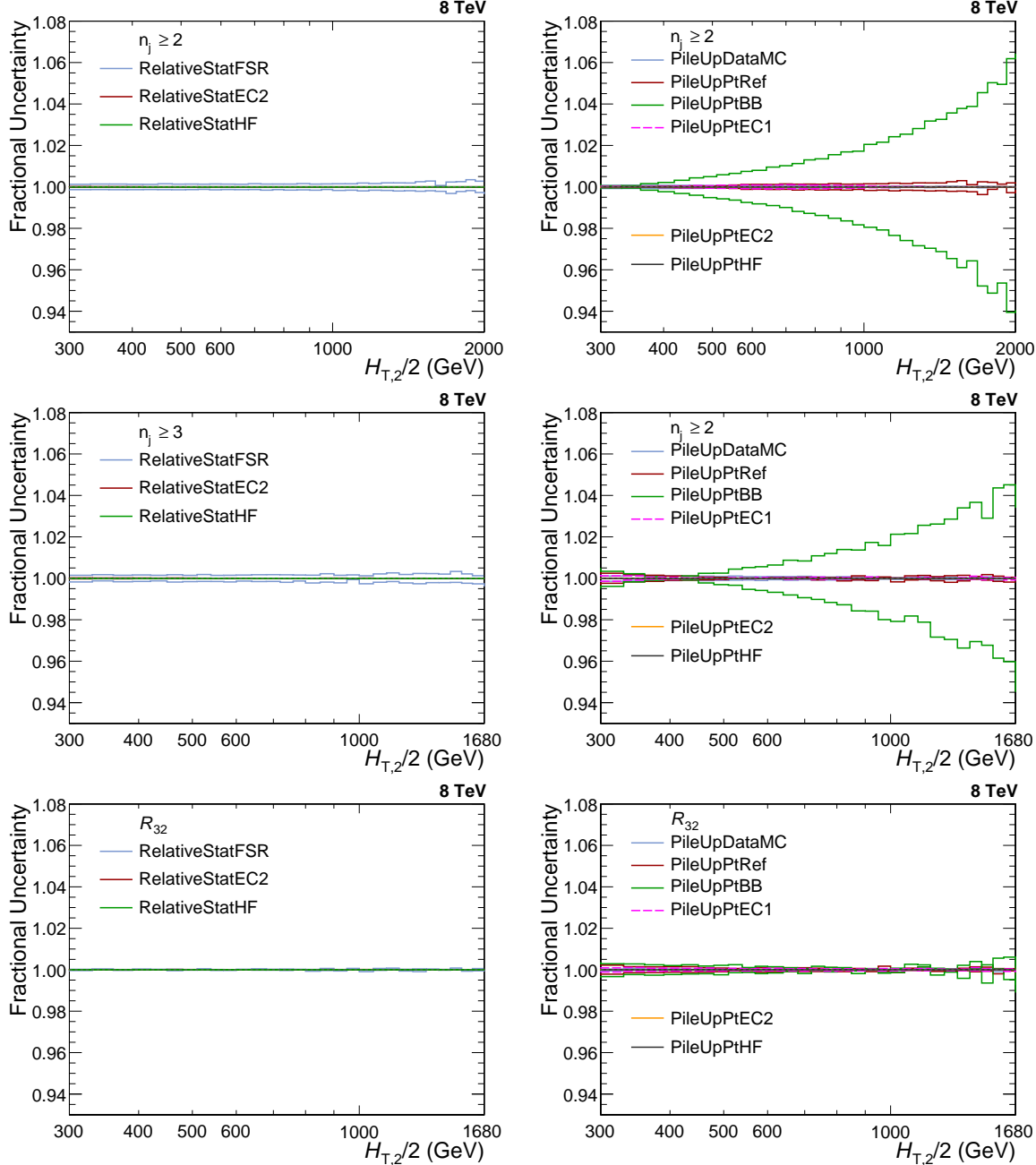


Figure A.3: The fractional jet energy correction (JEC) uncertainties from individual sources are shown for inclusive 2-jet (top) and 3-jet events cross-sections (middle); and cross-section ratio  $R_{32}$  (bottom). On left, JEC uncertainties are evaluated from RelativeStatFSR (blue), RelativeStatEC2 (red) and RelativeStatHF (green) sources whereas on right, these are evaluated from PileUpDataMC (blue), PileUpPtRef (red), PileUpPtBB (green), PileUpPtEC1 (pink), PileUpPtEC2 (orange) and PileUpPtHF (black) sources.

## A.3 Experimental Uncertainties

Table A.2: Experimental uncertainties (in %), from all sources as well as the total uncertainty, affecting the cross-section measurement in each bin of  $H_{\mathrm{T},2}/2$  for inclusive 2-jet events.

<b>Bin</b>	<b>Statistical</b>	<b>JEC</b>	<b>Unfolding</b>	<b>Lumi</b>	<b>Residual</b>	<b>Total</b>
300 - 330	0.242	+2.612 -2.565	+0.948 -0.928	2.6	1.0	+3.942 -3.906
330 - 360	0.258	+2.507 -2.473	+0.976 -0.969	2.6	1.0	+3.882 -3.858
360 - 390	0.202	+2.504 -2.465	+0.779 -0.783	2.6	1.0	+3.831 -3.807
390 - 420	0.193	+2.363 -2.381	+0.905 -0.904	2.6	1.0	+3.768 -3.780
420 - 450	0.084	+2.448 -2.422	+0.904 -0.895	2.6	1.0	+3.818 -3.799
450 - 480	0.096	+2.440 -2.352	+0.797 -0.795	2.6	1.0	+3.789 -3.733
480 - 510	0.107	+2.427 -2.406	+0.728 -0.715	2.6	1.0	+3.767 -3.751
510 - 540	0.128	+2.425 -2.395	+0.835 -0.862	2.6	1.0	+3.789 -3.775
540 - 570	0.154	+2.425 -2.376	+0.687 -0.674	2.6	1.0	+3.760 -3.726
570 - 600	0.180	+2.497 -2.474	+0.839 -0.827	2.6	1.0	+3.838 -3.820
600 - 640	0.209	+2.495 -2.491	+0.744 -0.743	2.6	1.0	+3.819 -3.816
640 - 680	0.264	+2.582 -2.545	+0.912 -0.912	2.6	1.0	+3.915 -3.891
680 - 720	0.320	+2.691 -2.574	+0.763 -0.756	2.6	1.0	+3.961 -3.880
720 - 760	0.387	+2.690 -2.755	+0.705 -0.712	2.6	1.0	+3.955 -4.001
760 - 800	0.465	+2.858 -2.846	+0.859 -0.846	2.6	1.0	+4.109 -4.098
800 - 850	0.548	+2.889 -2.913	+0.783 -0.787	2.6	1.0	+4.126 -4.143
850 - 900	0.698	+3.145 -3.102	+0.961 -0.958	2.6	1.0	+4.366 -4.334
900 - 950	0.847	+3.298 -3.233	+0.828 -0.829	2.6	1.0	+4.476 -4.429
950 - 1000	1.041	+3.291 -3.330	+0.895 -0.872	2.6	1.0	+4.525 -4.549
1000 - 1060	1.268	+3.598 -3.569	+0.945 -0.956	2.6	1.0	+4.817 -4.798
1060 - 1120	1.611	+3.759 -3.756	+0.970 -0.967	2.6	1.0	+5.043 -5.040
1120 - 1180	1.985	+4.154 -4.053	+1.089 -1.080	2.6	1.0	+5.490 -5.413
1180 - 1250	2.406	+4.251 -4.313	+1.062 -1.070	2.6	1.0	+5.722 -5.770
1250 - 1320	3.101	+4.696 -4.624	+1.151 -1.144	2.6	1.0	+6.384 -6.330
1320 - 1390	4.157	+4.934 -4.979	+1.343 -1.341	2.6	1.0	+7.155 -7.186
1390 - 1460	5.270	+5.148 -5.104	+1.185 -1.177	2.6	1.0	+7.965 -7.936
1460 - 1530	6.360	+5.890 -5.652	+1.405 -1.406	2.6	1.0	+9.213 -9.063
1530 - 1600	8.183	+5.924 -6.311	+1.598 -1.590	2.6	1.0	+10.601 -10.821
1600 - 1680	10.630	+5.969 -5.655	+1.607 -1.592	2.6	1.0	+12.608 -12.461
1680 - 1760	13.864	+7.245 -7.603	+1.821 -1.839	2.6	1.0	+15.993 -16.161
1760 - 1840	18.192	+7.781 -7.820	+1.902 -1.906	2.6	1.0	+20.071 -20.087
1840 - 1920	22.612	+7.647 -7.537	+1.588 -1.590	2.6	1.0	+24.085 -24.050
1920 - 2000	29.530	+9.199 -9.469	+1.511 -1.505	2.6	1.0	+31.092 -31.172

Table A.3: Experimental uncertainties (in %), from all sources as well as the total uncertainty, affecting the cross-section measurement in each bin of  $H_{\mathrm{T},2}/2$  for inclusive 3-jet events.

Bin	Statistical	JEC	Unfolding	Lumi	Residual	Total
300 - 330	0.796	+3.503 -3.475	+0.564 -0.552	2.6	1.0	+4.581 -4.558
330 - 360	0.781	+3.303 -3.186	+0.640 -0.633	2.6	1.0	+4.437 -4.350
360 - 390	0.583	+3.221 -3.094	+0.490 -0.496	2.6	1.0	+4.326 -4.233
390 - 420	0.531	+3.092 -3.149	+0.584 -0.584	2.6	1.0	+4.236 -4.278
420 - 450	0.224	+3.125 -2.996	+0.604 -0.592	2.6	1.0	+4.236 -4.140
450 - 480	0.248	+2.984 -2.890	+0.531 -0.528	2.6	1.0	+4.124 -4.056
480 - 510	0.269	+2.937 -2.963	+0.511 -0.512	2.6	1.0	+4.089 -4.108
510 - 540	0.318	+3.021 -2.797	+0.592 -0.612	2.6	1.0	+4.164 -4.007
540 - 570	0.375	+2.999 -2.935	+0.506 -0.500	2.6	1.0	+4.141 -4.094
570 - 600	0.434	+2.824 -2.906	+0.646 -0.620	2.6	1.0	+4.042 -4.096
600 - 640	0.497	+2.952 -2.956	+0.598 -0.604	2.6	1.0	+4.133 -4.136
640 - 680	0.617	+3.111 -3.001	+0.777 -0.786	2.6	1.0	+4.292 -4.215
680 - 720	0.739	+3.067 -2.984	+0.642 -0.611	2.6	1.0	+4.257 -4.194
720 - 760	0.895	+3.185 -3.111	+0.595 -0.607	2.6	1.0	+4.366 -4.313
760 - 800	1.068	+3.231 -3.166	+0.763 -0.774	2.6	1.0	+4.464 -4.419
800 - 850	1.250	+3.427 -3.295	+0.674 -0.687	2.6	1.0	+4.639 -4.544
850 - 900	1.578	+3.364 -3.540	+0.903 -0.898	2.6	1.0	+4.731 -4.857
900 - 950	1.961	+3.594 -3.524	+0.792 -0.793	2.6	1.0	+5.015 -4.965
950 - 1000	2.420	+3.603 -3.783	+0.846 -0.843	2.6	1.0	+5.226 -5.351
1000 - 1060	2.844	+4.164 -4.116	+0.916 -0.940	2.6	1.0	+5.834 -5.803
1060 - 1120	3.647	+4.038 -3.815	+0.963 -0.957	2.6	1.0	+6.188 -6.044
1120 - 1180	4.607	+4.278 -4.183	+1.084 -1.087	2.6	1.0	+6.961 -6.904
1180 - 1250	5.532	+4.894 -4.771	+1.074 -1.069	2.6	1.0	+7.967 -7.891
1250 - 1320	7.141	+5.144 -5.273	+1.222 -1.217	2.6	1.0	+9.312 -9.383
1320 - 1390	10.207	+5.542 -5.642	+1.414 -1.428	2.6	1.0	+12.027 -12.076
1390 - 1460	13.831	+5.630 -5.265	+1.257 -1.256	2.6	1.0	+15.242 -15.111
1460 - 1530	15.578	+5.576 -5.491	+1.546 -1.551	2.6	1.0	+16.850 -16.822
1530 - 1600	18.729	+6.409 -7.019	+1.718 -1.716	2.6	1.0	+20.063 -20.266
1600 - 1680	26.465	+7.017 -6.255	+1.775 -1.765	2.6	1.0	+27.578 -27.393

Table A.4: Experimental uncertainties (in %), from all sources as well as the total uncertainty, affecting the measurement of cross-section ratio  $R_{32}$ , in each bin of  $H_{T,2}/2$ .

<b>Bin</b>	<b>Statistical</b>	<b>JEC</b>	<b>Unfolding</b>	<b>Total</b>
300 - 330	0.741	+1.059 -1.097	+0.754 -0.751	+1.496 -1.522
330 - 360	0.587	+0.954 -0.923	+0.685 -0.689	+1.313 -1.292
360 - 390	0.519	+0.902 -0.855	+0.594 -0.593	+1.199 -1.163
390 - 420	0.236	+0.907 -0.952	+0.439 -0.438	+1.035 -1.074
420 - 450	0.192	+0.900 -0.835	+0.360 -0.361	+0.988 -0.930
450 - 480	0.209	+0.788 -0.802	+0.307 -0.308	+0.872 -0.884
480 - 510	0.245	+0.795 -0.867	+0.254 -0.235	+0.870 -0.931
510 - 540	0.287	+0.852 -0.682	+0.264 -0.268	+0.937 -0.787
540 - 570	0.326	+0.807 -0.803	+0.193 -0.189	+0.891 -0.887
570 - 600	0.397	+0.656 -0.774	+0.199 -0.219	+0.792 -0.898
600 - 640	0.447	+0.763 -0.797	+0.150 -0.154	+0.897 -0.926
640 - 680	0.573	+0.861 -0.781	+0.153 -0.140	+1.045 -0.979
680 - 720	0.663	+0.766 -0.787	+0.147 -0.164	+1.024 -1.042
720 - 760	0.774	+0.842 -0.769	+0.118 -0.118	+1.149 -1.097
760 - 800	0.970	+0.800 -0.729	+0.115 -0.096	+1.263 -1.218
800 - 850	1.116	+0.873 -0.775	+0.115 -0.104	+1.422 -1.363
850 - 900	1.436	+0.770 -0.896	+0.069 -0.069	+1.631 -1.694
900 - 950	1.716	+0.704 -0.752	+0.050 -0.051	+1.855 -1.874
950 - 1000	2.156	+0.824 -0.897	+0.089 -0.045	+2.310 -2.336
1000 - 1060	2.554	+0.812 -0.870	+0.045 -0.040	+2.680 -2.698
1060 - 1120	3.244	+0.792 -0.658	+0.018 -0.027	+3.339 -3.310
1120 - 1180	4.121	+0.985 -0.757	+0.025 -0.043	+4.237 -4.191
1180 - 1250	4.990	+1.031 -0.848	+0.023 -0.041	+5.095 -5.062
1250 - 1320	6.456	+0.750 -1.087	+0.079 -0.079	+6.500 -6.548
1320 - 1390	8.990	+1.112 -1.144	+0.080 -0.099	+9.059 -9.063
1390 - 1460	12.699	+1.157 -0.815	+0.076 -0.078	+12.751 -12.725
1460 - 1530	13.926	+0.768 -1.235	+0.143 -0.145	+13.948 -13.981
1530 - 1600	16.903	+1.050 -1.258	+0.120 -0.127	+16.936 -16.950
1600 - 1680	28.070	+1.471 -0.859	+0.178 -0.177	+28.109 -28.084

## A.4 Theoretical Uncertainties

Table A.5: Theoretical uncertainties (in %) calculating using CT10-NLO PDF set from all sources as well as the total uncertainty, affecting the cross-section measurement in each bin of  $H_{T,2}/2$  for inclusive 2-jet events.

Bin	Scale	PDF	NP	Total
300 - 330	+0.942 -6.149	+3.566 -3.090	0.825	+3.780 -6.931
330 - 360	+1.035 -6.289	+3.906 -3.342	0.736	+4.107 -7.159
360 - 390	+1.159 -6.438	+4.232 -3.573	0.696	+4.442 -7.396
390 - 420	+1.220 -6.536	+4.551 -3.794	0.723	+4.767 -7.592
420 - 450	+1.326 -6.660	+4.857 -3.997	0.745	+5.089 -7.802
450 - 480	+1.421 -6.776	+5.153 -4.186	0.765	+5.399 -8.001
480 - 510	+1.512 -6.888	+5.444 -4.365	0.782	+5.704 -8.192
510 - 540	+1.566 -6.967	+5.721 -4.527	0.797	+5.984 -8.347
540 - 570	+1.666 -7.082	+6.000 -4.682	0.810	+6.279 -8.528
570 - 600	+1.731 -7.172	+6.269 -4.825	0.822	+6.555 -8.683
600 - 640	+1.805 -7.271	+6.597 -4.979	0.833	+6.890 -8.852
640 - 680	+1.930 -7.416	+6.978 -5.143	0.845	+7.289 -9.064
680 - 720	+2.007 -7.527	+7.364 -5.295	0.856	+7.680 -9.243
720 - 760	+2.113 -7.663	+7.749 -5.437	0.865	+8.078 -9.436
760 - 800	+2.196 -7.781	+8.140 -5.569	0.873	+8.476 -9.609
800 - 850	+2.323 -7.945	+8.573 -5.706	0.881	+8.926 -9.822
850 - 900	+2.389 -8.062	+9.082 -5.863	0.889	+9.433 -10.008
900 - 950	+2.499 -8.227	+9.600 -6.018	0.896	+9.961 -10.232
950 - 1000	+2.631 -8.402	+10.134 -6.166	0.902	+10.509 -10.460
1000 - 1060	+2.738 -8.569	+10.747 -6.343	0.908	+11.127 -10.700
1060 - 1120	+2.853 -8.751	+11.431 -6.526	0.914	+11.817 -10.955
1120 - 1180	+2.992 -8.970	+12.183 -6.727	0.919	+12.579 -11.250
1180 - 1250	+3.135 -9.194	+13.019 -6.944	0.924	+13.423 -11.558
1250 - 1320	+3.324 -9.469	+14.004 -7.189	0.929	+14.423 -11.925
1320 - 1390	+3.434 -9.677	+15.080 -7.444	0.933	+15.494 -12.244
1390 - 1460	+3.629 -9.976	+16.223 -7.700	0.937	+16.650 -12.637
1460 - 1530	+3.760 -10.224	+17.505 -7.980	0.940	+17.929 -13.004
1530 - 1600	+3.894 -10.471	+18.891 -8.258	0.943	+19.311 -13.368
1600 - 1680	+4.107 -10.813	+20.496 -8.560	0.946	+20.925 -13.824
1680 - 1760	+4.421 -11.101	+22.481 -8.905	0.949	+22.931 -14.263
1760 - 1840	+4.921 -11.461	+24.654 -9.251	0.951	+25.158 -14.760
1840 - 1920	+5.404 -11.813	+27.143 -9.607	0.953	+27.692 -15.256
1920 - 2000	+5.867 -12.154	+29.986 -9.973	0.955	+30.570 -15.751

Table A.6: Theoretical uncertainties (in %) calculating using CT10-NLO PDF set from all sources as well as the total uncertainty, affecting the cross-section measurement in each bin of  $H_{T,2}/2$  for inclusive 3-jet events.

<b>Bin</b>	<b>Scale</b>	<b>PDF</b>	<b>NP</b>	<b>Total</b>
300 - 330	+0.539 -8.294	+5.716 -4.657	1.692	+5.986 -9.662
330 - 360	+0.550 -8.577	+5.977 -4.779	1.516	+6.191 -9.935
360 - 390	+0.599 -8.709	+6.187 -4.987	1.363	+6.363 -10.128
390 - 420	+0.719 -8.948	+6.751 -5.223	1.228	+6.900 -10.433
420 - 450	+0.799 -9.145	+7.031 -5.395	1.110	+7.162 -10.676
450 - 480	+0.847 -9.247	+7.404 -5.578	1.005	+7.520 -10.845
480 - 510	+0.847 -9.294	+7.837 -5.717	0.937	+7.938 -10.951
510 - 540	+0.922 -9.436	+8.198 -5.884	0.921	+8.301 -11.158
540 - 570	+0.974 -9.566	+8.529 -6.000	0.904	+8.632 -11.328
570 - 600	+1.086 -9.786	+8.970 -6.156	0.886	+9.079 -11.595
600 - 640	+1.107 -9.852	+9.402 -6.297	0.866	+9.506 -11.724
640 - 680	+1.278 -10.101	+10.310 -6.526	0.842	+10.423 -12.055
680 - 720	+1.384 -10.342	+9.682 -6.618	0.820	+9.815 -12.305
720 - 760	+1.415 -10.404	+11.051 -6.826	0.798	+11.170 -12.469
760 - 800	+1.547 -10.615	+11.565 -7.009	0.777	+11.694 -12.744
800 - 850	+1.679 -10.804	+12.242 -7.185	0.755	+12.379 -12.997
850 - 900	+2.085 -11.134	+13.097 -7.461	0.731	+13.282 -13.422
900 - 950	+2.475 -11.432	+13.889 -7.703	0.709	+14.125 -13.804
950 - 1000	+2.655 -11.608	+14.614 -7.915	0.688	+14.869 -14.066
1000 - 1060	+3.025 -11.926	+15.576 -8.173	0.667	+15.881 -14.473
1060 - 1120	+3.299 -12.189	+14.250 -8.441	0.645	+14.641 -14.840
1120 - 1180	+3.741 -12.584	+17.984 -8.787	0.625	+18.380 -15.361
1180 - 1250	+3.969 -12.843	+19.324 -9.127	0.625	+19.737 -15.768
1250 - 1320	+4.663 -13.452	+21.246 -9.517	0.642	+21.761 -16.490
1320 - 1390	+4.878 -13.702	+22.884 -9.899	0.657	+23.407 -16.916
1390 - 1460	+5.242 -14.095	+24.854 -10.332	0.670	+25.410 -17.489
1460 - 1530	+5.582 -14.464	+27.170 -10.733	0.682	+27.746 -18.024
1530 - 1600	+6.003 -14.907	+29.741 -11.165	0.692	+30.349 -18.637
1600 - 1680	+6.503 -15.418	+32.855 -11.617	0.702	+33.500 -19.317

Table A.7: Theoretical uncertainties (in %) calculating using CT10-NLO PDF set from all sources as well as the total uncertainty, affecting the measurement of cross-section ratio  $R_{32}$ , in each bin of  $H_{T,2}/2$ .

<b>Bin</b>	<b>Scale</b>	<b>PDF</b>	<b>NP</b>	<b>Total</b>
300 - 330	+0.038 -7.203	+2.458 -3.463	0.822	+2.592 -8.035
330 - 360	+0.027 -6.626	+2.317 -3.378	0.734	+2.431 -7.474
360 - 390	+0.024 -6.449	+2.149 -3.367	0.656	+2.247 -7.304
390 - 420	+0.084 -5.894	+2.411 -3.383	0.586	+2.482 -6.821
420 - 450	+0.113 -5.532	+2.345 -3.362	0.523	+2.405 -6.494
450 - 480	+0.109 -5.409	+2.390 -3.357	0.467	+2.438 -6.383
480 - 510	+0.073 -5.442	+2.506 -3.327	0.416	+2.541 -6.392
510 - 540	+0.107 -5.168	+2.559 -3.326	0.371	+2.588 -6.157
540 - 570	+0.112 -5.010	+2.586 -3.292	0.330	+2.609 -6.004
570 - 600	+0.163 -4.576	+2.729 -3.292	0.292	+2.750 -5.645
600 - 640	+0.146 -4.565	+2.824 -3.270	0.253	+2.839 -5.621
640 - 680	+0.198 -4.163	+3.368 -3.298	0.236	+3.382 -5.316
680 - 720	+0.155 -3.754	+2.352 -3.247	0.227	+2.368 -4.968
720 - 760	+0.196 -3.842	+3.267 -3.268	0.219	+3.280 -5.049
760 - 800	+0.126 -3.523	+3.366 -3.272	0.212	+3.375 -4.813
800 - 850	+0.110 -3.368	+3.596 -3.261	0.206	+3.604 -4.693
850 - 900	+0.048 -3.351	+3.909 -3.309	0.200	+3.915 -4.714
900 - 950	+0.116 -3.504	+4.148 -3.334	0.196	+4.154 -4.841
950 - 1000	+0.127 -3.511	+4.300 -3.335	0.192	+4.306 -4.846
1000 - 1060	+0.282 -3.683	+4.604 -3.357	0.204	+4.617 -4.988
1060 - 1120	+0.436 -3.779	+3.079 -3.375	0.224	+3.118 -5.071
1120 - 1180	+0.732 -3.982	+5.430 -3.452	0.241	+5.485 -5.276
1180 - 1250	+0.813 -4.031	+5.835 -3.511	0.258	+5.897 -5.352
1250 - 1320	+1.303 -4.414	+6.626 -3.591	0.275	+6.759 -5.697
1320 - 1390	+1.403 -4.471	+7.036 -3.659	0.290	+7.180 -5.785
1390 - 1460	+1.564 -4.590	+7.657 -3.778	0.304	+7.822 -5.953
1460 - 1530	+1.765 -4.738	+8.438 -3.853	0.316	+8.626 -6.115
1530 - 1600	+2.040 -4.972	+9.306 -3.962	0.328	+9.532 -6.366
1600 - 1680	+2.313 -5.179	+10.381 -4.075	0.339	+10.641 -6.599

# Bibliography

- [1] S. Chatrchyan *et al.*, “Measurement of the ratio of the inclusive 3-jet cross section to the inclusive 2-jet cross section in pp collisions at  $\sqrt{s} = 7$  TeV and first determination of the strong coupling constant in the TeV range,” *Eur. Phys. J.*, vol. C73, no. 10, p. 2604, 2013.
- [2] D. J. Griffiths, *Introduction to elementary particles; 2nd rev. version*. Physics textbook, New York, NY: Wiley, 2008.
- [3] D. H. Perkins, *Introduction to high energy physics*. 1982.
- [4] M. Herrero, “The Standard model,” *NATO Sci. Ser. C*, vol. 534, pp. 1–59, 1999.
- [5] S. Weinberg, “A Model of Leptons,” *Phys. Rev. Lett.*, vol. 19, pp. 1264–1266, 1967.
- [6] M. E. Peskin and D. V. Schroeder, *An Introduction to quantum field theory*. Reading, USA: Addison-Wesley, 1995.
- [7] S. L. Glashow, “Towards a Unified Theory: Threads in a Tapestry,” *Rev. Mod. Phys.*, vol. 52, pp. 539–543, 1980.
- [8] A. Salam, “Gauge Unification of Fundamental Forces,” *Rev. Mod. Phys.*, vol. 52, pp. 525–538, 1980. [Science210,723(1980)].

- [9] H. Georgi and S. L. Glashow, “Unity of All Elementary Particle Forces,” *Phys. Rev. Lett.*, vol. 32, pp. 438–441, 1974.
- [10] S. Chatrchyan *et al.*, “Observation of a new boson at a mass of 125 GeV with the CMS experiment at the LHC,” *Phys. Lett.*, vol. B716, pp. 30–61, 2012.
- [11] G. Aad *et al.*, “Observation of a new particle in the search for the Standard Model Higgs boson with the ATLAS detector at the LHC,” *Phys. Lett.*, vol. B716, pp. 1–29, 2012.
- [12] R. K. Ellis, W. J. Stirling, and B. R. Webber, “QCD and collider physics,” *Camb. Monogr. Part. Phys. Nucl. Phys. Cosmol.*, vol. 8, pp. 1–435, 1996.
- [13] F. Halzen and A. D. Martin, *QUARKS AND LEPTONS: AN INTRODUCTORY COURSE IN MODERN PARTICLE PHYSICS*. 1984.
- [14] M. Gell-Mann, “Symmetries of baryons and mesons,” *Phys. Rev.*, vol. 125, pp. 1067–1084, 1962.
- [15] K. Rabbertz, “Jet Physics at the LHC,” *Springer Tracts Mod. Phys.*, vol. 268, pp. pp.1–214, 2017.
- [16] G. ’t Hooft, “Dimensional regularization and the renormalization group,” *Nucl. Phys.*, vol. B61, pp. 455–468, 1973.
- [17] S. Weinberg, “New approach to the renormalization group,” *Phys. Rev.*, vol. D8, pp. 3497–3509, 1973.
- [18] C. Patrignani *et al.*, “Review of Particle Physics,” *Chin. Phys.*, vol. C40, no. 10, p. 100001, 2016.
- [19] L. Evans and P. Bryant, “LHC Machine,” *JINST*, vol. 3, p. S08001, 2008.

- [20] S. Myers and E. Picasso, “The design, construction and commissioning of the cern large electron–positron collider,” *Contemporary Physics*, vol. 31, no. 6, pp. 387–403, 1990.
- [21] K. Aamodt *et al.*, “The ALICE experiment at the CERN LHC,” *JINST*, vol. 3, p. S08002, 2008.
- [22] G. Aad *et al.*, “The ATLAS Experiment at the CERN Large Hadron Collider,” *JINST*, vol. 3, p. S08003, 2008.
- [23] S. Chatrchyan *et al.*, “The CMS Experiment at the CERN LHC,” *JINST*, vol. 3, p. S08004, 2008.
- [24] G. L. Bayatian *et al.*, “CMS Physics,” 2006.
- [25] G. L. Bayatian *et al.*, “CMS technical design report, volume II: Physics performance,” *J. Phys.*, vol. G34, no. 6, pp. 995–1579, 2007.
- [26] A. A. Alves, Jr. *et al.*, “The LHCb Detector at the LHC,” *JINST*, vol. 3, p. S08005, 2008.
- [27] O. Adriani *et al.*, “The LHCf detector at the CERN Large Hadron Collider,” *JINST*, vol. 3, p. S08006, 2008.
- [28] G. Anelli *et al.*, “The TOTEM experiment at the CERN Large Hadron Col-  
lider,” *JINST*, vol. 3, p. S08007, 2008.
- [29] C. Collaboration, “CMS Luminosity Based on Pixel Cluster Counting - Sum-  
mer 2013 Update,” 2013.
- [30] S. van der Meer, “Calibration of the Effective Beam Height in the ISR,” 1968.
- [31] P. Adzic *et al.*, “Energy resolution of the barrel of the CMS electromagnetic  
calorimeter,” *JINST*, vol. 2, p. P04004, 2007.

- [32] S. Chatrchyan *et al.*, “Performance of the CMS Hadron Calorimeter with Cosmic Ray Muons and LHC Beam Data,” *JINST*, vol. 5, p. T03012, 2010.
- [33] I. Bird, K. Bos, N. Brook, D. Duellmann, C. Eck, I. Fisk, D. Foster, B. Gibbard, C. Grandi, F. Grey, *et al.*, “LHC computing Grid. Technical design report,” 2005.
- [34] N. Metropolis and S. Ulam, “The monte carlo method,” *Journal of the American Statistical Association*, vol. 44, no. 247, pp. 335–341, 1949. PMID: 18139350.
- [35] B. Andersson, G. Gustafson, G. Ingelman, and T. Sjöstrand, “Parton fragmentation and string dynamics,” *Physics Reports*, vol. 97, no. 2, pp. 31 – 145, 1983.
- [36] T. Sjostrand, S. Mrenna, and P. Z. Skands, “PYTHIA 6.4 Physics and Manual,” *JHEP*, vol. 05, p. 026, 2006.
- [37] T. Sjostrand, S. Mrenna, and P. Z. Skands, “A Brief Introduction to PYTHIA 8.1,” *Comput. Phys. Commun.*, vol. 178, pp. 852–867, 2008.
- [38] R. Field, “Min-Bias and the Underlying Event at the LHC,” *Acta Phys. Polon.*, vol. B42, pp. 2631–2656, 2011.
- [39] V. Khachatryan *et al.*, “Event generator tunes obtained from underlying event and multiparton scattering measurements,” *Eur. Phys. J.*, vol. C76, no. 3, p. 155, 2016.
- [40] J. Alwall, M. Herquet, F. Maltoni, O. Mattelaer, and T. Stelzer, “MadGraph 5 : Going Beyond,” *JHEP*, vol. 06, p. 128, 2011.
- [41] J. Alwall *et al.*, “A Standard format for Les Houches event files,” *Comput. Phys. Commun.*, vol. 176, pp. 300–304, 2007.

- [42] G. Corcella, I. G. Knowles, G. Marchesini, S. Moretti, K. Odagiri, P. Richardson, M. H. Seymour, and B. R. Webber, “HERWIG 6: An Event generator for hadron emission reactions with interfering gluons (including supersymmetric processes),” *JHEP*, vol. 01, p. 010, 2001.
- [43] M. Bahr *et al.*, “Herwig++ Physics and Manual,” *Eur. Phys. J.*, vol. C58, pp. 639–707, 2008.
- [44] M. Bahr, S. Gieseke, M. Gigg, D. Grellscheid, K. Hamilton, S. Platzer, P. Richardson, M. H. Seymour, and J. Tully, “Herwig++ 2.3 Release Note,” 2008.
- [45] S. Frixione, P. Nason, and C. Oleari, “Matching NLO QCD computations with Parton Shower simulations: the POWHEG method,” *JHEP*, vol. 11, p. 070, 2007.
- [46] P. Nason, “A New method for combining NLO QCD with shower Monte Carlo algorithms,” *JHEP*, vol. 11, p. 040, 2004.
- [47] S. Alioli, K. Hamilton, P. Nason, C. Oleari, and E. Re, “Jet pair production in POWHEG,” *JHEP*, vol. 04, p. 081, 2011.
- [48] C. Oleari, “The POWHEG-BOX,” *Nucl. Phys. Proc. Suppl.*, vol. 205-206, pp. 36–41, 2010.
- [49] Z. Nagy, “Three jet cross-sections in hadron hadron collisions at next-to-leading order,” *Phys. Rev. Lett.*, vol. 88, p. 122003, 2002.
- [50] Z. Nagy, “Next-to-leading order calculation of three jet observables in hadron hadron collision,” *Phys. Rev.*, vol. D68, p. 094002, 2003.
- [51] T. Kluge, K. Rabbertz, and M. Wobisch, “FastNLO: Fast pQCD calculations for PDF fits,” in *Deep inelastic scattering. Proceedings, 14th International Workshop, DIS 2006, Tsukuba, Japan, April 20-24, 2006*, pp. 483–486, 2006.

- [52] D. Britzger, K. Rabbertz, F. Stober, and M. Wobisch, “New features in version 2 of the fastNLO project,” in *Proceedings, 20th International Workshop on Deep-Inelastic Scattering and Related Subjects (DIS 2012): Bonn, Germany, March 26-30, 2012*, pp. 217–221, 2012.
- [53] M. R. Whalley, D. Bourilkov, and R. C. Group, “The Les Houches accord PDFs (LHAPDF) and LHAGLUE,” in *HERA and the LHC: A Workshop on the implications of HERA for LHC physics. Proceedings, Part B*, pp. 575–581, 2005.
- [54] A. Buckley, J. Ferrando, S. Lloyd, K. Nordström, B. Page, M. Rüfenacht, M. Schönher, and G. Watt, “LHAPDF6: parton density access in the LHC precision era,” *Eur. Phys. J.*, vol. C75, p. 132, 2015.
- [55] S. Agostinelli *et al.*, “GEANT4: A Simulation toolkit,” *Nucl. Instrum. Meth.*, vol. A506, pp. 250–303, 2003.
- [56] S. Abdullin, P. Azzi, F. Beaudette, P. Janot, and A. Perrotta, “The fast simulation of the CMS detector at LHC,” *J. Phys. Conf. Ser.*, vol. 331, p. 032049, 2011.
- [57] T. Schörner-Sadenius, ed., *The Large Hadron Collider*. Berlin: Springer, 2015.
- [58] “Particle-Flow Event Reconstruction in CMS and Performance for Jets, Taus, and MET,” 2009.
- [59] “Commissioning of the Particle-flow Event Reconstruction with the first LHC collisions recorded in the CMS detector,” 2010.
- [60] W. Adam, B. Mangano, T. Speer, and T. Todorov, “Track reconstruction in the CMS tracker,” 2005.
- [61] S. Chatrchyan *et al.*, “Determination of Jet Energy Calibration and Transverse Momentum Resolution in CMS,” *JINST*, vol. 6, p. P11002, 2011.

- [62] V. Khachatryan *et al.*, “Jet energy scale and resolution in the CMS experiment in pp collisions at 8 TeV,” *JINST*, vol. 12, no. 02, p. P02014, 2017.
- [63] “CMS: The computing project. Technical design report,” 2005.
- [64] R. Brun and F. Rademakers, “ROOT: An object oriented data analysis framework,” *Nucl. Instrum. Meth.*, vol. A389, pp. 81–86, 1997.
- [65] V. Khachatryan *et al.*, “Measurement and QCD analysis of double-differential inclusive jet cross sections in pp collisions at  $\sqrt{s} = 8$  TeV and cross section ratios to 2.76 and 7 TeV,” *JHEP*, vol. 03, p. 156, 2017.
- [66] A. M. Sirunyan *et al.*, “Measurement of the triple-differential dijet cross section in proton-proton collisions at  $\sqrt{s} = 8$  TeV and constraints on parton distribution functions,” *Eur. Phys. J.*, vol. C77, no. 11, p. 746, 2017.
- [67] C. J. Clopper and E. S. Pearson, “The use of confidence or fiducial limits illustrated in the case of the binomial,” *Biometrika*, vol. 26, no. 4, pp. 404–413, 1934.
- [68] C. Collaboration, “Jet Performance in pp Collisions at 7 TeV,” 2010.
- [69] C. Collaboration, “Jet Identification at 8 TeV.” <https://twiki.cern.ch/twiki/bin/viewauth/CMS/JetID>, 2012. (accessed on 2017-10-31).
- [70] C. Collaboration, “Jet Energy Resolution at 8 TeV.” <https://twiki.cern.ch/twiki/bin/viewauth/CMS/JetResolution>, 2012. (accessed on 2016-01-22).
- [71] C. Collaboration, “Jet Energy Resolution in CMS at  $\text{sqrt}(s)=7$  TeV,” 2011.
- [72] G. D’Agostini, “A Multidimensional unfolding method based on Bayes’ theorem,” *Nucl. Instrum. Meth.*, vol. A362, pp. 487–498, 1995.

- [73] G. D'Agostini, "Improved iterative Bayesian unfolding," 2010.
- [74] T. Adye, "Unfolding algorithms and tests using RooUnfold," in *Proceedings, PHYSTAT 2011 Workshop on Statistical Issues Related to Discovery Claims in Search Experiments and Unfolding, CERN, Geneva, Switzerland 17-20 January 2011*, (Geneva), pp. 313–318, CERN, CERN, 2011.
- [75] S. Chatrchyan *et al.*, "Measurement of the Inclusive Jet Cross Section in  $pp$  Collisions at  $\sqrt{s} = 7$  TeV," *Phys. Rev. Lett.*, vol. 107, p. 132001, 2011.
- [76] C. Collaboration, "Jet energy scale uncertainty sources." <https://twiki.cern.ch/twiki/bin/viewauth/CMS/JECUncertaintySources>, 2012. (accessed on 2017-10-31).
- [77] S. Chatrchyan *et al.*, "Measurements of differential jet cross sections in proton-proton collisions at  $\sqrt{s} = 7$  TeV with the CMS detector," *Phys. Rev.*, vol. D87, no. 11, p. 112002, 2013. [Erratum: Phys. Rev.D87,no.11,119902(2013)].
- [78] G. Aad *et al.*, "Measurement of the inclusive jet cross section in  $pp$  collisions at  $\sqrt{s}=2.76$  TeV and comparison to the inclusive jet cross section at  $\sqrt{s}=7$  TeV using the ATLAS detector," *Eur. Phys. J.*, vol. C73, no. 8, p. 2509, 2013.
- [79] G. Aad *et al.*, "Measurement of the inclusive jet cross-section in proton-proton collisions at  $\sqrt{s} = 7$  TeV using  $4.5 \text{ fb}^{-1}$  of data with the ATLAS detector," *JHEP*, vol. 02, p. 153, 2015. [Erratum: JHEP09,141(2015)].
- [80] V. Khachatryan *et al.*, "Measurement of the inclusive 3-jet production differential cross section in proton–proton collisions at 7 TeV and determination of the strong coupling constant in the TeV range," *Eur. Phys. J.*, vol. C75, no. 5, p. 186, 2015.
- [81] V. Khachatryan *et al.*, "Measurement of the inclusive jet cross section in  $pp$  collisions at  $\sqrt{s} = 2.76$  TeV," *Eur. Phys. J.*, vol. C76, no. 5, p. 265, 2016.

- [82] S. Alekhin, J. Blumlein, and S. Moch, “Parton Distribution Functions and Benchmark Cross Sections at NNLO,” *Phys. Rev.*, vol. D86, p. 054009, 2012.
- [83] H.-L. Lai, M. Guzzi, J. Huston, Z. Li, P. M. Nadolsky, J. Pumplin, and C. P. Yuan, “New parton distributions for collider physics,” *Phys. Rev.*, vol. D82, p. 074024, 2010.
- [84] A. D. Martin, W. J. Stirling, R. S. Thorne, and G. Watt, “Parton distributions for the LHC,” *Eur. Phys. J.*, vol. C63, pp. 189–285, 2009.
- [85] A. D. Martin, W. J. Stirling, R. S. Thorne, and G. Watt, “Uncertainties on alpha(S) in global PDF analyses and implications for predicted hadronic cross sections,” *Eur. Phys. J.*, vol. C64, pp. 653–680, 2009.
- [86] R. D. Ball *et al.*, “Parton distributions with LHC data,” *Nucl. Phys.*, vol. B867, pp. 244–289, 2013.
- [87] S. Dulat, T.-J. Hou, J. Gao, M. Guzzi, J. Huston, P. Nadolsky, J. Pumplin, C. Schmidt, D. Stump, and C. P. Yuan, “New parton distribution functions from a global analysis of quantum chromodynamics,” *Phys. Rev.*, vol. D93, no. 3, p. 033006, 2016.
- [88] H. Abramowicz *et al.*, “Combination of measurements of inclusive deep inelastic  $e^\pm p$  scattering cross sections and QCD analysis of HERA data,” *Eur. Phys. J.*, vol. C75, no. 12, p. 580, 2015.
- [89] L. A. Harland-Lang, A. D. Martin, P. Motylinski, and R. S. Thorne, “Parton distributions in the LHC era: MMHT 2014 PDFs,” *Eur. Phys. J.*, vol. C75, no. 5, p. 204, 2015.
- [90] R. D. Ball *et al.*, “Parton distributions for the LHC Run II,” *JHEP*, vol. 04, p. 040, 2015.

- [91] W. Hollik *et al.*, “Electroweak physics,” *Acta Phys. Polon.*, vol. B35, pp. 2533–2555, 2004.
- [92] S. Dittmaier, A. Huss, and C. Speckner, “Weak radiative corrections to dijet production at hadron colliders,” *JHEP*, vol. 11, p. 095, 2012.
- [93] J. Pumplin, D. R. Stump, J. Huston, H. L. Lai, P. M. Nadolsky, and W. K. Tung, “New generation of parton distributions with uncertainties from global QCD analysis,” *JHEP*, vol. 07, p. 012, 2002.
- [94] S. Chatrchyan *et al.*, “Determination of the top-quark pole mass and strong coupling constant from the t t-bar production cross section in pp collisions at  $\sqrt{s} = 7$  TeV,” *Phys. Lett.*, vol. B728, pp. 496–517, 2014. [Erratum: *Phys. Lett.*B738,526(2014)].
- [95] V. Khachatryan *et al.*, “Constraints on parton distribution functions and extraction of the strong coupling constant from the inclusive jet cross section in pp collisions at  $\sqrt{s} = 7$  TeV,” *Eur. Phys. J.*, vol. C75, no. 6, p. 288, 2015.
- [96] G. Aad *et al.*, “Measurement of transverse energy-energy correlations in multi-jet events in pp collisions at  $\sqrt{s} = 7$  TeV using the ATLAS detector and determination of the strong coupling constant  $\alpha_s(m_Z)$ ,” *Phys. Lett.*, vol. B750, pp. 427–447, 2015.
- [97] V. M. Abazov *et al.*, “Determination of the strong coupling constant from the inclusive jet cross section in  $p\bar{p}$  collisions at  $\text{sqrt}(s)=1.96$  TeV,” *Phys. Rev.*, vol. D80, p. 111107, 2009.
- [98] V. M. Abazov *et al.*, “Measurement of angular correlations of jets at  $\sqrt{s} = 1.96$  TeV and determination of the strong coupling at high momentum transfers,” *Phys. Lett.*, vol. B718, pp. 56–63, 2012.

- [99] V. Andreev *et al.*, “Measurement of multijet production in  $ep$  collisions at high  $Q^2$  and determination of the strong coupling  $\alpha_s$ ,” *Eur. Phys. J.*, vol. C75, no. 2, p. 65, 2015.
- [100] V. Andreev *et al.*, “Measurement of Jet Production Cross Sections in Deep-inelastic ep Scattering at HERA,” *Eur. Phys. J.*, vol. C77, no. 4, p. 215, 2017.
- [101] H. Abramowicz *et al.*, “Inclusive-jet photoproduction at HERA and determination of alphas,” *Nucl. Phys.*, vol. B864, pp. 1–37, 2012.
- [102] T. Affolder *et al.*, “Measurement of the strong coupling constant from inclusive jet production at the Tevatron  $\bar{p}p$  collider,” *Phys. Rev. Lett.*, vol. 88, p. 042001, 2002.
- [103] R. D. Ball, L. Del Debbio, S. Forte, A. Guffanti, J. I. Latorre, J. Rojo, and M. Ubiali, “A first unbiased global NLO determination of parton distributions and their uncertainties,” *Nucl. Phys.*, vol. B838, pp. 136–206, 2010.
- [104] K. G. Chetyrkin, J. H. Kuhn, and M. Steinhauser, “RunDec: A Mathematica package for running and decoupling of the strong coupling and quark masses,” *Comput. Phys. Commun.*, vol. 133, pp. 43–65, 2000.
- [105] B. Schmidt and M. Steinhauser, “CRunDec: a C++ package for running and decoupling of the strong coupling and quark masses,” *Comput. Phys. Commun.*, vol. 183, pp. 1845–1848, 2012.